Employing Low-Cost Organic and Inorganic Hole Transporting Materials for Perovskite Solar Cells

Eman Ahmed A. Alkhudhayr

A thesis submitted for the degree of Doctor of Philosophy

School of Mathematics, Statistics and Physics

June 2023

Abstract

Organic-inorganic halide perovskites have attracted substantial attention from the photovoltaic research community since 2009, with power conversion efficiencies (PCE) already exceeding 26.1% 2023. The low cost of perovskite precursors and their simple solution processability make them very promising to be developed as a next-generation photovoltaic technology. However, perovskites are notoriously unstable, particularly in high-humidity environments, which are currently slowing down their widespread implementation. While efficient encapsulation of the full device will certainly inhibit this type of degradation, it is still desirable to fabricate devices which are stable in standard atmospheric conditions. Here, the hole-transporting materials (HTM) play a key role as they can enhance the stability of Perovskite solar cells (PSCs) by acting as moisture barriers. This thesis will discuss the effect of novel hole-transporting materials on Perovskite device performance.

Chapter 1 shows the introduction and the aims of this thesis. Chapter 2 gives a general background, the working principle of perovskite solar cells, and introduces the hole transporting materials and their classification as organic and inorganic. Chapter 3 describes the techniques used in the characterization in detail. Chapter 4 represents a new HTM (TPABT) based on familiar building blocks linked by functional amides and their application in PSCs. For a non-conjugated material, this HTM demonstrates the exceptional properties of high conductivity and charge carrier mobility and a blue-shifted onset of absorption that avoids competition for light with the perovskite layer. These observations show that conjugation through the main chain is unimportant for materials with good charge transfer properties. Chapter 5 focused on investigating two new hole transport oxides, $CuBi_2O_4$ and $NiMnO_4$, using a novel synthesis method with different variables, such as various salts and hydrothermal treatment of different durations. The XRD patterns of these materials confirmed their crystal structure and alignment with existing databases. Moreover, a perovskite solar cell utilising a spin-coated smooth film of $CuBi_2O_4$ as the hole-transporting material achieved an efficiency of 2.13%. Last chapter is the sixth and presents the conclusions and outlook.

Acknowledgments

I am extremely grateful to my supervisors, Professor Elizabeth Gibson, Dr Pablo Docampo, and Dr Toby Hallam, for their invaluable supervision, mentorship, constant help, support, encouragement, and patience during my PhD study. Their support, especially during the period of the COVID pandemic, is above and beyond. I am thankful for the financial support from King Faisal University, Saudi Arabia.

I gratefully acknowledge Dr Fabio Cucinotta for assistance with Photoluminescence measurements. Special thanks to Dr Jamie Gould for carrying out XRD variable temperature experiments of p-type materials and his useful discussion, and Dr Isabel Arce-Garcia for the SEM images that are presented in the images in Chapter 5.

Many thanks to Dr Paul Waddell for the TPABT crystal structures and Dr Su Stephens for her help in the lab and the training using the reactor. I acknowledge the assistance and advice from members of staff and colleagues of the Energy Material Laboratory group and the Docampo group in Glasgow.

Special thanks to my family, Ibrahim Ahmed, and Abdullah Adamu, for supporting me to finish my PhD. Thank you for motivating me to overcome the difficulties during these years.
Thanks to my close friends for their endless support and understanding.

Table of Contents

List of Figures

List of Tables

Acronyms

J_{SC}	Short Circuit Current
n-i-p	Conventional perovskite solar cells
P_{in}	Light Intensity
p-i-n	Inverted perovskite solar cells
R_{rec}	Recombination Resistance
T_g	Glass-transition temperature
T_m	Melting temperature
V_{OC}	Open Circuit Voltage
AFM	Atomic Force Microscopy
CB	Conduction Band
CV	Cyclic Voltammetry
DSC	Differential Scanning Calorimetry
ETL	Electron Transporting Layer
FF	Fill Factor
FTO	Fluorine-doped Tin Oxide
HOMO	Highest Occupied Molecular Orbital
HTL	Hole Transporting Layer
J-V	Current-voltage
LUMO	Lowest Unoccupied Molecular Orbital
PCE	Power Conversion Efficiency
PL	Photoluminescence
PSCs	Perovskite solar cells
PV	Photovoltaic
SEM	Scanning Electron Microscopy
TGA	Thermogravimetric Analysis
VB	Valence Band
XRD	X-Ray Diffraction

Chapter 1. Introduction

1.1 Background and Motivation

Nowadays, the study of alternative and sustainable sources is considered among one of the most important priorities of engineering sciences. Sustainable sources like sun, wind, hydro, and tidal power could become an alternative to fossil fuels which have been extensively used in the past few decades[1]. Solar energy, which is crucial in meeting the predictable future demands, provides 1.9×10^8 TWh of radiation yearly on the surface of the earth, therefore adequately yields a year of energy requirements within a seven-to-eight-hour period. This provision from the sun is both free and unlimited as well as clean, sustainable, readily accessible and a ubiquitous energy source [2].

The total electricity energy consumption across the world in 2021 was found to be approximately 25,343 terawatt-hours (TWh)[3]. Due to the rising growth of population and changing world economy, these figures are incessantly rising. A reduction in the influence on the environment that is instigated by using damaging energy development techniques undertaken by various societies to achieve individual societal requirements is essential for unceasing development. However, the majority of energy resources existing have distinct environmental impacts, and so a proposal of using resources which provide adequate efficiency with a minimized environmental impact is desired. For example, methods with scarcer use of resources and minimum pollution production for the equal product yields a superior efficiency. Sustainable energy is the extraction and utilisation of bulk quantity sources which will not become depleted. Countless fresh efforts are being undertaken to reduce cost and escalate output[4-6].

Solar cells are defined as a device which directly transfers incident solar radiation to electricity using the photovoltaic effect, a physical and chemical phenomenon[7]. Many factors can limit the performance of PV operation such as material quality, light intensity, humidity, and temperature[8]. All these factors are directly related to the absorption efficiency of photons and the generation of free charge carriers. Solar cells were established in 1839 by Alexandre-Edmond Becquerel[9]. Silicon (Si), gallium arsenide (GaAs) and other inorganic crystalline semi-conductors have shown to be the optimum performing photovoltaic devices so far. Power conversion efficiencies (PCEs) reach approximately 27.8% (single crystal) for Si-constructed cells[10] as shown in Figure 1.1 with these solar cells currently having extensive applications commercially for both residential and industrial uses. Conversely, a large thickness required to provide sufficient light absorption due to

the indirect bandgap features of silicon, considerably increases the intricacy and expenditure of the fabrication process. This restricts its use within the energy industry. Furthermore, whilst producing a thin film solar cell with the potential for attaining a PCEs of 28.8%, the cost of using the direct bandgap material GaAs also makes it unavailable for extensive commercialization [11].

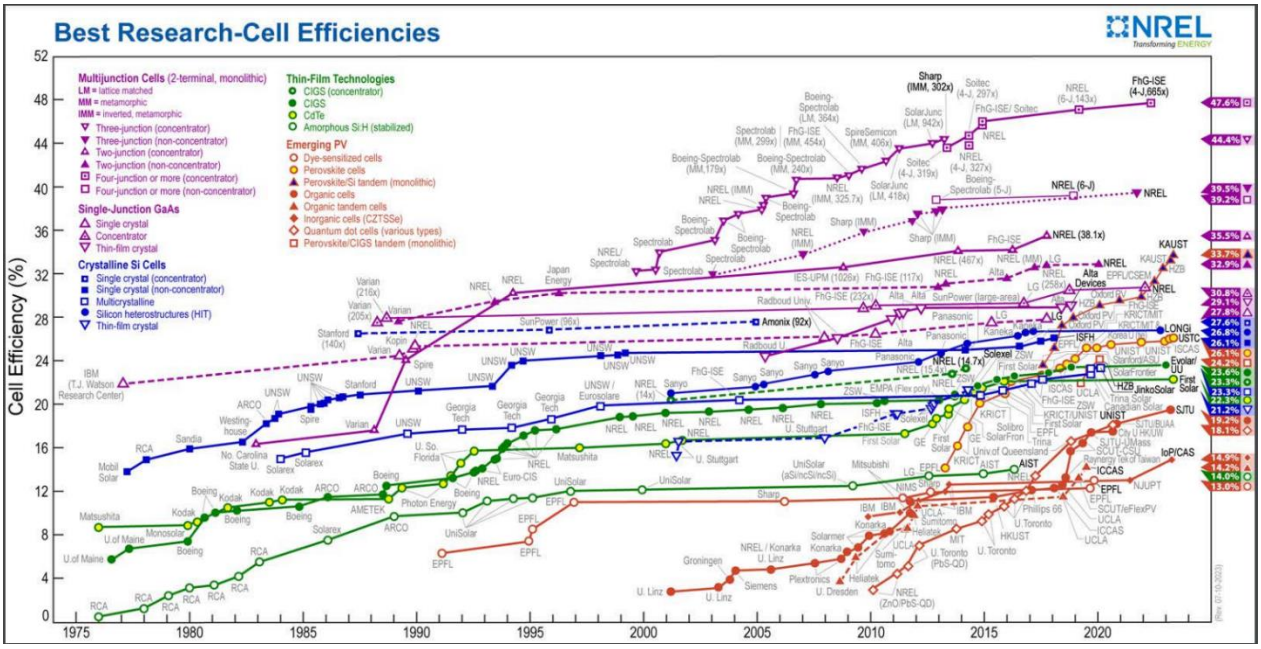

Figure 1.1. Best Research-Cell Efficiencies Chart from NREL Transforming Energy[10].

Various additional materials, such as cadmium telluride (CdTe) and copper indium gallium selenide (CIGS), have been studied as options in fabricating film solar cells, with each having PCEs of 22.1% and 22.4% respectively[12]. Nonetheless, the former option is afflicted by the adverse environmental effects stemming from cadmium's toxicity. Conversely, the extensive manufacturing of the latter option is constrained by the intricate production processes and the scarcity of indium, a rare element. Consequently, extended periods for financial and energy recuperation currently impede the broad adoption of photovoltaic devices of this nature[12].

Solution-processed semiconductors have emerged as promising materials suitable for a range of optoelectronic applications, including but not limited to light-emitting diodes (LEDs), field-effect transistors (FETs), and photovoltaic devices[13]. These devices enjoy advantages stemming from their ability to utilise materials that are readily tunable, cost-effective, and readily accessible. Consequently, they can employ cost-efficient and uncomplicated solution processing techniques

such as spin-coating, spray-coating, and reel-to-reel printing. Consequently, it is expected that solar cells employing these materials will exhibit reduced financial and energetic overheads in comparison to conventional crystalline inorganic semiconductors.

In 1991, O'Regan and Grätzel pioneered the development of a solar cell featuring nanostructured electrodes and efficient charge-injection dyes, which they named the dye-sensitised solar cell (DSSC)[14]. This class of solution-processed photovoltaic devices facilitates the separation of constituent materials, thereby providing the opportunity to independently investigate and customise the fundamental processes of solar energy conversion. Drawing inspiration from the DSSC structure, Miyasaka and colleagues introduced the perovskite-sensitized solar cell in 2009, achieving a modest power conversion efficiency (PCE) of 3.81% [15, 16]. Subsequently, perovskite solar cells (PSCs) have emerged as the most promising photovoltaic materials, garnering significant research attention and setting new efficiency records that have rapidly increased to 26% as of 2023[10].

Nevertheless, despite their remarkable efficiency achievements, PSCs still confront two major challenges that impede their widespread adoption within the energy industry. Firstly, the predominant hole-transporting material (HTM) utilised in PSCs, namely 2,2',7,7'-tetrakis(N,N-di-p-methoxyphenyl-amine)9,9'-Spirobifluorene (Spiro-OMeTAD), is prohibitively expensive for large-scale industrial applications. Secondly, organic-inorganic halide perovskite, being an ionic solid, exhibits high sensitivity to atmospheric moisture, leading to rapid degradation if the perovskite film lacks adequate protection. Consequently, the quest for alternative, cost-effective HTMs that offer exceptional stability represents a paramount research focus in the realm of perovskite photovoltaic research [17, 18].

1.2 Aims of the Thesis

The target of this thesis is to find alternative HTMs for low-cost, efficient, and stable PSCs. In a PSC with a regular structure, a HTL is located on top of the perovskite layer. The HTL has two functions: (i) selectively removing holes from the absorber layer and efficiently transporting free carriers to the electrode. Moreover, it acts as a blocking layer to protect the perovskite layer from moisture penetration from the environment. Even though PSCs based on the commonly used Spiro-OMeTAD HTM have achieved acceptable PCEs, the properties of this material are not ideal to meet the above criteria. First, Spiro-OMeTAD has a relatively low hole mobility in its original

form, and therefore additives such as lithium bis (trifluoromethanesulfonyl) imide salt (LiTFSI) and 4-tert-butylpyridine (*t*BP) should be included in Spiro-OMeTAD solution to improve hole conductivity. Secondly, these additives are hygroscopic, which makes the perovskite film sensitive to humidity from the environment. In addition, the high cost of Spiro-OMeTAD limits the industrialization potential of PSCs based on this material. This thesis intensively investigates two types of alternative HTMs for use in PSC; one is the organic, which is TPABT, and the other is the inorganic ($NiMnO_4$, $CuBi_2O_4$ and NiO).

1.3 References

[1] A.I. Osman, L. Chen, M. Yang, G. Msigwa, M. Farghali, S. Fawzy, D.W. Rooney, P.-S. Yap, Cost, environmental impact, and resilience of renewable energy under a changing climate: a review, Environmental Chemistry Letters 21(2) (2023) 741-764. https://doi.org/10.1007/s10311-022-01532-8.

[2] F. Yao, P.I. Palmer, Source Sector Mitigation of Solar Energy Generation Losses Attributable to Particulate Matter Pollution, Environmental Science & Technology 56(12) (2022) 8619-8628. https://doi.org/10.1021/acs.est.2c01175.

[3] EIA, Net electricity consumption worldwide in select years from 1980 to 2021. https://www.statista.com/statistics/280704/world-power-consumption/.

[4] N.M. Haegel, S.R. Kurtz, Global Progress Toward Renewable Electricity: Tracking the Role of Solar, IEEE Journal of Photovoltaics 11(6) (2021) 1335-1342. https://doi.org/10.1109/JPHOTOV.2021.3104149.

[5] M. Cook, Chapter 2 - Trends in global energy supply and demand, in: M. Cook (Ed.), Developments in Petroleum Science, Elsevier2021, pp. 15-42. https://doi.org/https://doi.org/10.1016/B978-0-12-821190-8.00002-2.

[6] Z. Lei, H. Zhou, W. Hu, G.P. Liu, S. Guan, X. Feng, Toward a Web-Based Digital Twin Thermal Power Plant, IEEE Transactions on Industrial Informatics 18(3) (2022) 1716-1725. https://doi.org/10.1109/TII.2021.3086149.

[7] A.M. Bagher, M.M.A. Vahid, M. Mohsen, Types of solar cells and application, American Journal of optics and Photonics 3(5) (2015) 94-113.

[8] F. Shaik, S.S. Lingala, P. Veeraboina, Effect of various parameters on the performance of solar PV power plant: a review and the experimental study, Sustainable Energy Research 10(1) (2023) 6. https://doi.org/10.1186/s40807-023-00076-x.

[9] S. Tonzani, Sun power, Nature Materials 9(1) (2010) S10-S11. https://doi.org/10.1038/nmat2645.

[10] N. Renewable, E. Laboratory, Best Research-Cell Efficiency Chart, 2023.

[11] J.Y. Tsao, S. Chowdhury, M.A. Hollis, D. Jena, N.M. Johnson, K.A. Jones, R.J. Kaplar, S. Rajan, C.G. Van de Walle, E. Bellotti, C.L. Chua, R. Collazo, M.E. Coltrin, J.A. Cooper, K.R. Evans, S. Graham, T.A. Grotjohn, E.R. Heller, M. Higashiwaki, M.S. Islam, P.W. Juodawlkis, M.A. Khan, A.D. Koehler, J.H. Leach, U.K. Mishra, R.J. Nemanich, R.C.N. Pilawa-Podgurski, J.B. Shealy, Z. Sitar, M.J. Tadjer, A.F. Witulski, M. Wraback, J.A. Simmons, Ultrawide-Bandgap Semiconductors: Research Opportunities and Challenges, Advanced Electronic Materials 4(1) (2018) 1600501. https://doi.org/https://doi.org/10.1002/aelm.201600501.

[12] C.O. Teixeira, D. Castro, L. Andrade, A. Mendes, Selection of the ultimate perovskite solar cell materials and fabrication processes towards its industrialization: A review, Energy Science & Engineering 10(4) (2022) 1478-1525. https://doi.org/https://doi.org/10.1002/ese3.1084.

[13] F. Li, W. Yu, X. Guan, T. Wu, Emerging Transistor Applications Enabled by Halide Perovskites, Accounts of Materials Research 3(1) (2022) 8-20. https://doi.org/10.1021/accountsmr.1c00103.

[14] K. Sharma, V. Sharma, S.S. Sharma, Dye-Sensitized Solar Cells: Fundamentals and Current Status, Nanoscale Research Letters 13(1) (2018) 381. https://doi.org/10.1186/s11671-018-2760-6.

[15] Y. Rong, X. Hou, Y. Hu, A. Mei, L. Liu, P. Wang, H. Han, Synergy of ammonium chloride and moisture on perovskite crystallization for efficient printable mesoscopic solar cells, Nature Communications 8(1) (2017) 14555. https://doi.org/10.1038/ncomms14555.

[16] Z. Zhou, S. Pang, Z. Liu, H. Xu, G. Cui, Interface engineering for high-performance perovskite hybrid solar cells, Journal of Materials Chemistry A 3(38) (2015) 19205-19217.

[17] Y. Wang, I. Ahmad, T. Leung, J. Lin, W. Chen, F. Liu, A.M.C. Ng, Y. Zhang, A.B. Djurišić, Encapsulation and Stability Testing of Perovskite Solar Cells for Real Life Applications, ACS Materials Au 2(3) (2022) 215-236. https://doi.org/10.1021/acsmaterialsau.1c00045.

[18] A. Farokhi, H. Shahroosvand, G. Delle Monache, M. Pilkington, M.K. Nazeeruddin, The evolution of triphenylamine hole transport materials for efficient perovskite solar cells, Chemical Society Reviews (2022).

Chapter 2. Background

2.1 Perovskite Solar Cells

Perovskite solar cells (PSCs) have newly emerged as "third generation solar cells", these are collectively supported as economically and environmentally viable renewable technology options, compared to conventional solar cell technologies, especially in tackling universal challenges in energy production, security, and environmental influences [1]. In recent years, perovskite solar cells were considered as the subject of great interest in photovoltaic research. This is due to their high absorption coefficient, long charge carrier lifetime, easy and cheap processing, as well as the ability to easily tune the band gap of perovskite and their outstanding performance [2-4]. However, besides the success of obtaining high efficiency, PSCs still face two major problems that hinders their widespread application in the energy industry. First, the most used hole-transporting material for PSCs (Spiro-OMeTAD) is too expensive for industrialisation [5, 6]. Secondly, organic-inorganic halide perovskite as an ionic solid is very sensitive to moisture from the atmosphere, which can cause a rapid degradation if the perovskite film if not properly protected [7].

2.1.1 Halide Perovskite Materials

Perovskite originally refers to a calcium titanium oxide mineral species with the chemical formula of ($CaTiO_3$), which was discovered by Gustav Rose in 1839 [2]. The general chemical formula of perovskite crystals is ABX_3, (A can be an organic or an inorganic cation such as: Methylammonium ($CH_3NH_3^+$, MA), Formamidinium ($CH(NH_2)_2^+$), FA), Cs^+ or Rb^+, B is a divalent cation: Pb(II) or Sn(II), X : Halogen anion (Cl^-, Br^- and I^-) or (SCN^-))[8] [9]is as shown below in (Figure 2.1).

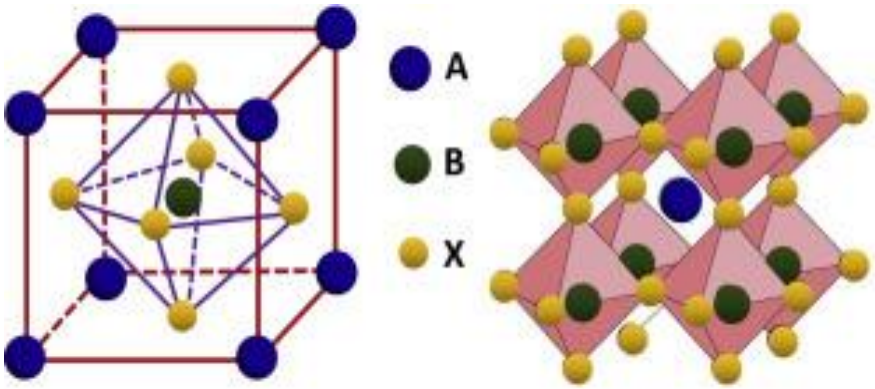

Figure 2.1. Crystalline structure of perovskite ABX_3, A: MA or FA cation, B: Pb^{2+} cation, X: Cl^-, Br^- or I^- anion [9].

2.1.2 The Development of the Perovskite Solar Cell

Perovskite Solar cells (PSC) were first established on mesoporous TiO_2 photoanodes which were sensitized with $CH_3NH_3PbX_3$ (X=I) by Miyasaka in 2009 [4]. The methylammonium iodine only yielded a PCEs of 3.81%, and liquid electrolyte configuration degraded promptly within minutes.

In 2012, Snaith and Miyasaka exhibited a "meso-super structured" solar cell, which featured an inert scaffold like Al_2O_3 with coated $CH_3NH_3Pbl_{3-x}Cl_x$ and Spiro-OMeTAD in place of previously used n-type mesoporous oxide. This non-sensitization PSC produced enhanced V_{OC} values, up to 1.13 V, and a PCE of 10.9% [4]. Advances in cell fabrication in 2013 increased efficiency of solar cells consisting of organometal halide perovskite to over 15%, Liu and his colleagues showcased a PCE of 15.4% in planar heterojunction PVC with vapor deposition fabrication [5]. Meanwhile, Gratzel and his colleagues produced a m-TiO_2 film fabricated perovskite using sequential deposition methods, which had a PCE of 15%. A PCE of 22.1% was achieved in March 2016 by the Korean Research Institute of Chemical Technology, and more recently in 2018 a 4-terminal all-perovskite tandem solar cell by Zhao and colleagues generated a PCE of 25.8% [6]and reached to 26% in 2023[10].

2.1.3 How Perovskite Solar Cells Operate

Figure 2.2 provides an overview of the typical layer structure for a PSC. This comprises a transparent electrode on a glass surface, usually indium tin oxide (ITO) or fluorine doped in oxide (FTO) with an electron transporting layer (ETL) on top of it. The PSC also contains of a hole-transporting layer (HTL) and a metallic electrode [11, 12]. Figure 2.2 also provides a schematic overview of the PSC process. The electrons are transported to electrodes via the ETL, and holes are transported within the hole transporting material to the back electrode. This is due to the specific configuration of the Highest Occupied Molecular Orbital (HOMO) and Lowest Unoccupied Molecular Orbital (LUMO) energy levels that align with the valence band maximum and conduction band minimum within the perovskite. After the separation of the carriers has occurred, the electron passes through the wire linking these two electrodes and the moving electrons subsequently result in a current being produced [8-9]. The hole transporting material will be discussed in detail in the following section.

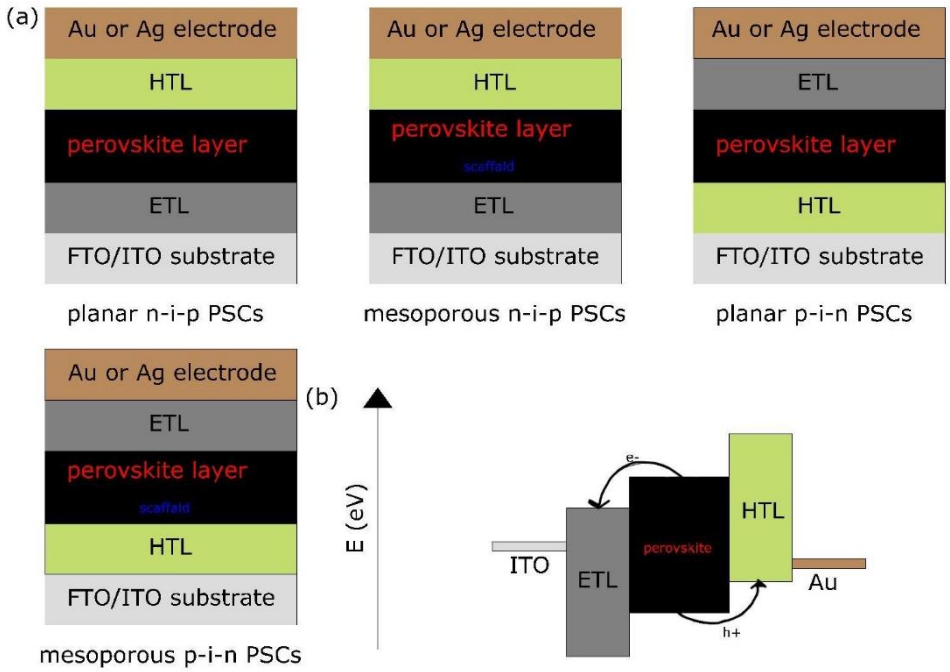

Figure 2.2. An illustration of a typical perovskite solar cell (a) the conventional (n-i-p) and inverted (p-i-n) structure and (b) energy level scheme for transporting direction of the electron and hole carriers in n-i-p perovskite [13].

Perovskites maintain an ambipolar behavior with n- and p-type conduction which permits two distinctive device architectures. Conventional n–i–p devices can be divided into mesoscopic (in

which the perovskite is infiltrated into a mesoporous scaffold of a metal oxide (TCO or FTO/c-TiO_2/m-TiO_2/perovskite/HTM/metal) and planar heterojunction (TCO or FTO/ETM/perovskite/HTM/metal), in which the perovskite is sandwiched between electron- and hole selective contacts structures. Both concepts have been transferred to the so-called inverted architectures (p–i–n), in which the aforementioned stack is inverted (TCO/HTM/perovskite/ ETM/metal) [8-9] (Figure 2.2).

2.2 Hole Transporting Materials (HTM) in Perovskite Solar Cells

HTM contained within PSCs are fundamental to their function, however, these can often be expensive with an anticipated cost for spiro-OMeTAD being approximately 90 $/g [14]. In regular structured PSCs where the HTM is placed on top of the perovskite layer, HTMs undertake a variety of imperative roles which include (i) proficient extraction of the photogenerated holes, thus improving transport to the counter-electrode and assisting in blocking the electron transfer to the anode; (ii) refining device stability by inhibiting direct contact between the perovskite and electrode (classically Au, Ag and Al) and safeguarding against the dispersal of the electrode into the perovskite layer (iii) ensuring constant coverage of the perovskite layer to subdue the charge recombination losses between the perovskite and HTM interface; and (iv) influencing open circuit voltage (with existence of dopants within the HTM layer, a diminished energy disorder within the HTM layer in relation to the chemical structure, and by the variable mobility and conductivity values of the HTM)[15, 16]. To achieve its full potential as a PSC, an HTM must satisfy certain fundamental requirements, a compatible highest occupied molecular orbital (HOMO) energy level to the perovskite VB energy level, an adequate hole mobility and both thermal and photochemical stability [17]. Organic and inorganic hole-conductors are among the numerous HTMs which have been analysed and integrated into PSCs. Organic hole-conductors can be classified as small molecule hole-conductors or conducting polymers such as P3HT, PTAA and PEDOT [18]. In addition, alternative inorganic HTMs such as NiO and Cul have been shown to generate efficient perovskite solar cells [19, 20]. Figure 2.3 shows the energy levels for HTMs typically used in PSCs.

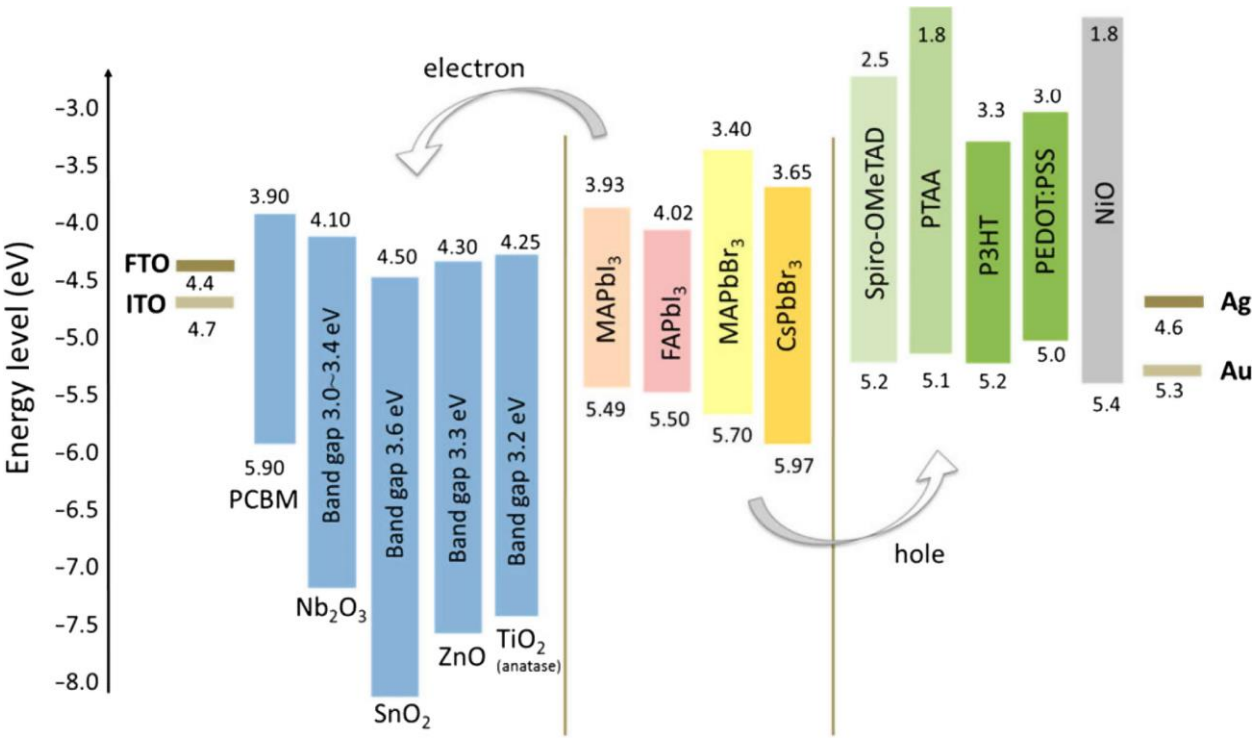

Figure 2.3. Schematic display of energy levels for HTMs which are often used in PSCs [21].

The most widely used hole conducting material in PSCs is Spiro-OMeTAD, which has a moderately small hole mobility and so consistently has lithium bis(trifluoromethanesulfonyl)imide (LiTFSI) and 4-tert-butylpyridine (tBP) integrated within the solution to enrich the hole conductivity. Though the price of this material is more than ten times the value of gold and platinum, it is still sensitive to environmental moisture due to the hygroscopic identity of the additives.

2.2.1 Organic Hole Transporting Materials

In the conventional (n-i-p) and inverted (p-i-n) perovskite solar cells (PSCs), organic hole transport materials (HTMs) are widely employed due to their compatibility with low-temperature solution processes and the ability to finely adjust their properties through molecular design. Organic HTMs can be categorised into two types: polymer HTMs and a growing class of small-molecule HTMs based on their molecular weight. Examples of common polymer HTMs used in PSCs include 2,2',7,7'-tetrakis(N,N-di-p-methoxyphenyl-amine)9,9'-Spirobifluorene(SpiroOMeTAD), poly(3,4-ethylenedioxythiophene):poly(styrenesulfonate)(PEDOT:PSS),poly(N,N’-bis(4-butylphenyl)-

N,N'-bis(phenyl)benzidine)(poly-TPD) and poly(bis(4-phenyl)(2,4,6-trimethylphenyl)amine) (PTAA)[22].

Spiro-OMeTAD is a highly amorphous HTM with a high glass transition temperature (Tg) and appropriate energy levels, making it a dominant choice among various HTMs for perovskite solar cells (PSCs). However, the pristine form of spiro-OMeTAD has a relatively low hole mobility of about 2 x 10^{-4} cm^2 V^{-1} s^{-1}, as calculated using the space charge limited current (SCLC) model. This can be significantly improved by incorporating optimal amounts of Li-TFSI and *t*BP. The enhancement in hole mobility can be attributed to increased disorder and a broadened tail of the density of states induced by the presence of Li^+, while *t*BP dopants improve the solubility of Li-TFSI and enhance the uniformity of the spiro-OMeTAD film[23].

In addition, the electrical conductivity of doped spiro-OMeTAD can be further increased by incorporating small amounts of cobalt- or antimony-based salts, such as tris(2-(1H-pyrazol-1-yl)-4-tert-butylpyridine)cobalt(III) tris-(bis(trifluoromethylsulfonyl)imide)) (FK209) and $N(PhBr)_3SbCl_6$, in combination with Li-TFSI and tBP. These suitable additives have led to significant improvements in the power conversion efficiency (PCE) of PSCs based on spiro-OMeTAD[24]. Continuous optimisation of the light-absorbing materials and processing techniques has further contributed to the widespread use of doped spiro-OMeTAD as the preferred HTM in PSCs. Notably, in 2014, Jeon *et al*. synthesized derivatives of spiro-OMeTAD with methoxy substituents located in different positions and doping them with Li-TFSI and *t*BP resulted in mesoporous PSCs with a significantly higher PCE of up to 16.7%[3]. Similarly, in 2016, Bi *et al.* achieved a maximum PCE of 20.8% and an open-circuit voltage of 1.18 V in mesoporous PSCs by using spiro-OMeTAD doped with Li-TFSI, *t*BP, and FK209[3]. Furthermore, in 2017, Jiang et al. demonstrated that a moderate residual amount of PbI_2 in spiro-OMeTAD-based devices could provide stable and high PCEs, reaching 21.6% and 20.1% in small and large planar PSCs, respectively. In 2019, Jiang *et al*. utilised phenethyl ammonium iodide (PEAI) to reduce defects and suppress non-radiative recombination on the perovskite surface, resulting in a certified PCE of 23.32% and a V_{OC} of 1.18 V in planar PSCs with doped spiro-OMeTAD[3]. Apart from typical organic-inorganic hybrid PSCs, spiro-OMeTAD has also been employed in PSCs using new light-absorbing materials or processing techniques. For instance, a scalable sheet-to-sheet slot die coating process was developed in 2017, yielding a large-area module with a PCE above 10% and a power output of 1.7 W[3].

Second common HTM after spiro-OMeTAD is PEDOT:PSS (Figure 2.4 (b)) faces challenges such as an energy level mismatch with perovskites and the high acidity of the PSS chain. Poly-TPD exhibits issues related to non-wettability and high cost. The efficiency of inverted PSCs based on these HTMs is insufficient, limiting their application in high-efficiency inverted devices.

PTAA (Figure 2.4 (c)) also suffers from non-wettability and a high cost, similar to poly-TPD. However, it has been successfully employed in improving the efficiency of inverted PSCs due to its more suitable energy level alignment with the perovskite layer, excellent conductivity, chemical neutrality, and high optical transmittance[5]. Presently, the efficiency of inverted PSCs based on PTAA has surpassed 25%[5, 25]. To address these concerns, Zhang et al. investigated PTAA with different molecular weights (MW) to examine their surface properties and their impact on the upper perovskite films. It was observed that PTAA with a molecular weight of 25000 exhibited the best performance, achieving a record efficiency of 18.11% with minimal hysteresis. These findings suggest that inverted PSCs based on non-doped PTAA can also exhibit excellent performance, offering an alternative approach without the need for expensive dopants and the added complexity of device fabrication [25].

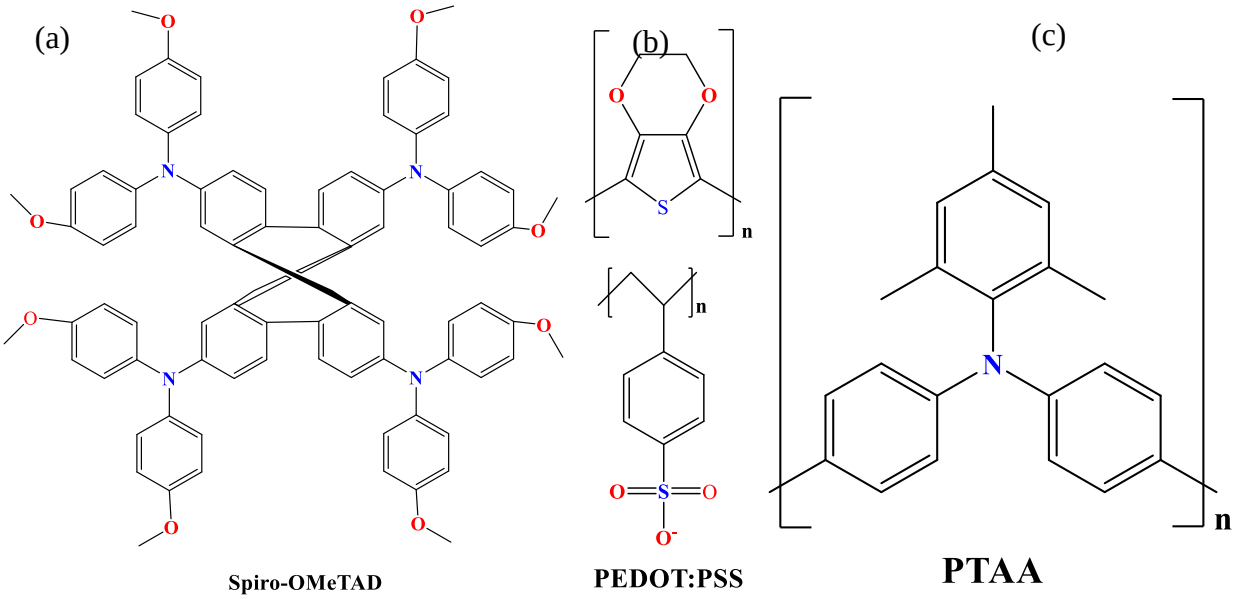

Figure 2.4. Chemical structures of (a) spiro-OMeTAD, (b) PTAA and (c) PEDOT: PSS.

New generation amide based HTM was published by Petrus, *et al.* [26]. The EDOT-Amide-TPA which is based on amide-functionalized small molecules was synthesised using simple and low-cost condensation reaction. The material showed excellent thermal and chemical stability. The HTM also exhibits fast and efficient hole extraction from the perovskite layer, leading to improved power conversion efficiencies and device stability. The authors demonstrate that the amide bond in the HTM plays a key role in enhancing the charge transport properties and preventing the migration of additives. This work introduces a novel design strategy for low-cost and high-performance HTMs for perovskite solar cells.

2.2.2 Inorganic Hole Transporting Materials

Despite the impressive power conversion efficiency (PCE) demonstrated by perovskite solar cells (PSCs) utilising typical organic hole transport materials (HTMs), their stability remains a significant challenge. To address this issue, one approach is to employ dopant-free organic HTMs, as they offer improved stability. However, an even more effective strategy involves utilising inorganic materials as HTMs [27].

The challenges faced by organic hole transport materials (HTMs) in inverted perovskite solar cells (PSCs), such as hydrophobicity, high raw material costs, and potential degradation, limit their application and commercialization. In contrast, inorganic HTMs have garnered significant attention due to their excellent long-term and thermal stability. Among these inorganic HTMs, metal oxides based on nickel oxide (NiO_x) have shown remarkable success in inverted PSCs and have been extensively studied. This is primarily due to their favourable energy level alignment with most perovskite absorbers, excellent stability, and ease of synthesis and deposition[27].

NiOx, in its stoichiometric form, is an insulator. However, the conductivity of NiO_x relies heavily on the presence of intrinsic Ni vacancies, which act as self-doping agents by introducing Ni_3^+ ions. Manipulating the thickness of NiO_x becomes crucial to managing the increased series resistance caused by these Ni vacancies. Nevertheless, undoped NiO_x exhibits low conductivity due to the high ionisation energy of the Ni vacancies, which affects the hole charge density. To address this issue, various metal cations such as Ag^+, Au^+, Cu^{2+}, Cs^+, K^+, and specific molecules have been doped into NiO_x. This doping strategy aims to enhance the conductivity and adjust the energy level by modulating the concentration of Ni vacancies[3].

Han *et al.* proposed a heavily p-doped (p+) $Ni_xMg_yLi_{1-x-y}O$ co doping approach, where 15 mol% Mg^{2+} was doped into 5 mol% Li^+-doped NiO_x. This co-doping compensated for the positive shift in the valence band maximum caused by Li^+ doping in the NiO_x lattice. As a result, the $Li_{0.05}Mg_{0.15}Ni_{0.8}O$ film exhibited a significantly improved conductivity of 2.32×10^{-3} S cm^{-1}, approximately 12 times higher than that of the undoped sample. This enhancement in conductivity led to a notable reduction in series resistance and an increase in shunt resistance, which is advantageous for manufacturing large-area (>1 cm^2) PSCs[3].

Consequently, the implementation of this co-doping strategy resulted in the achievement of a world-record efficiency for large-area (>1 cm^2) PSCs at that time. Specifically, a large-area PSC with a high-power conversion efficiency (PCE) of 16.2% (certified 15%) was obtained, demonstrating the effectiveness of the $Li_xMg_yNi_{1-x}O_y$ co-doping approach for scalable PSCs [28]. Inspired by this technique, Chen *et al*. conducted a systematic investigation of the impact of doping several molecules with high electron affinity, similar to F_6TCNNQ, into NiO_x. Among these molecules, 3,6-difluoro-2,5,7,7,8,8-hexacyanoquinodimethane (F_2HCNQ) exhibited the highest electron affinity (EA), promoting charge transfer from the VBM of NiO_x to the LUMO of the molecules. The increased work function (WF) and valence band (VB) resulting from the high EA facilitated more favourable energy level alignment at the NiO_x/perovskite interfaces. Consequently, interfacial hole extraction was accelerated with reduced energy loss. This led to the ground-breaking achievement of an efficiency exceeding 22% for the first time in inverted PSCs based on F_2HCNQ-NiOx fabricated through a low-temperature process[28].

Although inverted PSCs based on NiO_x have demonstrated impressive results, their record PCEs still fall behind those of PTAA- or SAM-based PSCs. Several reasons can account for this discrepancy: Firstly, the presence of abundant surface defects and an energy level mismatch at the NiO_x/perovskite interface leads to a significant energy offset, exacerbating interfacial carrier recombination and hindering charge carrier extraction. Secondly, the high-oxidative-state Ni^{3+} can react with A-site cation salts, forming $PbI_{2-x}Br_x$ and resulting in the accumulation of A-site defects and $PbI_{2-x}Br_x$-rich perovskite at the NiO_x/perovskite interface. This creates a barrier for hole extraction and induces noncapacitive hysteresis. Lastly, light-induced deprotonation at the NiO_x/perovskite interface leads to the generation of interfacial voids and vacancies, shallow-level defects, and substantial ion movement, thereby diminishing overall efficiency[3].

Despite these challenges, NiO_x-based inverted PSCs, which represent the most promising inorganic HTM, have achieved impressive outcomes, including a certified PCE of 23.91%. Subsequent efforts have been dedicated to enhancing the efficiency and stability of inverted PSCs based on NiO_x, which will be discussed further.

Other p-type materials were considered. Liu, *et al.* [29] investigate the use of copper thiocyanate (CuSCN) as a hole-transporting material, which is cheaper and more thermally robust than the commonly used Spiro-OMeTAD. However, they discover that CuSCN causes a critical interfacial instability with the perovskite layer, leading to accelerated degradation under high temperature. They propose a mechanism for this degradation and show that it can be mitigated by coating the devices with a thin layer of poly(methyl methacrylate) (PMMA), which acts as an on-cell encapsulation. They demonstrate that this simple strategy improves the thermal stability of the devices in air, retaining 77% of their initial efficiency after 1080 hours at 85 °C.

2.3 References

[1] V. Romano, A. Agresti, R. Verduci, G. D'Angelo, Advances in Perovskites for Photovoltaic Applications in Space, ACS Energy Letters 7(8) (2022) 2490-2514. https://doi.org/10.1021/acsenergylett.2c01099.

[2] A.S.R. Bati, Y.L. Zhong, P.L. Burn, M.K. Nazeeruddin, P.E. Shaw, M. Batmunkh, Next-generation applications for integrated perovskite solar cells, Communications Materials 4(1) (2023) 2. https://doi.org/10.1038/s43246-022-00325-4.

[3] S. Li, Y.-L. Cao, W.-H. Li, Z.-S. Bo, A brief review of hole transporting materials commonly used in perovskite solar cells, Rare Metals 40(10) (2021) 2712-2729. https://doi.org/10.1007/s12598-020-01691-z.

[4] M.A. Afroz, A. Singh, R.K. Gupta, R. Garai, N.K. Tailor, Yukta, S. Choudhary, B. Sharma, P. Mahajan, B. Padha, S. Verma, S. Arya, V. Gupta, S. Akin, D. Prochowicz, M.M. Tavakoli, S.P. Singh, P.K. Iyer, P. Yadav, H. Hu, G. De, S. Satapathi, Design potential and future prospects of lead-free halide perovskites in photovoltaic devices, Journal of Materials Chemistry A 11(25) (2023) 13133-13173. https://doi.org/10.1039/D2TA07687J.

[5] S. Liu, V.P. Biju, Y. Qi, W. Chen, Z. Liu, Recent progress in the development of high-efficiency inverted perovskite solar cells, NPG Asia Materials 15(1) (2023) 27. https://doi.org/10.1038/s41427-023-00474-z.

[6] F. Lin, J. Luo, Y. Zhang, J. Zhu, H.A. Malik, Z. Wan, C. Jia, Perovskite solar cells: Li–TFSI and t-BP-based chemical dopant engineering in spiro-OMeTAD, Journal of Materials Chemistry A 11(6) (2023) 2544-2567. https://doi.org/10.1039/D2TA08597F.

[7] D. Zhang, D. Li, Y. Hu, A. Mei, H. Han, Degradation pathways in perovskite solar cells and how to meet international standards, Communications Materials 3(1) (2022) 58. https://doi.org/10.1038/s43246-022-00281-z.

[8] J. Jiang, F. Liu, I. Tranca, Q. Shen, S. Tao, Atomistic and Electronic Origin of Phase Instability of Metal Halide Perovskites, ACS Applied Energy Materials 3(12) (2020) 11548-11558. https://doi.org/10.1021/acsaem.0c00791.

[9] B. Ai, Z. Fan, Z.J. Wong, Plasmonic–perovskite solar cells, light emitters, and sensors, Microsystems & Nanoengineering 8(1) (2022) 5. https://doi.org/10.1038/s41378-021-00334-2.

[10] Best Research-Cell Efficiency Chart.

[11] R. Wang, M. Mujahid, Y. Duan, Z.-K. Wang, J. Xue, Y. Yang, A Review of Perovskites Solar Cell Stability, Advanced Functional Materials 29(47) (2019) 1808843. https://doi.org/https://doi.org/10.1002/adfm.201808843.

[12] S.S. Shin, S.J. Lee, S.I. Seok, Metal Oxide Charge Transport Layers for Efficient and Stable Perovskite Solar Cells, Advanced Functional Materials 29(47) (2019) 1900455. https://doi.org/https://doi.org/10.1002/adfm.201900455.

[13] I.G. Sonsona, M. Carrera, M. Más-Montoya, R.S. Sánchez, P. Serafini, E.M. Barea, I. Mora-Seró, D. Curiel, 2D-Self-Assembled Organic Materials in Undoped Hole Transport Bilayers for Efficient Inverted Perovskite Solar Cells, ACS Applied Materials & Interfaces 15(18) (2023) 22310-22319. https://doi.org/10.1021/acsami.2c23010.

[14] Deepika, A. Singh, U.K. Verma, A. Tonk, Device Structures of Perovskite Solar Cells: A Critical Review, physica status solidi (a) 220(9) (2023) 2200736. https://doi.org/https://doi.org/10.1002/pssa.202200736.

[15] T. Wu, D. Zhang, Y. Ou, H. Ma, A. Sun, R. Zhao, L. Zhu, R. Wang, R. Zhuang, G. Liu, Y. Zhao, Q. Lai, Y. Hua, Efficient perovskite solar cells enabled by large dimensional structured hole transporting materials, Journal of Materials Chemistry A 9(3) (2021) 1663-1668. https://doi.org/10.1039/D0TA10449C.

[16] M. Vasilopoulou, A. Fakharuddin, A.G. Coutsolelos, P. Falaras, P. Argitis, A.R.b.M. Yusoff, M.K. Nazeeruddin, Molecular materials as interfacial layers and additives in perovskite solar cells, Chemical Society Reviews 49(13) (2020) 4496-4526. https://doi.org/10.1039/C9CS00733D.

[17] M. Vasilopoulou, A. Soultati, P.-P. Filippatos, A.R.b. Mohd Yusoff, M.K. Nazeeruddin, L.C. Palilis, Charge transport materials for mesoscopic perovskite solar cells, Journal of Materials Chemistry C 10(31) (2022) 11063-11104. https://doi.org/10.1039/D2TC00828A.

[18] X. Jiang, Z. Yu, Y. Zhang, J. Lai, J. Li, G.G. Gurzadyan, X. Yang, L. Sun, High-Performance Regular Perovskite Solar Cells Employing Low-Cost Poly(ethylenedioxythiophene) as a Hole-Transporting Material, Scientific Reports 7(1) (2017) 42564. https://doi.org/10.1038/srep42564.

[19] J. Chen, N.-G. Park, Inorganic Hole Transporting Materials for Stable and High Efficiency Perovskite Solar Cells, The Journal of Physical Chemistry C 122(25) (2018) 14039-14063. https://doi.org/10.1021/acs.jpcc.8b01177.

[20] R. Rajeswari, M. Mrinalini, S. Prasanthkumar, L. Giribabu, Emerging of Inorganic Hole Transporting Materials For Perovskite Solar Cells, The Chemical Record 17(7) (2017) 681-699. https://doi.org/https://doi.org/10.1002/tcr.201600117.

[21] Z. Ahmad, A. Mishra, S.M. Abdulrahim, D. Taguchi, P. Sanghyun, F. Aziz, M. Iwamoto, T. Manaka, J. Bhadra, N.J. Al-Thani, M.K. Nazeeruddin, F. Touati, A. Belaidi, S.A. Al-Muhtaseb, Consequence of aging at Au/HTM/perovskite interface in triple cation 3D and 2D/3D hybrid perovskite solar cells, Scientific Reports 11(1) (2021) 33. https://doi.org/10.1038/s41598-020-79659-3.

[22] P. Yan, D. Yang, H. Wang, S. Yang, Z. Ge, Recent advances in dopant-free organic hole-transporting materials for efficient, stable and low-cost perovskite solar cells, Energy & Environmental Science 15(9) (2022) 3630-3669. https://doi.org/10.1039/D2EE01256A.

[23] Q. Fu, X. Tang, H. Liu, R. Wang, T. Liu, Z. Wu, H.Y. Woo, T. Zhou, X. Wan, Y. Chen, Y. Liu, Ionic Dopant-Free Polymer Alloy Hole Transport Materials for High-Performance Perovskite Solar Cells, Journal of the American Chemical Society 144(21) (2022) 9500-9509. https://doi.org/10.1021/jacs.2c04029.

[24] Z. Hawash, L.K. Ono, Y. Qi, Recent Advances in Spiro-MeOTAD Hole Transport Material and Its Applications in Organic–Inorganic Halide Perovskite Solar Cells, Advanced Materials Interfaces 5(1) (2018) 1700623. https://doi.org/https://doi.org/10.1002/admi.201700623.

[25] Q. Zhao, R. Wu, Z. Zhang, J. Xiong, Z. He, B. Fan, Z. Dai, B. Yang, X. Xue, P. Cai, S. Zhan, X. Zhang, J. Zhang, Achieving efficient inverted planar perovskite solar cells with nondoped

PTAA as a hole transport layer, Organic Electronics 71 (2019) 106-112. https://doi.org/https://doi.org/10.1016/j.orgel.2019.05.019.

[26] M.L. Petrus, K. Schutt, M.T. Sirtl, E.M. Hutter, A.C. Closs, J.M. Ball, J.C. Bijleveld, A. Petrozza, T. Bein, T.J. Dingemans, T.J. Savenije, H. Snaith, P. Docampo, New Generation Hole Transporting Materials for Perovskite Solar Cells: Amide-Based Small-Molecules with Nonconjugated Backbones, Advanced Energy Materials 8(32) (2018) 1801605. https://doi.org/https://doi.org/10.1002/aenm.201801605.

[27] X. Cai, T. Hu, H. Hou, P. Zhu, R. Liu, J. Peng, W. Luo, H. Yu, A review for nickel oxide hole transport layer and its application in halide perovskite solar cells, Materials Today Sustainability 23 (2023) 100438. https://doi.org/https://doi.org/10.1016/j.mtsust.2023.100438.

[28] Y.-H. Li, X. Lu, R. Wang, Y.-Y. Ma, S. Duhm, M.-K. Fung, Cu-Doped nickel oxide prepared using a low-temperature combustion method as a hole-injection layer for high-performance OLEDs, Journal of Materials Chemistry C 5(45) (2017) 11751-11757. https://doi.org/10.1039/C7TC03884D.

[29] J. Liu, S.K. Pathak, N. Sakai, R. Sheng, S. Bai, Z. Wang, H.J. Snaith, Identification and Mitigation of a Critical Interfacial Instability in Perovskite Solar Cells Employing Copper Thiocyanate Hole-Transporter, Advanced Materials Interfaces 3(22) (2016) 1600571. https://doi.org/https://doi.org/10.1002/admi.201600571.

Chapter 3. Experimental Methods

3.1 Characterisation Techniques

We have utilised many electrical and structural characterization techniques to investigate the crystal structure, morphology of the deposited thin films, and to calculate the photovoltaic performance of fabricated solar cells. Structural characterization techniques such as scanning electron microscope (SEM), atomic force microscopy (AFM) and X-ray diffraction (XRD); for optical and electrical properties, the characterization techniques like; UV-visible spectrophotometer, current-voltage (I-V) test with the solar simulator.

3.1.1 UV-Vis Spectrophotometer

The absorbance and transmittance of coated thin films were recorded by a Perkin Elmer Lambda 1050 double beam UV-Vis spectrophotometer.

The operational principle of this spectrophotometer is based on the Beer Lambert law. ***Lambert's law***: The percentage of light absorbed by the given medium is not dependent on the light intensity. The successive layers of equal thickness will transmit an equal proportion of incident light[1]. For the absorption of a photon, the energy of the photon has to be high enough to excite an electron from its ground state to the excited state and corresponds to at least the energy difference these two states or more. ***Beer's Law***: The absorption of light is depending on both thickness of the sample and concentration of the material medium. Therefore, absorbance A is expressed by the Lambert-Beer Law[2]:

$$A = -\log(\frac{I}{I_0}) = \varepsilon\, c\, d \qquad \text{Equation 1}$$

Where I is the intensity of transmitted light, I_o is the intensity of the incident light, ε is the molar absorptivity ($dm^3\ mol^{-1}\ cm^{-1}$), c is molar concentration (mol. dm^{-3}), and d is path length (cm). It is to be noted that ε is a function of wavelength and therefore the Lambert- Beer law applicable to a single wavelength of light.

Since the law does not consider external factors like the reflection of the light at interfaces between two media, measurements with an integrating sphere and a reference have to be performed to correct these effects. For UV-Vis measurements, the spectral range is scanned in a defined step

size and first the transmission (%T) of the light and afterwards the reflectance (%R) of the investigated substrates are measured. It is important to use a reference that is containing the solvent or the architecture of the measured liquid sample. And in case of thin film samples, we have to take the pristine substrate as a reference. To obtain the percentage absorbance (%A) of the sample, following equation can be used:

$$\%A = 1 - \%T - \%R \qquad \text{Equation 2}$$

3.1.2 X-Ray Diffraction (XRD)

XRD is a very powerful investigative technique for finding the phase of the crystalline material and provide information on the dimensions of the unit cell. This technique is generally used in solid state physics, chemistry, biophysics, biochemistry, materials science and in many other fields. In the present study, we have used XRD for finding the phase and crystal structure of the spin coated and doctor-blade thin film material. The schematic diagram of the glancing angle X-ray diffractometer is shown in Figure 3.1

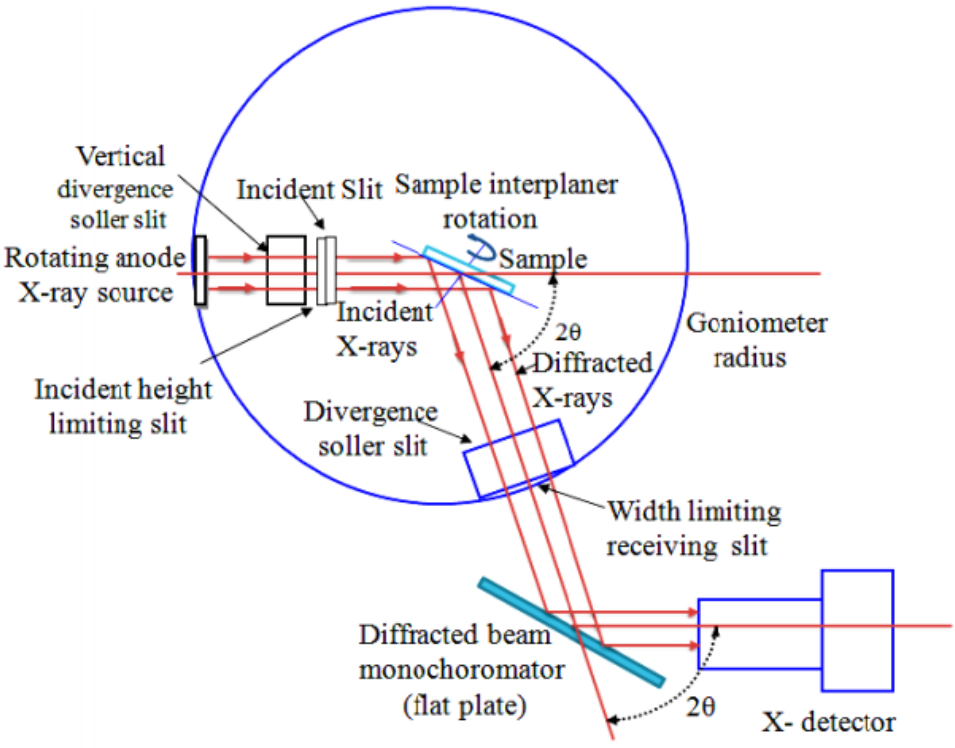

Figure 3.1. Schematic diagram of the glancing angle X-ray diffractometer[3].

Working Principle: In 1912, Max von Laue discovered that crystalline substances which act as 3-D diffraction gratings for the X-ray wavelengths that is similar to the spacing of planes in a crystal structure[4]. The schematic diagram showing the principle of XRD is given in Figure 3.1. The XRD pattern is based on the constructive interference between monochromatic X-rays and crystalline sample. These X-rays will be generated in a cathode ray tube (CRT), then filtered to produce monochromatic radiation, concentrated and directed towards the sample. The interaction of X-rays with the given sample produces constructive interference when conditions satisfy the Bragg's law ($n\lambda = 2d \sin\theta$)[5]. It relates the wavelength (λ) of X-rays to diffraction angle (θ) and distance (d) between two successive planes (lattice spacing) in a crystal structure. These diffracted X-rays are then detected, processed and counted. By scanning the sample in a range of 2θ angles, all possible diffraction directions of the lattice crystal structure can be attained due to the random orientation of individual atoms in a crystal structure. Thus, the conversion of all diffraction peaks into d-spacing allows the identification of a crystal structure. It is known that each crystal structure has a set of unique d-spacing, and typically the identification is achieved by comparison of obtained d-spacing with the standard reference diffraction patterns.

3.1.3 Thermogravimetric Analysis (TGA)and Differential Scanning Calorimetry (DSC)

To characterise the thermal properties of the compounds, TGA and DSC were used, which was performed using an STA 6000(Perkin Elmer), under a nitrogen atmosphere, with a scan rate of 5 °C per min. Differential scanning calorimetry (DSC) was performed under a nitrogen atmosphere using Ta Instruments with a heating rate in the range of 5 °C per min. To do so, a sample is heated at constant rate to a high temperature (e.g., 900°C), the mass is measured by using a simultaneous thermobalance. During the measurements, constant gas-flow of a chosen gas such as nitrogen is used to desorb volatile components, such as solvents by simultaneous thermobalance. It is furthermore possible to do differential scanning calorimetry measurements to obtain not only the mass difference of the sample but also endothermic effect for getting structural differences that are not indicated by a loss of mass (melting point). Using this characterization technique, the melting temperature (T_m), the glass-transition temperature (T_g). These are important variables for materials that are used in solar devices since the working temperatures can exceed 80°C [6].

3.1.4 Cyclic Voltammetry (CV)

Cyclic voltammetry is an analytical potentiodynamic technique that allows the study of the electrochemical behavior of a material. This measurement is usually performed by dissolving a low concentration of analyte (a few mM) in a solution with an inert supporting electrolyte. In this solution, the counter electrode, working, and reference electrodes are immersed. For the measurement, a triangular potential is applied to the working electrode, meaning that it is changing linearly over time and with a fixed scan rate, starting from an initial potential at time t_1 to a switching potential at time swept back to the original value time[7].

When the material has accessible oxidation states, an anodic current will appear on the positive scan while a cathodic current will appear on the negative back scan. The faster the redox reaction, the more symmetric is the reduction and oxidation peak of the CV-diagram. To measure organic molecules, an internal calibrant (e.g., Ferrocene) is usually added in order to improve the accuracy of the results. Using the onset of the first oxidation (in case if there are more than one oxidation states) gives the HOMO energy level of the characterized compound using formula:

$$E_{HOMO} = -(E_{(onset,ox\ vs\ Fc+/Fc} + 5.1) \qquad \text{Equation 3}$$

Therefore, this characterization method is a very valuable tool to determine the HOMO-energy level of hole-transporting materials (HTM). So, energy level alignment of HTM HOMO-level with absorber layer like perovskite can be checked before the fabrication of devices.

3.1.5 Profilometry

Profilometry is an easy and fast method to determine the film thickness of an investigated sample and is based on the principle of scannng force microscopy (SFM). SFM is based on the interaction of a probe, which is normally a sharp tip, and the sample surface. The interactions between the probe and the sample can be van-der-Waals forces, dipole interactions ,magnetic forces and contact interactions. To measure the sample, a cantilever is brought into contact with the sample and scans this sample. To measure the sample , a cantilever is brought into contact with the sample and scans this sample. To maintain an imaging parameter, a laser is focused on the cantilever, measring the deflection of the tip due to changes in the morphology of the sample. The reflected laser beam is detected by a four-quadrant photodiode that is translating the signal into a forzce using the following equation:

$$F_N = K_N \, \Delta z \qquad \text{Equation 4}$$

F_N is the force, k_N is the spring constant of the cantilever and Δz is the deflection of the cantilever. In a profilometer, the probe is in direct contact with the sample and the surface is measured by scanning over it with a specific contact force. The surface topography is measured by moving the probe along the surface and using the force feedback from the surface. A feedback system is used to keep the arm on a setpoint so the changes in the z position can be used for the reconstruction of the surface. The analog signal is afterwards translated into a digital signal[8].

3.1.6 Scanning Electron Microscopy (SEM)

Scanning electron microscopy allows the imaging of micro and nanostructures of the investigated materials. The principle is based on the use of electrons with a smaller De-Broglie wavelength than photons that are used in optical microscopes. Therefore, a high resolution of the images in the range of nanometers can be achieved. The setup is shown in Figure 3.2. The principle of this characterization method is based on the interaction of electrons with the atoms of the sample. Amongst many other effects, this interaction is causing the formation of secondary electrons that are created by the absorption of the electron beam in the sample. The secondary electrons (SE) with a smaller energy of (10-50 eV) can be detected by an SE detector that is placed at a certain angle to the sample holder. The amount of secondary electrons reaching the detector is highly dependent on the different heights, surface orientations and the composition of the illuminated spot. Therefore, by screening the sample surface step by step, it is possible to generate a microscopic picture of the material, using the different intensities of the created secondary electrons. In a SEM setup, the electron beam is created by an electron gun in high vacuum with a voltage of 3 to 30 kV using a heated tungsten filament. The electrons are accelerated using an aperture-like anode and the beam is focused by condenser lenses and objective lenses to decrease the beam diameter to a few nanometers. The SE detector is an Everhat-Thornley photomultiplier detector. Backscattered electrons which are highly energetic can be detected using a semiconductor[10].

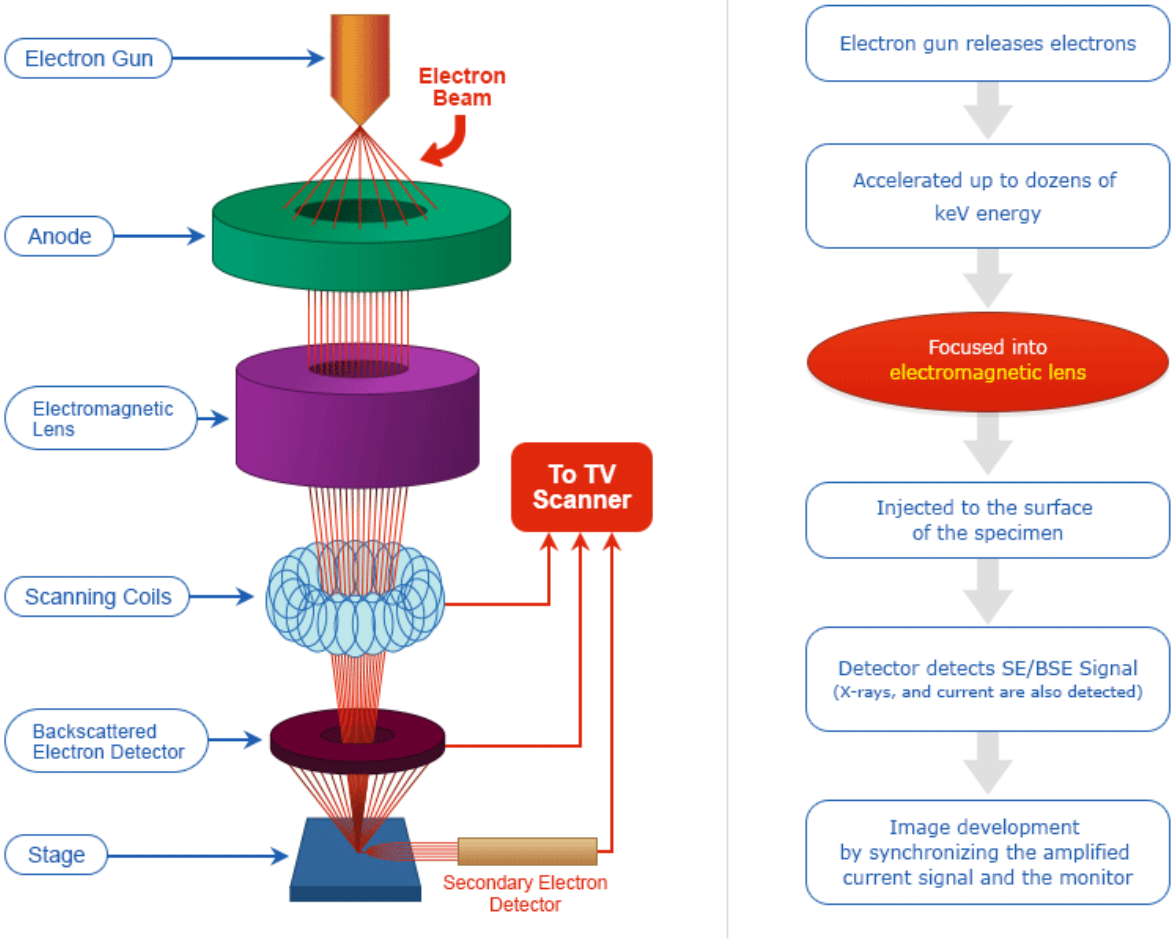

Figure 3.2. Schematic of SEM setup[9].

3.1.7 Current-Voltage Measurements

Solar devices are often compared by their power efficiency. To ensure comparable results of solar devices between different laboratories, the devices are characterised by measuring their current-voltage properties under artificial light replicating standard (AM1.5 spectrum, 1000 W m^{-2}) illumination. A current-voltage curve is measured, to determine the PCE of a solar cell. This is done by applying a varying external bias voltage and measuring the corresponding light-generated current of the solar cell.

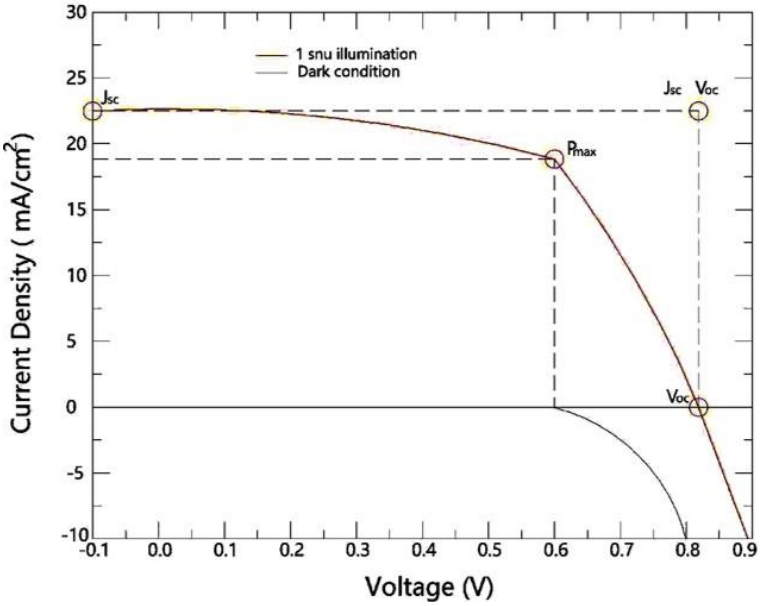

Figure 3.3. An example of J-V curves of a solar cell under 1 sun illumination (red) and in the dark (black).

V_{OC} is the open circuit voltage which is the voltage of the cell that has to be applied to neutralize the internal electric field in a solar cell (i.e., a net current of zero). It depends on the Fermi-levels of the absorber, the hole-and the electron selective layers. The V_{OC} also depends on recombination processes and therefore on the lifetime of the charge-carriers. The short-circuit current (J_{SC}) is the current flow in the solar cell at zero external bias. The J_{SC} gives insight in the absorption behavior of the material since it is strongly dependent on the band gap of the material. Also, the J_{SC} depends on the light intensity of the incident light and the collection of light generated carries[11].

The maximum power a cell can produce upon light irradiation (P_{max}) is defined by the product between V_{max} and J_{max}, defined by the point in the J/V curve that forms the largest rectangular area between the curve and the coordinate axes (Figure 3.3). To determine the quality of a cell with respect to its maximum possible efficiency (set by Jsc and Voc), the fill factor (FF) was introduced. It is defined as:

$$FF = \frac{J_{\max} * v_{max}}{J_{SC} * v_{OC}} = \frac{P_{max}}{J_{SC} V_{OC}} \qquad \text{Equation 5}$$

The fill factor is a key parameter for the device performance and is strongly reduced by internal losses like shunt and series resistance, Using the fill factor, the PCE of solar cell is given by following equation:

$$\eta = {P_{max}}/{P_{in}} = {FF * J_{sc} * V_{oc}}/{P_{in}} \qquad \text{Equation 6}$$

3.1.8 Mobility Measurements

The hole mobility was evaluated according to the literature. A hole only device with the ITO/PEDOT: PSS/HTM/Au structure was fabricated. Indium tin oxide (ITO) coated glass substrates (Kintec, 15-20 Ohm/m^2) were etched and washed with soap, deionized water and ethanol and dried with nitrogen. The remaining organic residues were removed with a digital UV Ozone cleaner (Nova scan) for 15 min. Then, a PEDOT: PSS layer 10 nm thick was deposited by spin coater at 6000 rpm on the substrate for 60 s, followed by annealing at 120°C for 10 min. A TPABT solution was prepared at a concentration of 10 mg/ml in chlorobenzene, and chloroform (2:1) was applied by spin coater over the annealed PEDOT: PSS layer, followed by deposition of a 50 nm thick gold film as a counter electrode. The characteristics of the J-V devices were recorded using the Keithley system. Mobility was calculated by the SCLC method using the Mott-Gurney equation.

3.1.9 Conductivity Measurements

Glass substrates with a thin compact layer of Al_2O_3 were used to improve the wetting of the HTM on the substrate. TPABT was applied by centrifugation at 1250 rpm from solutions of a mixture of chlorobenzene and chloroform containing some LiTFSI as an oxidizing agent, resulting in film thickness ≈50 nm. The films were allowed to oxidize for 24 hours in a desiccator. Gold electrodes 50 nm thick were thermally deposited in vacuum (≈10^{-6} bar). The electrode scheme was designed for two-point probe measurements with channel lengths of 250, 500, and 1000 µm and channel widths of 0.2, 0.1, and 0.056 µm. JV curves were recorded under ambient conditions without illumination using a Keithley 2400 source meter at a scan rate of 1.5 V s^{-1}.

3.1.10 Density Functional Theory- Made by Miriam Fsadni.

<u>HOMO energy correction:</u>

Based on a previously reported method, theoretical HOMO levels of literature HTMs in dichloromethane were compared with their corresponding experimentally determined energies. For a group of 15 HTMs the DFT (PBE0/def2-SV(P) HOMO energies calculated in dichloromethane were plotted against their experimental values and an excellent linear correlation was found (R^2 = 0.9548), with the relationship described by:

$$y = 0.9621x - 0.3959 \qquad \text{Equation 7}$$

The molecules in this group consist of symmetrical HTMs with TPA (Docampo group amide, hydrazine linker- and azomenthine linker-based HTMs) and DPA side units, as well as spiro-OMeTAD. The root mean squared error (RMSE) between the theoretical and experimental data was found to be 0.206 eV. Owing to the excellent linear correlation, applying a correction factor of -0.206 eV to the theoretical HOMO energies provided values in close agreement with experimental results, with a RMSE of 0.019 eV. When the initial group of HTMs was expanded to 23, the correction factor of -0.206 eV was found to give a modest improvement in the theoretical HOMO energies, with a RMSE of 0.105 eV.

3.2 Device Assembly

3.2.1 Cleaning the FTO Substrate

Fluorine-doped tin oxide (FTO) coated glass substrates were etched using zinc powder and 2M HCl solution in de-ionized (DI) water. The patterned substrates were sequentially cleaned with Hellmanex soap solution, DI water, acetone, and ethanol with ultra-sonication for each 30 minutes, followed by drying with nitrogen gun. Finally, the organic residues on substrates were removed with 15 min UV-Ozone treatment.

3.2.2 c – TiO_2 layer Deposition

An acidic solution for compact TiO_2 (c-TiO_2) layer was prepared by mixing 370µl titanium isopropoxide (99.999%, Sigma-Aldrich) and 35 µl of 2M HCl in dry isopropanol (99.8%, Fisher Scientific). Then the mixed solution was spin-coated on cleaned FTO substrates at 2000 rpm for 45 s. The coated substrate was step annealed on hotplate starting from 150°C to finally at 500 °C for 45 min to form electron selective $c - TiO_2$.

3.2.3 Fabrication of Perovskite Film

The perovskite precursor was prepared by mixing 300 mg methylammonium iodide (MAI, Greatcell Solar) and 867 mg lead iodide ($PbI_2, TCI\ Chemicals$) in 1.5 mL mixed solvent which

contained 4:1 volume ratio of dimethylformamide (DMF, 99.8%, Fisher Scientific) and Methyl sulfoxide (DMSO, 99.7%, Fisher Scientific). The solution was kept on magnetic stirrer at 40°C to get a homogeneous light-yellow colour precursor solution. All the steps were performed inside a nitrogen filled glovebox.

The perovskite layer was spin-coated on the top of an electron selective c-TiO_2 layer at 1000 rpm for 30 s, followed by step annealing the coated substrates at 40°C for 45 min then heated at 100°C for 10 min.

Perovskite photovoltaics were fabricated in a standard device structure FTO/SnO_2-nanoparticles (np)/FAMACs perovskite/HTM/Au. FTO glass substrates were patterned with a laser etch and cleaned using a cleaning solution of Hellmanex (2%) in deionized water, acetone, and ethanol, then dried with Nitrogen. The substrates were then treated with UV ozone for 15 minutes. For the electron transport layer (ETL), SnO_2-np (Alfa) diluted with deionized water (1:1) was spin-coated onto FTO substrates at 2000 rpm for 30 s in the air and annealed at 150°C for 30 minutes. The substrates were immediately transferred to deposit a perovskite and (HTL) in the glove box. The perovskite solution was prepared according to the following procedure: PbI_2 (1.575M), $PbCl_2$ (0.05M), CsI (0.075M), FAI (1.21M) and MAI (0.21M) were dissolved in DMF/DMSO mixture (4:1) and left on a hotplate overnight at 70°C in the glovebox. The next day, the solution was filtered before being used. The solution was spin-coated over SnO_2 at 1000 rpm for 10s and 4000 rpm for 30 seconds to deposit the perovskite film. 300 µl of ethyl acetate was dropped onto the spinning substrate at the 15 s, and the substrate was immediately transferred to a hot plate at 100° C for 30 minutes.

3.2.4 Deposition of Hole Transporting Layer (HTL)

Hole Transport layer and electrode deposition: (Spiro-OMeTAD) was prepared by dissolving 75 mg spiro-OMeTAD (Sigma-Aldrich) with 10 mg (Li-TFSI) salt, 13.5 mg (CoTFSI) in 1 mL anhydrous chlorobenzene and 29 µL(tBP). 50 µL of the Spiro-OMeTAD solution filtering was statically dispensed onto the substrate and then spin-coated at 4000 rpm for 38 s, then annealed to the film at 70°C for 30 min.

A solution of TPABT was prepared from 10 mg TPABT in 666.6 µl anhydrous chlorobenzene and 333.3 µL chloroform along with 10 µl tBP and 25 µl LiTFSI salt in acetonitrile (170 mg/ml) in

turn to increase HTM conductivity. The TPABT solution was heated for 10 min until the solution became completely transparent (≈80°C), and then it was passed hot through a 0.45 µm polytetrafluoroethylene (PTFE) syringe filter. 60 µl of the TPABT solution was rapidly dispensed to the substrates while spinning at 1250 rpm for 40 s and 2000 rpm for 5 s.

NiO Deposition

The HTL solution was made by dissolving $NiCl_2$ (1g) and F108 (1 g) in mixture of ethanol (6 ml) and DI water (5 ml) and finally stirring it overnight then leave this solution for a couple of weeks and then centrifuge to remove any solid material. The HTL was deposited on the top of FTO glass by spin-coating at 1500 rpm for 30 s inside the fume hood. Then the film was annealed in furnace at 450℃ for 30 min.

3.2.5 Metal Electrode Deposition

Thermal evaporation was used to deposit the metal contact on the top of HTL to measure the photovoltaic performance of the fabricated device. In this case it was used to deposit 50 nm gold film, 120 nm film of silver or 120 nm film of aluminum through a shadow mask in a vacuum of 10^{-5} Pa.

3.3 References

[1] T. Mirkovic, E.E. Ostroumov, J.M. Anna, R. van Grondelle, Govindjee, G.D. Scholes, Light Absorption and Energy Transfer in the Antenna Complexes of Photosynthetic Organisms, Chemical Reviews 117(2) (2017) 249-293. https://doi.org/10.1021/acs.chemrev.6b00002.

[2] G. Huang, J. He, X. Zhang, M. Feng, Y. Tan, C. Lv, H. Huang, Z. Jin, Applications of Lambert-Beer law in the preparation and performance evaluation of graphene modified asphalt, Construction and Building Materials 273 (2021) 121582. https://doi.org/https://doi.org/10.1016/j.conbuildmat.2020.121582.

[3] F. Guan, M. Asai, D.A. Bartkoski, M. Kleckner, Z.e. Harel, M. Salehpour, Adding the X-ray Bragg reflection physical process in crystal to the Geant4 Monte Carlo simulation toolkit, part I: reflection from a crystal slab, Precision Radiation Oncology 7(1) (2023) 59-66. https://doi.org/https://doi.org/10.1002/pro6.1188.

[4] D.G. Lamas, M. de Oliveira Neto, G. Kellermann, A.F. Craievich, 5 - X-Ray Diffraction and Scattering by Nanomaterials, in: A.L. Da Róz, M. Ferreira, F. de Lima Leite, O.N. Oliveira (Eds.), Nanocharacterization Techniques, William Andrew Publishing2017, pp. 111-182. https://doi.org/https://doi.org/10.1016/B978-0-323-49778-7.00005-9.

[5] R. Sharma, D. Bisen, U. Shukla, B. Sharma, X-ray diffraction: a powerful method of characterizing nanomaterials, Recent Res Sci Technol 4(8) (2012) 77-79.

[6] C. Müller, On the Glass Transition of Polymer Semiconductors and Its Impact on Polymer Solar Cell Stability, Chemistry of Materials 27(8) (2015) 2740-2754. https://doi.org/10.1021/acs.chemmater.5b00024.

[7] T. Grygar, F. Marken, U. Schröder, F. Scholz, Electrochemical analysis of solids. A review, Collection of Czechoslovak chemical communications 67(2) (2002) 163-208.

[8] A.M. Petrina, G.M. Mainasheva, Information measuring systems in nanotechnology, Automatic Documentation and Mathematical Linguistics 44(4) (2010) 187-198. https://doi.org/10.3103/S0005105510040023.

[9] M. Joshi, A. Bhattacharyya, Characterization techniques for nanotechnology applications in textiles, Indian Journal of Fibre and Textile Research 33 (2008) 304-317.

[10] K. Akhtar, S.A. Khan, S.B. Khan, A.M. Asiri, Scanning electron microscopy: Principle and applications in nanomaterials characterization, Handbook of materials characterization (2018) 113-145.

[11] B. Qi, J. Wang, Open-circuit voltage in organic solar cells, Journal of Materials Chemistry 22(46) (2012) 24315-24325. https://doi.org/10.1039/C2JM33719C.

Chapter 4. Improving the Conductivity of Amide-based Small Molecules Through Enhanced Molecular Packing and Their Application as Hole Transport Mediators in Perovskite Solar Cells

Abstract

Organic-inorganic hybrid halide perovskite solar cells (PSCs) have attracted substantial attention from the photovoltaic research community, with power conversion efficiency (PCE) already exceeding 26%. Current state-of-the-art devices rely on Spiro-OMeTAD as the hole transporting material (HTM); however, Spiro-OMeTAD is costly due to its complicated synthesis and expensive product purification, whilst its low conductivity ultimately limits the achievable device efficiency. In this work, we build upon our recently introduced family of low-cost amide-based small molecules and introduce a molecule (termed TPABT) that results in high conductivity values (~10^{-4} S cm^{-1} upon addition of standard ionic additives), outperforming Spiro-OMeTAD, while only costing an estimated $5/g. We ascribe the increased optoelectronic properties to favourable molecular packing, as shown by single crystal X-ray diffraction, which results in close spacing between the triphenylamine blocks. This, in turn, results in a short hole-hopping distance between molecules and, therefore, good mobility and conductivity. In addition, TPABT exhibits a higher bandgap and is as a result more transparent in the visible range of the solar spectrum than Spiro-OMeTAD, leading to lower parasitic absorption losses. We apply the material in perovskite solar cells and obtain good efficiency values in the ~15% range. Our approach shows that engineering better molecular packing may be the key to developing high-efficiency, low-cost HTMs for perovskite solar cells.

4.1 Introduction

Perovskite solar cells (PSCs) are classified under the third generation of photovoltaics,[1] and are considered a promising emerging technology due to their excellent properties: high charge carrier mobility, intense light absorption ability, defect-tolerance and compatibility with low-cost fabrication solution processes[2]. In the past decade, constant efforts have been made to improve the device engineering for perovskite solar cells, leading to a remarkable increase in the power conversion efficiency (PCE) from 3.81% in 2009[3] to over 26%[4]. PSCs typically contain two electrodes, a layer of hole transporting material (HTM), a layer of electron transporting material (ETM), and a perovskite-based light-absorbing layer.[5, 6] When the PSC devices are illuminated,

the photogenerated electrons and holes in the perovskite are transferred to the ETM and HTM and then collected by the front and back electrodes[7].

The HTM has played a key part in the development of PSCs and its performance can determine the efficiency and stability. In “regular” structured PSCs, the HTM is placed on top of the perovskite layer, and it performs variety of roles which include: (i) proficient extraction of the photogenerated holes, including facilitating electron transport to the counter-electrode and hindering electron transfer back to the anode; (ii) promoting device stability by inhibiting direct contact between the perovskite and electrode (typically gold, silver and aluminium) and safeguarding against the dispersal of the electrode into the perovskite layer; (iii) ensuring uniform coverage of the perovskite layer to minimise the charge recombination losses at the perovskite and electrode interface[5]. To maximise the PSC performance, the properties of the HTM must satisfy certain fundamental requirements, which include a small offset in energy between highest occupied molecular orbital (HOMO) of the HTM and the perovskite valence band (VB), an adequate hole mobility and both thermal and photochemical stability.

Many HTMs have been analysed and integrated into PSCs, including organic and inorganic materials. The most common organic examples are 2,2',7,7'-tetrakis[N,N-di(4-methoxyphenyl)amino]-9,9'-spirobifluorene (SpiroOMeTAD), polytriarylamine (PTAA), poly(3,4-ethylenedioxythiophene) polystyrene sulfonate (PEDOT-PSS) and poly(3-hexylthiophene-2,5-diyl) P3HT[8]. Multi-step synthetic methods, involving metal-catalysed cross-coupling reactions and stringent reaction conditions, are required to synthesise these materials, followed by lengthy purification[9]. This makes HTMs like spiro-OMeTAD complicated and expensive to manufacture on a large scale, with anticipated costs in the range of ~90 $/g[10]. This represents a significant contribution to the total cost of the device and consequently may hinder the commercial success of perovskite solar cells.

It has recently introduced condensation chemistry as a low-cost approach, i.e., in the range of 1-10 $/g, to high quality organic molecules with a lower environmental impact[11-14]. This includes aromatic amides, which have additional advantages over conventional C-C coupling because of the dipole nature of the bond arising from the difference of the electronegativity of the nitrogen and oxygen atom. Consequently, stronger interactions within and between the molecules could be promoted through the ability of amide groups to form intramolecular and intermolecular hydrogen bonds[15]. Amide groups are also planar in geometry and have a high rotational barrier due to their

partial double bond character[16]. These properties can lead to a denser molecular packing in the HTM layer. There may also be opportunities to take advantage of the possibility to form monodentate complexes between the oxygen atoms of the amide group with metal atoms, for example building lead or lithium adducts when applied in PSCs[17]. These chemical and structural properties of amide-molecules make these compounds highly promising for applications in solar devices.

In the present work, we describe a new HTM (TPABT), based on familiar building blocks linked together by functional amides, and its application in PSCs. For a non-conjugated material, this HTM demonstrates the exceptional properties of high conductivity and charge carrier mobility, and a blue-shifted onset of absorption, that avoids competition for light with the perovskite layer. These observations show that conjugation through the main chain is not important for materials with good charge transfer properties. Amide bonds in TPABT have the potential to coordinate with Li^+ ions, which leads to an increase in the conductivity beyond 10^{-4} S cm^{-1} upon addition of standard ionic additives, outperforming both our previous amide-based molecule, EDOT-Amide-TPA, and Spiro-OMeTAD in a like-to-like comparison. We used TPABT to fabricate PSCs and obtained devices with PCE ~15%. Our HTM TPABT is superior to Spiro-OMeTAD in terms of optical transparency and low cost, making this a key milestone in developing future low-cost HTMs.

4.2 Results and discussion

4.2.1 Synthesis

TPABT was synthesized by condensing thiophene β-dicarbonyl chloride and 4-amino-4',4''-dimethoxytripehenylamine, as illustrated in Figure 4.1. The structure of the product was confirmed by ^1H and ^{13}C-NMR spectroscopies (Appendix A.1, and A.2). Whilst the singlet at 10.33 ppm confirms the formation of an amide bond, the integral of 12 indicates the methoxy group (3.80 ppm) is in line with two triphenylamine units attached to the thiophene moiety. The successful synthesis was further corroborated by high-resolution mass spectrometry analysis showing the $[M+H]^+$ cation (Appendix A.3).

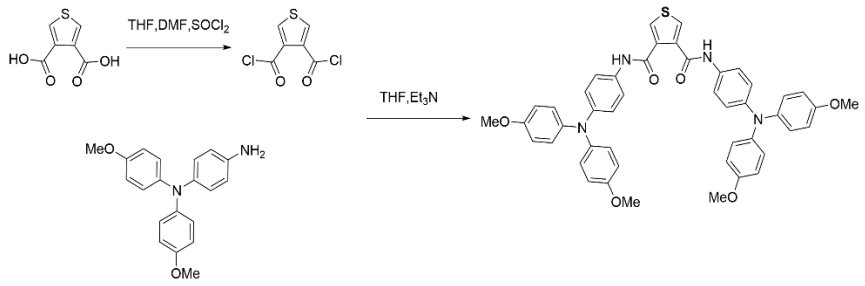

Figure 4.1. Reaction scheme and molecular structure of TPABT. ***Made by Dumitru Sirbu, Miriam Fsadni, and Benjamin Vella.***

TPABT crystals of suitable quality for single-crystal X-ray diffraction measurements were grown by slow evaporation of the solvent (chloroform, chlorobenzene) or slow diffusion of an antisolvent into the TPABT solution (diethyl ether and tetrahydrofuran; hexane and chloroform). In all cases, the TPABT crystallized as a solvate; two polymorphs of the chloroform mono-solvate (TPABT-$CHCl_3$, and TPABT2-$CHCl_3$) (Table Appendix A.2 and A.3), one chlorobenzene solvates (TPABT-CB) (Table Appendix A.1), and one in which there is a 3:1 ratio of diethyl ether and tetrahydrofuran (TPABT-THF) (Table Appendix A.4). It should be noted that crystallisation from the CB/$CHCl_3$ mixture yields the chlorobenzene solvate of TPABT identical to the structure obtained by evaporating the neat chlorobenzene solution. In the case of TPABT-$CHCl_3$, continuous solvent accessible channels are formed along the crystallographic [001] direction (Figure 4.2). In the structure of TPABT-THF the solvent molecules occupy the space between layers of TPABT molecules in the crystallographic (001) plane, while the solvent molecules in both TPABT2-$CHCl_3$ and TPABT-CB occupy discreet pockets formed in the space between the TPA groups of the main residue. Thus, using chlorobenzene and chloroform as the mixture solvent; during the spin coating process; is the application of the TPABT molecule to be used as HTM in perovskite solar devices. Chlorobenzene has been used as an antisolvent for preparing perovskite films in perovskite solar cells. This indicates the limiting choice of solvents tested to dissolve the TPABT. The perovskite must not be soluble in the solvent since the HTM layer is on top of the perovskite layer in the standard configuration in perovskite solar devices.

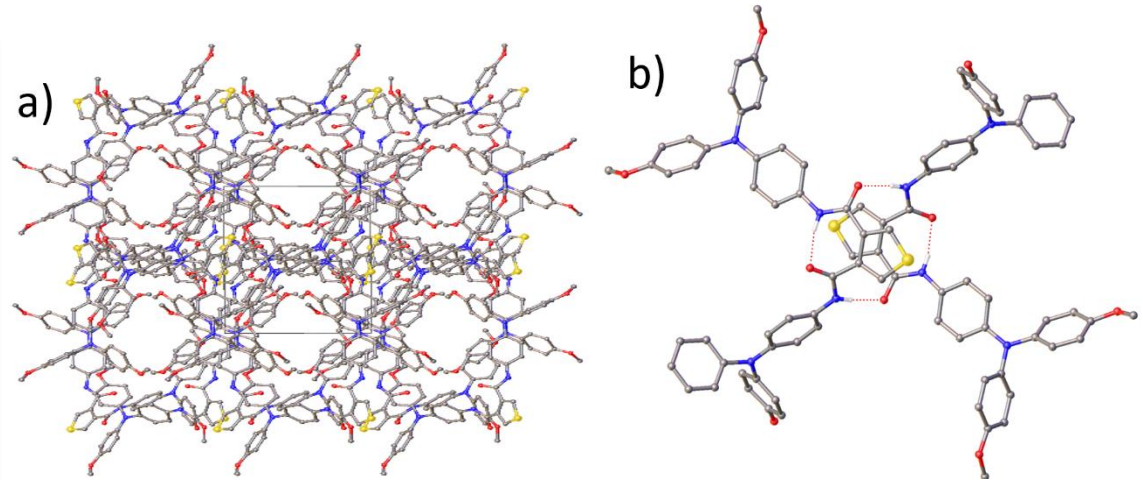

Figure 4.2. a) A view of the structure of TPABT-$CHCl_3$ down the [001] direction highlighting the solvent-accessible channels. Hydrogen atoms and solvent molecules have been omitted for clarity. b) A typical hydrogen-bonded dimer of TPABT molecules as observed in each TPABT structure. ***Made by Paul Waddell.***

In each structure, the conformation of the TPABT molecule is constrained by an intramolecular hydrogen bond formed between the two amide groups. This appears to have the effect of reducing the distance between the two TPA units, as the average N2···N4 distance is *ca.* 12.1 Å compared to 18 Å calculated for the EDOT-amide-TPA. The shortest N2···N4 distance is observed in TPABT2-$CHCl_3$ (*ca.* 10.9 Å). In addition, all four crystal structures form a hydrogen-bonded dimer of TPABT molecules, effectively reducing the distance between the TPA groups of neighbouring molecules to *ca.* 12.1 Å (Figure 4.2).

4.2.2 Computations

To gain further insight into the structural and electronic properties of the amines, DFT calculations of the molecules in dichloromethane were performed at the PBE0/def2-SV(P) level using ORCA (version 5.0.2)[18-23]. Frequency calculations were performed on all energy minimised geometries to ensure that minimum energy conformations were obtained. This show (Figure 4.3) that the HOMO of TPABT is localised on the TPA arm and the amide linker moiety. In contrast to the HOMO of TPABT appears to be localised on just one of the triphenylamine (TPA) units. The orientation and distance of the carbonyl oxygen to the amide hydrogen on either side of the thiophene core point to the possibility of intramolecular hydrogen bonding (in agreement with the

experimental crystal structure), resulting in asymmetry. This manifests in the destabilisation and stabilisation of the HOMO-1 and LUMO+1 energies, respectively. The hole hopping distance may be approximated by the TPA N...N distances of HOMO sites on two neighbouring molecules. The TPABT-CB crystal structure reveals the shortest hopping distance to be 8.9 Å. The equivalent distances in TPABT2-$CHCl_3$ and TPABT-THF are even shorter at 8.6 Å and 8.0 Å, respectively.

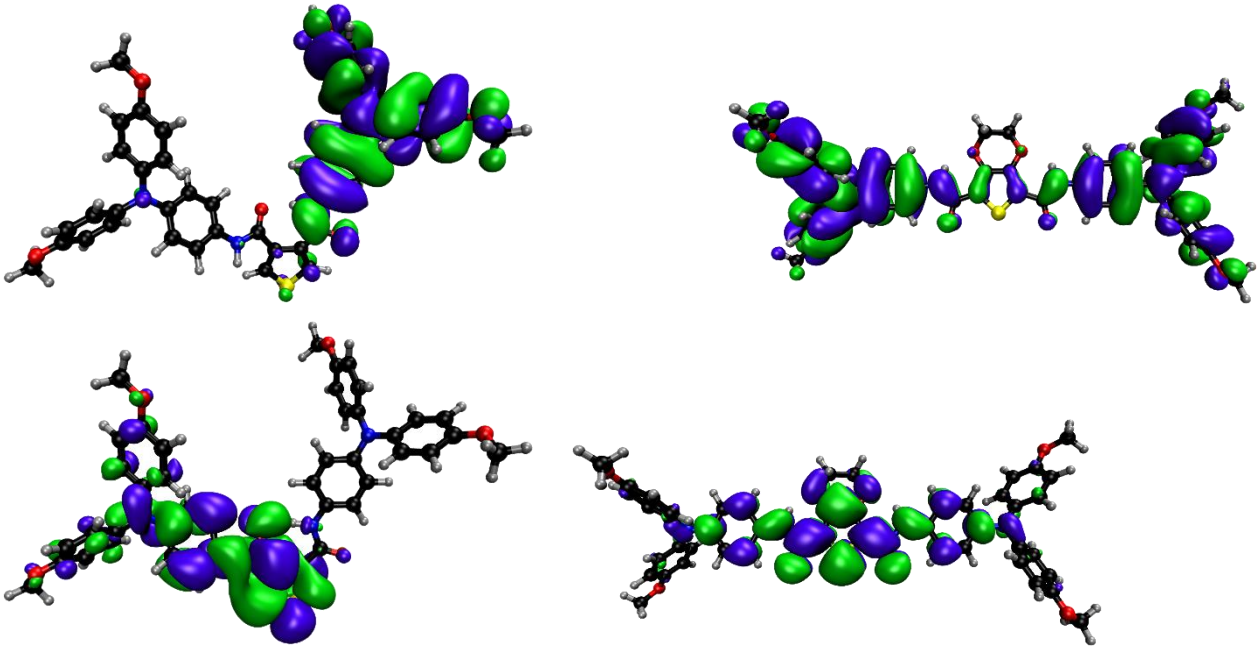

Figure 4.3. Frontier orbital distributions of TPABT (top left: HOMO; bottom left LUMO) and EDOT-Amide-TPA (top right: HOMO; bottom right: LUMO) in dichloromethane, from DFT (PBE0/def2-SV(P)). ***Made by Miriam Fsadni.***

The HOMO energies obtained for single molecules in vacuum are likely to vary from those in the film. Some of the effects of neighbouring molecules can be approximated by implementing the C-PCM, with the parameters set to dichloromethane ($\kappa = 9.08$)[24]. It has previously been shown that a correction factor can be applied to theoretical HOMO energies calculated in dichloromethane, giving results that match closely with those from cyclic voltammetry experiments[25, 26]. Using a procedure reported by Chi, *et al.* [23], we obtained a correction of –0.206 eV for the HOMO energies of a range of TPA- and DPA-based molecules in dichloromethane (Table 4.1).

Table 4.1. Calculated molecular energy levels for the HTMs using DFT.

	Frontier Orbital Energies (eV)					
Compound	$HOMO_{DFT,vac}$*	$HOMO_{DFT,DCM}$†	$HOMO_{calc}$‡	$LUMO_{DFT,vacuum}$*	$LUMO_{DFT,DCM}$†	$Dipole_{DFT,DCM}$† (Debye)
TPA-BT	-4.87	-5.03	-5.23	-1.16	-1.34	10.6
EDOT-Amide-TPA[12, 14, 17, 24]	-4.87	-5.09	-5.29	-1.82	-2.01	13.0
Spiro-OMeTAD[12, 14, 17, 24]	-4.60	-4.91	-5.12	-0.75	-1.09	3.26

* PBE0/def2-SV(P); † PBE0/def2-SV(P) with C-PCM(CH_2Cl_2) implemented; ‡based on $HOMO_{DFT,DCM}$ with correction factor (-0.206 eV) applied

The calculated HOMO energy of TPABT (-5.23 eV) was found to be close to the experimentally determined value (-5.27 eV) and, like EDOT-Amide-TPA, is suitably higher than the perovskite valence band (-5.43 eV). Interestingly, TPABT displays a high dipole moment, although lower than that of EDOT-Amide-TPA. While the high dipole of EDOT-Amide-TPA was previously offered as a possible explanation for its high mobility, by promoting close molecular packing in the solid film, recent work in our group has shown this to be unlikely[27]. Indeed, a higher dipole generally correlates with a lower mobility[28, 29], as the dipole-dipole interactions give rise to large energy barriers that restrict the mobility of the charge particles to smaller and smaller regions of the film, therefore, EDOT-Amide-TPA performs well despite this. Consequently, the higher mobility of TPABT compared to EDOT-Amide-TPA may be partly attributable to its lower dipole moment.

4.2.3 Optical and electrochemical characterization

To maximise light harvesting by the perovskite layer, minimise parasitic absorption losses, and enhance the current in solar cells, light absorption by the HTM in the range of visible light absorption from 400 to 800 nm should be minimised. Thus, the optical properties of TPABT, EDOT-Amide-TPA, and Spiro-OMeTAD films were investigated using UV-visible absorption spectroscopy. The maximum absorption wavelengths of the HTMs are listed in Table 4.2. The

absorption spectra of all three HTM thin films, are displayed in Figure 4.4 a) and Appendix A.4). The pristine Spiro-OMeTAD exhibits strong absorption I n the UV region, with a peak maximum at 374 nm, which is consistent with data published previously by Wang, *et al.* [30]. In contrast, the absorbance of pristine EDOT-Amide-TPA and TPABT films were very low in the UV region. We found this new material, TPABT, to be more transparent in the visible region, compared to both Spiro-OMeTAD and EDOT-Amide-TPA (Appendix A.5), which will allow more photons to be absorbed by the perovskite layer and improve the PCE.

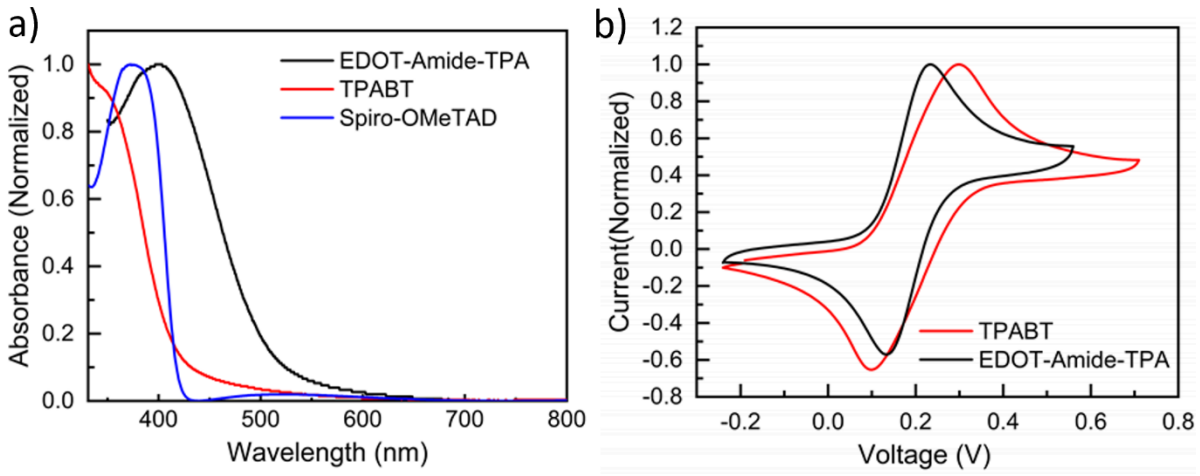

Figure 4.4 a) Normalized UV-visible absorption spectra of TPABT (50 nm thickness), EDOT-Amide-TPA (45 nm) and Spiro-OMeTAD (200 nm) as a thin film that was applied by spin coating under the same conditions as the solar cells (below), b) Normalised cyclic voltammogram of TPABT and EDOT-Amide-TPA measured in anhydrous dichloromethane under N_2 with 0.1 M $TBAPF_6$.

Table 4.2. The absorption maxima of TPABT, EDOT-Amide-TPA and Spiro-OMeTAD as pristine films and doped with added LiTFSI and the redox potentials of the HTMs in dichloromethane.

HTM	λ_{max} pristine (nm)	λ_{max} doped (nm)	E_g[a] (eV)	$E_{1/2}[HTM^+\|HTM]$ (V vs Fc)	E_{HOMO}[b] (eV)	E_{LUMO}[c] (eV)
Spiro-OMeTAD	374	376	2.70[31, 32]	0.13	-5.20	-2.50
EDOT-Amide-TPA	408	430	2.73[12]	0.18	-5.25	-2.52
TPABT	333	332	2.70	0.22	-5.29	-2.594

[a] E_g is the HOMO and LUMO separation derived from the optical spectra (Appendix A.7). [b] calculated from $E_{1/2}[HTM^+|HTM]$ + 4.85 eV, [c] estimated from $E_{HOMO} + E_g$.

On addition of LiTFSI to TPABT, we observed a shift in the absorption maximum, indicating a change in the electronic properties of the film (Appendix A.6). This is consistent with previous research by Petrus, *et al.* [12]. We also observed that the absorption maxima of Spiro-OMeTAD and EDOT-Amide-TPA decreased upon addition of LiTFSI, compared to their pristine absorption. Petrus *et al*. previously demonstrated by FTIR spectroscopy that LiTFSI plays a role in doping the HTMs through the coordination of the Li^+ ion to the amide bond, and this coordination leads to increased conjugation through the amide bond Petrus, *et al.* [12]. This leads to an increase in carrier density, charge delocalisation and conductivity of the film[33].

It is essential to have a good alignment of the HOMO energy level of the HTM with the valence band of the chosen perovskite to successfully extract holes and to obtain a high open circuit voltage (V_{OC}). Hence, the electrochemical behaviour of TPABT was investigated by cyclic voltammetry (CV) and the data is shown in(Figure 4.4 b ,Table 4.2,and Appendix A.8). We observed reversible oxidation starting at 0.17 V versus F_C and the redox potential of TPABT was determined to be 0.22

V vs. Fc, which is more positive than that for EDOT-amide-TPA (0.18 V vs. Fc). From these values plus the optical energy gap (E_g), the HOMO energy was calculated to be -5.27 eV and the LUMO energy was estimated to be -2.5 eV. The energy level of the HOMO is in good agreement with the valence band of the perovskite (-5.23 eV)[30] and is expected to result in minimal losses in V_{OC}, while the high LUMO energy allows TPABT to function as an effective electron blocking layer.

4.2.4 Thermal Properties

One important advantage of aromatic amides is their outstanding thermal and chemical stability[34]. This is important when it comes to photovoltaic devices as the HTM should not degrade under full operational conditions, which can reach over 80°C[12]. The thermal properties of TPABT were investigated by using thermogravimetric analysis (TGA) and differential scanning calorimetry (DSC) measurements compared with EDOT-Amide-TPA and Spiro-OMeTAD. The results of TGA for HTMs, (Figure 4.5a) show that the TPABT behaves similarly to EDOT-Amide-TPA and Spiro-OMeTAD below 300°C with mass loss of less than 1%. The degradation temperature was 300°C for TPABT and 347 °C for EDOT-Amide-TPA, which is very close to the value published by Petrus et al., while the degradation temperature of Spiro-OMeTAD was 408°C, also consistent with a previous study[12]. However, after doping the TPABT and Spiro-OMeTAD by LiTFSI and *t*BP, the degradation temperature of TPABT shifted from 300°C to 350°C, while the spiro-OMeAD started degrading from 250 °C, that indicates to TPABT is more stable than Spiro-OMeTAD because of the amide bonds (Appendix A.9).

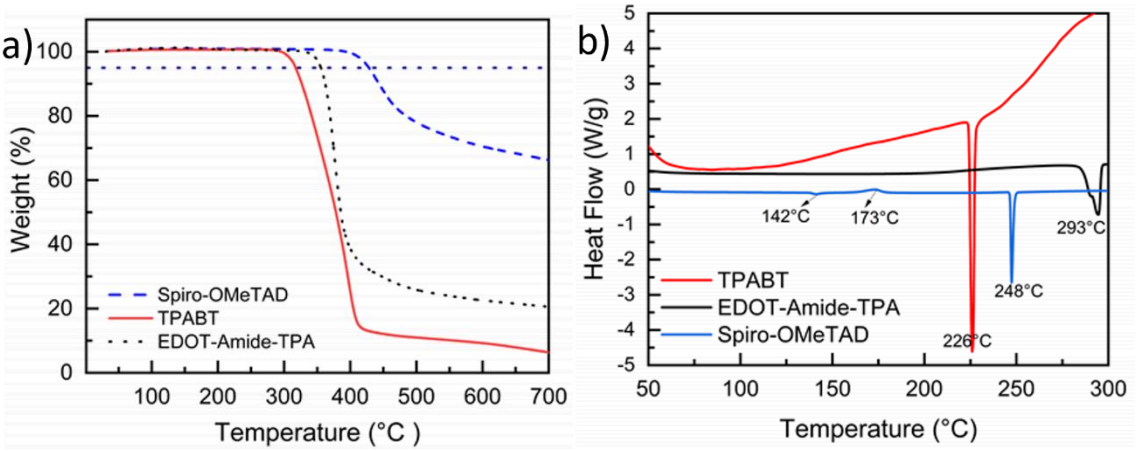

Figure 4.5. a) Thermogravimetric analysis of pristine TPABT, EDOT-Amide-TPA and Spiro-OMeTAD at a heating rate of 5°C min^{-1} under N_2 atmosphere, b) Differential scanning calorimetry (first cycle of heating) for TPABT, EDOT-Amide-TPA and Spiro-OMeTAD at the heating rate of 5°C min^{-1}.

The DSC analysis can expose the polymorph character of HTMs and the melting point also indicates the stability of the materials. In Figure 4.5b, the DSC of Spiro-OMeTAD in the first cycle of heating shows the glass transition T_g at 142°C, a crystallisation temperature T_C of 173°C and the melting point T_m at 248°C. In the second cycle of heating, the T_g had shifted to 124°C, while the T_m and T_C were not observed (Appendix A.12), and those values obtained match well with the values reported in the literature[35]. By comparison, the first cycle of heating TPABT and EDOT-Amide-TPA showed the T_m at 226°C and 293°C, respectively. The T_m appeared at the same temperature in second wave of heating for EDOT-Amide-TPA, however, the TPABT was amorphous in second cycle (Appendix A.10, Appendix A.11). All thermal transitions are well above the operating temperature of photovoltaic devices (Table Appendix A.6).

4.2.5 Charge Transport Measurements

To gain a better understanding of the charge transport, the hole mobilities of the HTMs were measured in devices using the following architecture: ITO/PEDOT:PSS/TPABT/Au; the results are shown in Figure 4.6b , Appendix A.13 ,and summarised in Table Appendix A.7. The estimated hole mobility in TPABT upon addition of Li-TFSI was 3.23×10^{-5} cm^2 $V^{-1}s^{-1}$. The hole mobility in Spiro-OMeTAD and EDOT-Amide-TPA, have been reported to reach of 5.3×10^{-4} cm^2 $V^{-1}s^{-1}$ and 2.1×10^{-4} cm^2 $V^{-1}s^{-1}$, respectively. Upon the addition of LiTFSI to the HTM, a significant increase

in mobility was observed, which can be ascribed to the reduction of the barrier height for charge hopping between TPA units.

In addition to the mobility of charge carriers, high conductivity is essential for HTMs. Thus, we performed in-plane conductivity measurements with LiTFSI as an additive and the results are shown in the Figure 4.6a. With an increase in the concentration of LiTFSI in the HTM solution, the conductivity of the TPABT films sharply increases, reaching a value of 4.71×10^{-4} S cm^{-1} with 225 mol % LiTFSI. Lower conductivity was recorded for Spiro-OMeTAD (1.2×10^{-4} S cm^{-1}) and EDOT-amide-TPA (1.84×10^{-4} S cm^{-1}) with the addition of 225% LiTFSI. The high conductivity value for TBABT might refer to the more porous nature of this material compared with Spiro-OMeTAD and EDOT-amide-TPA, as AFM images are shown in (Appendix A.14 -A.16). This nature could lead to an increase in the oxidation rate, which leads to a rise in conductivity.

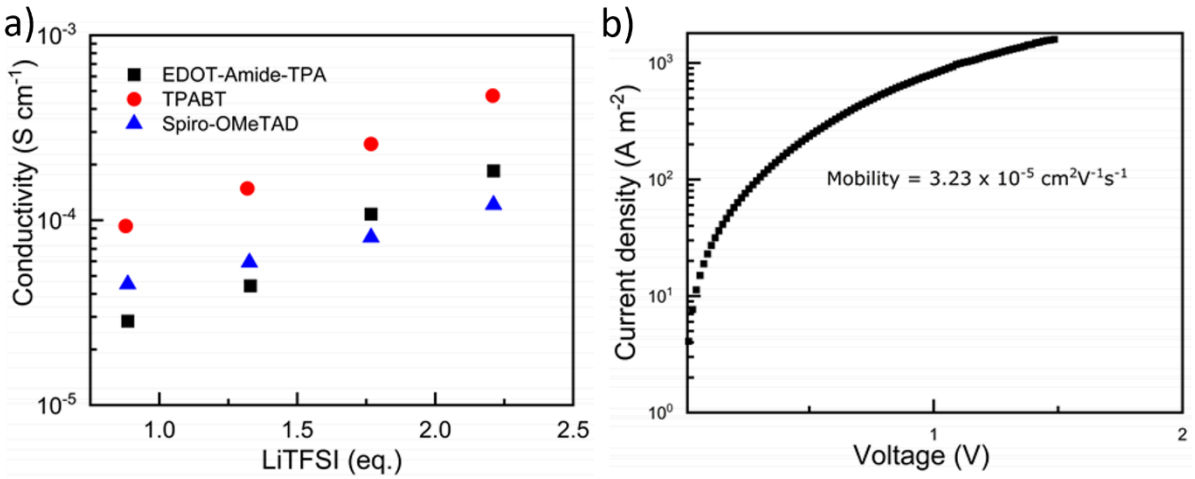

Figure 4.6. a) Conductivity of the film vs. concentration of LiTFSI. 20% error is added to account for the deviation in film thickness across the samples (+/- 10 nm), b) J-V measurements of hole only devices.

4.2.6 Device Characterisation

Solar cell devices were prepared to investigate the appropriateness of TPABT as an HTM in PSCs, and the results were compared with Spiro-OMeTAD. The TPABT deposition parameters were optimised with $MAPbI_3$ (Appendix A.26 -A.27, and Table Appendix A.13-A.14). Then, solar cells were fabricated with a state-of-the-art perovskite composition, as the mixture of halides and cations has been reported to outperform $MAPbI_3$ when applied in solar cells[7]. The planar configuration device was adopted with ($FTO/SnO_2/Cs_{0.05}(FA_{0.85}MA_{0.15})0.95Pb(I_3Cl_2)$/2D perovskite/HTM/Au) as shown in Figure 4.7b. To enhance the conductivity and mobility of the HTM, TPABT was doped with *t*BP and LiTFSI. The solar cells devices were characterised by measuring the current density-voltage curve under standard AM 1.5 sun illumination (100 mW cm^{-2}). The best devices are shown in Figure 4.7a, with 16.9% and 14.84% efficiency for Spiro-OMeTAD and TPABT, respectively. The slightly low efficiency of TPABT might be due to somewhat unfavourable energetics at the interface with the perovskite, which possibly hinders charge extraction rates or interfacial recombination. Moreover, the statistical analysis (Table Appendix A.9-A.12) shows that the increases in power conversion efficiencies (PCE), open-circuit voltage (V_{OC}), and short-circuit current density (J_{SC}) are significant for TPABT after two days of oxidation (Appendix A.22–A.25). We consider that the outstanding stability of TPABT is related to the presence of the amide bonds, as the interactions between Li^+ ions and the amide bonds facilitate a homogeneous distribution of the ions throughout the HTM and minimise their propagation. Moreover, this strong inter-molecular interaction of TPABT helps with film formation, as shown in AFM images in (Appendix A.17, A.18, and A.20) which in turn reduces the number of pinholes in the film. In comparison, Spiro-OMeTAD tends to form nanopores as well as larger pinholes (Appendix A.19 and A.21) which leave some of the perovskite surface exposed and therefore degradation is catalysed at these sites.

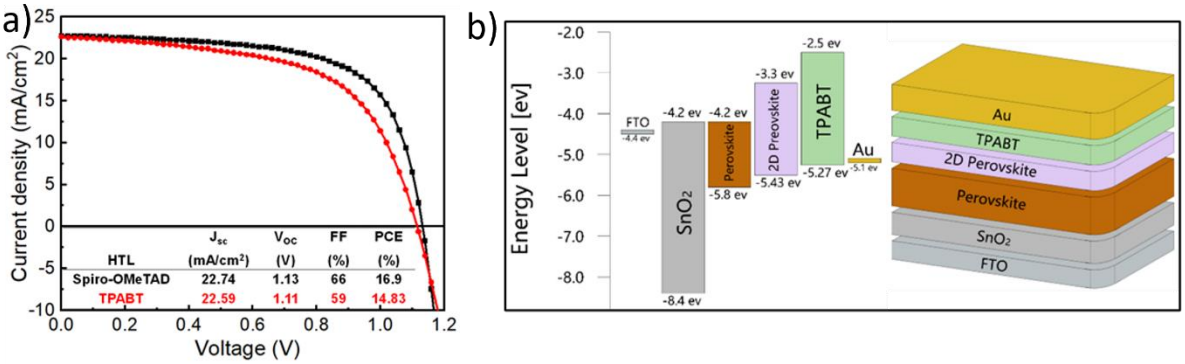

Figure 4.7. a) JV curves collected under AM 1.5 simulated sunlight of the champion device comprising TPABT and Spiro-OMeTAD in combination with FAMACs perovskite on SnO_2, b) energy level diagram of TPABT with Perovskite and ETL.

4.3 Conclusions

In summary, this work showed a way to design and produce new low-cost hole transporting material (TPABT) that can outperform the previous material in the same generation, EDOT-Amide-TPA. The material showed favourable properties including the molecular assembly, high transparency and excellent charge transport. This material was synthesized through simple condensation chemistry, resulting in extremely low-cost materials, especially compared to Spiro-OMeTAD which is produced at very high cost due to the complicated synthesis and extensive purification. The calculated HOMO-of TPABT obtained from cyclic voltammetry and DFT calculations, indicate a good alignment of the HOMO level of TPABT with the valence band of perovskite suggesting hole-selectivity and the potential for good performance in solar cell devices. Conductivity measurements show that the addition of LiTFSI as an oxidant result in a major increase of the conductivity reaching up to 4.71×10^{-4} S cm^{-1} upon addition of 225% mol Li-TFSI, which was 4 × higher than Spiro-OMeTAD under the same conditions. Hole mobility measurements of the TPABT showed an increase up to 10^{-4} cm^2 $V^{-1}s^{-1}$ upon addition of Li-TFSI. Employing the TPABT in solar cell devices, shows good efficiency ~15% with V_{oc} 1.11V and J_{sc} 22.59 mA cm^{-2}. Further investigation of the performance of TPABT derivatives are underway; it is relatively easy to switch out the core and tune the TPA units to improve the film characteristics, conductivity and transparency, which could lead to potential further improvements to efficiency.

4.4 Experimental Section

4.4.1 Synthesis of TPABT

All chemicals were purchased from commercial sources and used as received, unless otherwise stated. Solvents for spectroscopic studies were of the highest purity available. The 4-amino-4',4''-dimethoxytriphenylamine was prepared using a previously reported method[11].

4.4.2 Synthesis of 3,4-Ethylenedioxythiophene-2,5-dicarbonyl chloride

2.8 mmol of thiophene-3,4-dicarboxylic acid was dissolved in 40 mL THF and 0.1 eq. of DMF was added. Then 2.25 eq. of $SOCl_2$ was added dropwise, resulting in a colour change to yellow. After heating the solution for 2h at 80 °C, the solution was allowed to cool down to R.T. The solvents were removed under vacuum, resulting in acyl chloride in a quantitative yield as a yellow-brown solid, which was used in the next step without further purification.

4.4.3 Synthesis of N^3,N^4-bis(4-(bis(4-methoxyphenyl)amino)phenyl)thiophene-3,4-dicarboxamide TPABT

The total yield of the acyl chloride was dissolved in 40 mL dry THF, and 2.25 eq. 4-amino-4',4''-dimethoxytripehenylamine was added, followed by dropwise addition of 0.2 mL triethylamine to the solution. The resulting dark red solution was heated to reflux for 2 h. The mixture was allowed to cool to R.T. overnight, reduced to 5 mL, and 10 mL Et_2O was added, resulting in a pale-yellow precipitate. The precipitate was filtered, washed twice with ethanol, and dried in vacuum to deliver the product as a pale beige solid with a yield of 70%. ^{1}H NMR (400 MHz, DMSO-d_6) δ (ppm) = 10.33 (s, 2H, amide), 7.87 (s, 2H, thiophene), 7.56 (d, J = 8.9 Hz, 4H, phenyl), 7.04 (m, 8H, phenyl), 6.96 (d, J = 8.9 Hz, 4H, phenyl), 6.82 (m, 8H, phenyl), 3.80 (s, 12H, methoxy). ^{13}C NMR (101 MHz, DMSO-d_6) δ (ppm) = 13C NMR (101 MHz, CDCl3) δ 162.63, 155.81, 145.85, 141.27, 135.77, 132.60, 131.38, 126.24, 121.83, 121.59, 114.83, 55.66. FTIR: ν(cm^{-1}): 3238 (vw), 3100 (vw), 3039 (w), 2948 (vw), 2834 (w), 1608 (s), 1557 (m), 1538 (m), 1501 (vs), 1463 (m), 1441 (w), 1429 (w), 1368 (w), 1310 (m), 1284 (m), 1240 (vs), 1188 (w), 1178 (m), 1104 (w), 1035 (s), 943 (vw), 911 (w), 892 (w), 569 (w), 824 (vs), 782 (m), 728 (s), 679 (w), 639 (w), 617 (w), 572 (m), 525 (m), 479 (w). HRMS (*m/z*): found $[M + H]^+$: 777.2737, calcd for $C_{46}H_{40}N_4O_6SH$: 777.2741.

4.4.4 General Characterisation Techniques

Electronic absorption spectra were recorded at RT using a Shimadzu UV-1800 spectrophotometer. FT-IR spectrum was recorded with a PerkinElmer FT-IR Spectrum Two instrument. High-resolution electrospray ionization (ESI) mass spectrometry data was collected by the National Mass Spectrometry Facility (NMSF) in Swansea. ^{1}H, ^{13}C NMR spectra was recorded with a Jeol ECS 400 MHz instrument. Chemical shifts are referenced relative to the residual protonated solvent.

Crystal structure data for TPABT-$CHCl_3$, TPABT-CB and TPABT-THF was collected on an Xcalibur, Atlas, Gemini ultra-diffractometer equipped with a fine-focus sealed X-ray tube ($\lambda_{CuK\alpha}$ = 1.54184 Å). Cell refinement, data collection and data reduction were undertaken via software CrysAlisPro (Rigaku OD, 2015). For TPABT-$CHCl_3$ and TPABT-CB, intensities were corrected for absorption via an analytical numeric absorption correction method using a multifaceted crystal model based on expressions derived by Clark, *et al.* [36]. For TPABT-THF, an empirical absorption correction using spherical harmonics was implemented in SCALE3 ABSPACK scaling algorithm.

Data for TPABT-$CHCl_3$ was collected at beamline I19 at Diamond Light Source ($\lambda_{Synchrotron}$ = 0.6889 Å)[33, 34]. This data was processed using APEX3 (Bruker (2015). APEX3. BrukerAXS Inc., Madison, Wisconsin, USA.).

Using Olex2[37], the structure was solved using XT[35] and refined by XL[38]. All non-hydrogen atoms were refined anisotropically, and hydrogen atoms were positioned with idealised geometry, with the exception of those bound to heteroatoms which were located using peaks in the Fourier difference map. The displacement parameters of the hydrogen atoms were constrained using a riding model with $U_{(H)}$ set to be an appropriate multiple of the U_{eq} value of the parent atom.

4.4.5 Cyclic Voltammetry (CV)

Cyclic voltammetry experiments were performed using glassy carbon as a working electrode, the counter electrode was platinum wire and an Ag/AgCl reference electrode with and without ferrocene (Fc) internal reference. Experiments were performed in anhydrous and degassed dichloromethane solutions of the hole transporter, with 0.1 M tetrabutylammonium hexafluorophosphate (tBuNPF_6) as electrolyte and a scan rate of 50 mV s^{-1}. HOMO levels were calculated as stated by the literature with the formal potential of the Fc+/Fc redox positioned at −5.27 eV versus vacuum.

4.5 References

[1] Y. Rong, Y. Hu, A. Mei, H. Tan, M.I. Saidaminov, S.I. Seok, M.D. McGehee, E.H. Sargent, H. Han, Challenges for commercializing perovskite solar cells, Science 361(6408) (2018). https://doi.org/10.1126/science.aat8235.

[2] X. Yin, Z. Song, Z. Li, W. Tang, Toward ideal hole transport materials: A review on recent progress in dopant-free hole transport materials for fabricating efficient and stable perovskite solar cells, Energy and Environmental Science 13(11) (2020) 4057-4086. https://doi.org/10.1039/d0ee02337j.

[3] A. Kojima, K. Teshima, Y. Shirai, T. Miyasaka, Organometal halide perovskites as visible-light sensitizers for photovoltaic cells, Journal of the American Chemical Society 131(17) (2009) 6050-1. https://doi.org/10.1021/ja809598r.

[4] Best Research-Cell Efficiency Chart.

[5] S. Li, Y.-L. Cao, W.-H. Li, Z.-S. Bo, A brief review of hole transporting materials commonly used in perovskite solar cells, Rare Metals 40(10) (2021) 2712-2729. https://doi.org/10.1007/s12598-020-01691-z.

[6] T.H. Schloemer, J.A. Christians, J.M. Luther, A. Sellinger, Doping strategies for small molecule organic hole-transport materials: impacts on perovskite solar cell performance and stability, Chemical Science 10(7) (2019) 1904-1935. https://doi.org/10.1039/C8SC05284K.

[7] K. Pydzińskapydzińska-Białek, V. Drushliak, E. Coy, K. Załę, J. Flach, J. Idígoras, L. Contreras-Bernal, A. Hagfeldt, J.A. Anta, M.Z.ł. Ziółek, Understanding the Interfaces between Triple-Cation Perovskite and Electron or Hole Transporting Material, ACS Appl. Mater. Interfaces 12 (2020) 36-36. https://doi.org/10.1021/acsami.0c07095.

[8] M.M. Tavakoli, J. Zhao, R. Po, G. Bianchi, A. Cominetti, C. Carbonera, J. Kong, M.M. Tavakoli, J. Zhao, J. Kong, R. Po, G. Bianchi, A. Cominetti, C. Carbonera, Efficient and Stable Mesoscopic Perovskite Solar Cells Using PDTITT as a New Hole Transporting Layer, (2019). https://doi.org/10.1002/adfm.201905887.

[9] U. Díaz, A. Corma, Organic-Inorganic Hybrid Materials: Multi-FunctionalS olids for Multi-StepR eactionP rocesses, & Nanotechnology Chem. Eur.J 24 (2018) 3944-3958. https://doi.org/10.1002/chem.201704185.

[10] L. Nakka, Y. Cheng, A.G. Aberle, F. Lin, Analytical Review of Spiro-OMeTAD Hole Transport Materials: Paths Toward Stable and Efficient Perovskite Solar Cells, (2022). https://doi.org/10.1002/aesr.202200045.

[11] M.L. Petrus, T. Bein, T.J. Dingemans, P. Docampo, A low cost azomethine-based hole transporting material for perovskite photovoltaics, Journal of Materials Chemistry A 3(23) (2015) 12159-12162. https://doi.org/10.1039/C5TA03046C.

[12] M.L. Petrus, K. Schutt, M.T. Sirtl, E.M. Hutter, A.C. Closs, J.M. Ball, J.C. Bijleveld, A. Petrozza, T. Bein, T.J. Dingemans, T.J. Savenije, H. Snaith, P. Docampo, New Generation Hole Transporting Materials for Perovskite Solar Cells: Amide-Based Small-Molecules with Nonconjugated Backbones, Advanced Energy Materials 8(32) (2018) 1801605-1801605. https://doi.org/10.1002/AENM.201801605.

[13] M.L. Petrus, A. Music, A.C. Closs, J.C. Bijleveld, M.T. Sirtl, Y. Hu, T.J. Dingemans, T. Bein, P. Docampo, Design rules for the preparation of low-cost hole transporting materials for perovskite solar cells with moisture barrier properties, Journal of Materials Chemistry A 5(48) (2017) 25200-25210. https://doi.org/10.1039/c7ta06452g.

[14] M.L. Petrus, R.K.M. Bouwer, U. Lafont, S. Athanasopoulos, N.C. Greenham, T.J. Dingemans, Small-molecule azomethines: Organic photovoltaics via Schiff base condensation chemistry, Journal of Materials Chemistry A 2(25) (2014) 9474-9477. https://doi.org/10.1039/c4ta01629g.

[15] D.W. Zhang, X. Zhao, J.L. Hou, Z.T. Li, Aromatic amide foldamers: Structures, properties, and functions, Chemical Reviews 112(10) (2012) 5271-5316. https://doi.org/10.1021/cr300116k.

[16] R.A. Olsen, L. Liu, N. Ghaderi, A. Johns, M.E. Hatcher, L.J. Mueller, The Amide Rotational Barriers in Picolinamide and Nicotinamide: NMR and ab Initio Studies, (2003). https://doi.org/10.1021/ja028751j.

[17] M.L. Petrus, J. Schlipf, C. Li, T.P. Gujar, N. Giesbrecht, P. Müller-Buschbaum, M. Thelakkat, T. Bein, S. Hüttner, P. Docampo, Capturing the Sun: A Review of the Challenges and Perspectives of Perovskite Solar Cells, Advanced Energy Materials 7(16) (2017) 1-27. https://doi.org/10.1002/aenm.201700264.

[18] F. Neese, The ORCA program system, WIREs Computational Molecular Science 2(1) (2012) 73-78. https://doi.org/10.1002/wcms.81.

[19] Y. Guo, C. Riplinger, U. Becker, D.G. Liakos, Y. Minenkov, L. Cavallo, F. Neese, Communication: An improved linear scaling perturbative triples correction for the domain based local pair-natural orbital based singles and doubles coupled cluster method [DLPNO-CCSD(T)], The Journal of Chemical Physics 148(1) (2018) 011101-011101. https://doi.org/10.1063/1.5011798.

[20] F. Neese, Software update: The <scp>ORCA</scp> program system—Version 5.0, WIREs Computational Molecular Science 12(5) (2022). https://doi.org/10.1002/wcms.1606.
[21] F. Weigend, R. Ahlrichs, Balanced basis sets of split valence, triple zeta valence and quadruple zeta valence quality for H to Rn: Design and assessment of accuracy, Physical Chemistry Chemical Physics 7(18) (2005) 3297-3297. https://doi.org/10.1039/b508541a.
[22] S. Tortorella, M.M. Talamo, A. Cardone, M. Pastore, F. De Angelis, Benchmarking DFT and semi-empirical methods for a reliable and cost-efficient computational screening of benzofulvene derivatives as donor materials for small-molecule organic solar cells, Journal of Physics: Condensed Matter 28(7) (2016) 074005-074005. https://doi.org/10.1088/0953-8984/28/7/074005.
[23] W.-J. Chi, Q.-S. Li, Z.-S. Li, Exploring the electrochemical properties of hole transport materials with spiro-cores for efficient perovskite solar cells from first-principles, Nanoscale 8(11) (2016) 6146-6154. https://doi.org/10.1039/C6NR00235H.
[24] M.L. Petrus, M.T. Sirtl, A.C. Closs, T. Bein, P. Docampo, Hydrazone-based hole transporting material prepared via condensation chemistry as alternative for cross-coupling chemistry for perovskite solar cells, Molecular Systems Design and Engineering 3(5) (2018) 734-740. https://doi.org/10.1039/c8me00023a.
[25] T. Pope, Y. Giret, M. Fsadni, P. Docampo, C. Groves, T.J. Penfold, Modelling the effect of dipole ordering on charge-carrier mobility in organic semiconductors, Organic Electronics 115(January) (2023) 106760-106760. https://doi.org/10.1016/j.orgel.2023.106760.
[26] P. Friederich, V. Meded, A. Poschlad, T. Neumann, V. Rodin, V. Stehr, F. Symalla, D. Danilov, G. Lüdemann, R.F. Fink, I. Kondov, F. von Wrochem, W. Wenzel, Molecular Origin of the Charge Carrier Mobility in Small Molecule Organic Semiconductors, Advanced Functional Materials 26(31) (2016) 5757-5763. https://doi.org/10.1002/adfm.201601807.
[27] Y. Tu, J. Wu, G. Xu, X. Yang, R. Cai, Q. Gong, R. Zhu, W. Huang, 2006545 (1 of 22) Perovskite Solar Cells for Space Applications: Progress and Challenges, (2021). https://doi.org/10.1002/adma.202006545.
[28] J.F. Ponder, S.A. Gregory, A. Atassi, A.K. Menon, A.W. Lang, L.R. Savagian, J.R. Reynolds, S.K. Yee, Significant Enhancement of the Electrical Conductivity of Conjugated Polymers by Post-Processing Side Chain Removal, Cite This: J. Am. Chem. Soc 2022 (2022). https://doi.org/10.1021/jacs.1c11558.

[29] J.A. Röhr, D. Moia, S.A. Haque, T. Kirchartz, J. Nelson, Exploring the validity and limitations of the Mott-Gurney law for charge-carrier mobility determination of semiconducting thin-films, Journal of Physics Condensed Matter 30(10) (2018). https://doi.org/10.1088/1361-648X/aaabad.

[30] S. Wang, W. Sun, M. Zhang, H. Yan, G. Hua, Z. Li, R. He, W. Zeng, Z. Lan, J. Wu, Strong electron acceptor additive based spiro-OMeTAD for high-performance and hysteresis-less planar perovskite solar cells †, (2020). https://doi.org/10.1039/d0ra07254k.

[31] L. Nakka, Y. Cheng, A.G. Aberle, F. Lin, Analytical Review of Spiro-OMeTAD Hole Transport Materials: Paths Toward Stable and Efficient Perovskite Solar Cells, Advanced Energy and Sustainability Research 3(8) (2022) 2200045-2200045. https://doi.org/10.1002/AESR.202200045.

[32] A.K. Jena, A. Kulkarni, T. Miyasaka, Halide Perovskite Photovoltaics: Background, Status, and Future Prospects, Chemical Reviews 119(5) (2019) 3036-3103. https://doi.org/10.1021/acs.chemrev.8b00539.

[33] D. Allan, H. Nowell, S. Barnett, M. Warren, A. Wilcox, J. Christensen, L. Saunders, A. Peach, M. Hooper, L. Zaja, S. Patel, L. Cahill, R. Marshall, S. Trimnell, A. Foster, T. Bates, S. Lay, M. Williams, P. Hathaway, G. Winter, M. Gerstel, R. Wooley, A Novel Dual Air-Bearing Fixed-χ Diffractometer for Small-Molecule Single-Crystal X-ray Diffraction on Beamline I19 at Diamond Light Source, Crystals 7(11) (2017) 336-336. https://doi.org/10.3390/cryst7110336.

[34] N. Johnson, P. Waddell, W. Clegg, M. Probert, Remote Access Revolution: Chemical Crystallographers Enter a New Era at Diamond Light Source Beamline I19, Crystals 7(12) (2017) 360-360. https://doi.org/10.3390/cryst7120360.

[35] G.M. Sheldrick, A short history of SHELX, Acta Crystallographica Section A Foundations of Crystallography 64(1) (2008) 112-122. https://doi.org/10.1107/S0108767307043930.

[36] R.C. Clark, J.S. Reid, The analytical calculation of absorption in multifaceted crystals, Acta Crystallographica Section A Foundations of Crystallography 51(6) (1995) 887-897. https://doi.org/10.1107/S0108767395007367.

[37] O.V. Dolomanov, L.J. Bourhis, R.J. Gildea, J.A.K. Howard, H. Puschmann, OLEX2 : a complete structure solution, refinement and analysis program, Journal of Applied Crystallography 42(2) (2009) 339-341. https://doi.org/10.1107/S0021889808042726.

[38] G.M. Sheldrick, SHELXT – Integrated space-group and crystal-structure determination, Acta Crystallographica Section A Foundations and Advances 71(1) (2015) 3-8. https://doi.org/10.1107/S2053273314026370.

Chapter 5. Employing Hole Transport Conducting Oxides ($CuBi_2O_4$ and $NiMnO_4$) beside NiO for Stable and Efficient Inverted Perovskite Solar Cells

Abstract

Chapter 4 discussed the substitution of Spiro-OMeTAD with TPABT in perovskite solar cells; however, limited stability issues were still observed in the resulting devices. To effectively compete with conventional crystalline photovoltaic devices, it remains crucial to explore novel hole-transporting materials that can offer both satisfactory efficiency and stability. In this chapter, we focused on investigating two new hole transport oxides, $CuBi_2O_4$ and $NiMnO_4$, using a novel synthesis method with different variables, such as various salts and hydrothermal treatment of different durations. The XRD patterns of these materials confirmed their crystal structure and alignment with existing databases. Moreover, a perovskite solar cell utilising a spin-coated smooth film of $CuBi_2O_4$ as the hole-transporting material achieved an efficiency of 2.13%. In addition, by employing NiO as the hole-transporting material in an inverted p-i-n solar cell structure, a promising efficiency of 6.40% was attained. These findings highlight the potential of $CuBi_2O_4$ as an alternative material to NiO for inverted perovskite solar cells and underline the importance of exploring new hole transport materials to enhance both efficiency and stability in photovoltaic devices.

5.1 Introduction

Organic-inorganic hybrid perovskites have gained significant interest within the photovoltaic research field since 2012. Perovskite solar cells (PSCs) utilising these materials have seen a remarkable increase in their power conversion efficiency (PCE), reaching up to 26% in 2023[1]. This progress has attracted the attention of researchers in the pursuit of advancing photovoltaic technologies[2]. The low cost of organometal halide perovskite precursors and their convenient solution processability hold great promise for their potential as a future-generation photovoltaic technology. Nonetheless, the primary challenge in their industrial application for photovoltaics lies in their chemical instability, particularly when exposed to high humidity conditions[3]. To establish perovskite as a formidable contender to silicon-based solar cell technology, the perovskite structure needs to undergo modifications that render it inherently stable to environmental conditions. The alternative strategy to address this issue involves the effective encapsulation of PSCs, aiming to prevent the ingress of humidity into the perovskite layer in the cells. In this approach, hole-

transporting materials (HTMs) can serve to enhance the stability of PSCs. Apart from their primary function as a hole-selective layer, which is crucial for achieving high-performance PSCs, HTMs can also act as moisture-blocking layers. This additional role further contributes to the overall stability of the PSC[4, 5]. 2,2',7,7'-tetrakis(N,N-di-p-methoxyphenyl-amine) 9,9'-Spirobifluorene (Spiro-OMeTAD) is recognised as a highly efficient and commonly employed organic hole-conductor in PSCs[6]. It has demonstrated exceptional performance, with power conversion efficiency (PCE) surpassing the 25%[6]. Nevertheless, Spiro-OMeTAD presents a significant disadvantage in terms of cost, particularly at the research scale, where its price exceeds that of gold and platinum by more than ten times[7]. Furthermore, the doping of Spiro-OMeTAD with lithium bis(trifluoromethane sulfonyl)imide (LiTFSI) salt introduces a high hygroscopic[6, 8], which is essentially to enhance the hole conductivity of Spiro-OMeTAD[9]. However, the hygroscopic nature leads to degradation of the perovskite layer. While pre-oxidizing Spiro-OMeTAD can be an alternative to avoid the addition of LiTFSI as a dopant, it comes at the expense of higher cost, rendering it commercially impractical for large-scale applications. In the quest to discover a viable substitute for Spiro-OMeTAD, researchers have explored various alternative HTMs, including but not limited to PTAA, PEDOT:PSS, NiO, and CuO[10]. In this chapter, we focused on investigating two new hole transport oxides materials, $CuBi_2O_4$ and $NiMnO_4$ due to their properties and applications in the energy field.

Several research groups have documented the synthesis and properties of nickel manganese oxide materials for diverse applications. For example, Pang et al. achieved the formation of porous bipyramid, fusiform, and plate-shaped $NiMn_2O_4$ materials through air calcination of oxalate precursors, omitting the use of templates or surfactants[11]. These materials exhibited potential for supercapacitor applications. Kang et al. employed a solvothermal and calcination technique to produce porous hierarchical $NiMn_2O_4$/C nanostructures resembling tremella, showcasing exceptional specific capacity and long-term cycling performance, even under high current densities as cathodes in lithium batteries[12]. Garcia et al. explored the catalytic activity of Ni-doped MnO_x catalysts via a mild hydrothermal reaction involving Ni and Mn, in the presence of various carbon powder substrates[13]. By controlling pH and temperature, they investigated the influence of these substrates on the kinetics of the oxygen reduction reaction (ORR) in an alkaline medium. Menezes et al. synthesized nickel-manganese oxides with adjustable Ni: Mn ratios using heterobimetallic single-source precursors, which proved to be effective catalysts for water oxidation[14].

Moreover, $CuBi_2O_4$ exhibits several appealing characteristics that make it a promising candidate for application as a photocathode in solar water splitting. Firstly, it possesses a band gap ranging from 1.5 to 1.8 eV[15], allowing efficient utilization of a significant portion of the visible spectrum. Secondly, its conduction band minimum (CBM) is positioned at a more negative potential compared to the thermodynamic potential required for water reduction, enabling the production of solar-generated hydrogen (H_2). Thirdly, its valence band maximum (VBM) resides at a significantly more positive potential than p-type Si and p-type Cu_2O, which are presently recognized as highly promising photocathode materials. Consequently, $CuBi_2O_4$ can attain a more positive flat-band potential (>1.0 V vs RHE) and has the potential to achieve a photovoltage (the difference between the thermodynamic reduction potential of water and the onset potential for photocurrent) exceeding 1 V for efficient H_2 evolution.

In this chapter a study was conducted between perovskite solar cells utilising $CuBi_2O_4$ as the hole-transporting material (HTM) and devices employing the inorganic HTM, NiO. A relatively smooth film of $CuBi_2O_4$ was successfully deposited using a spin coater, resulting in a solar cell with a power conversion efficiency (PCE) of 2.13% in an inverted p-i-n structure. To optimise the performance of $CuBi_2O_4$ and achieve a continuous and uniform film, several treatments were employed. These treatments included ball milling with different sizes of balls, both in wet and dry conditions, ultrasonic treatment, and annealing the powder at an appropriate temperature. The effectiveness of these treatments was evaluated through XRD patterns, SEM images, and UV-vis spectroscopy. Ultimately, these optimisation efforts resulted in a significantly improved film quality, with particle sizes ranging from 20 to 25 nm, enhancing charge transfer within the solar cell structure.

The utilisation of $CuBi_2O_4$ as an alternative HTM in perovskite solar cells demonstrates its potential for application in photovoltaic devices. While the achieved PCE of 2.13% may be modest compared to conventional photovoltaic technologies, the chapter highlights the opportunity of exploring novel HTMs to enhance the overall performance of perovskite solar cells. Further research and optimisation efforts are necessary to increase the efficiency of $CuBi_2O_4$-based solar cells.

The investigation of various treatments for $CuBi_2O_4$ synthesis and film formation revealed the significance of controlling the particle size and film morphology for improved charge transfer properties. The use of ball milling, wet and dry grinding, ultrasonic treatment, and annealing was

effective in optimising the properties of the $CuBi_2O_4$ film. By achieving a relatively uniform film with appropriate particle size, the charge transfer within the solar cell was enhanced, contributing to the observed improvement in device performance.

Overall, this chapter sheds light on the potential of $CuBi_2O_4$ as a promising HTM for perovskite solar cells. The results encourage further exploration and optimisation of $CuBi_2O_4$-based devices to enhance their efficiency and stability. By continuing to investigate novel HTMs and refining their synthesis and film deposition techniques, we can advance the development of efficient and stable perovskite solar cells for future photovoltaic applications.

5.2 Synthesis

Synthesis of Cu Bi OH, Ni Mn OH and $Ni(OH)_2$ was done using the reactor, which was constructed in the Gibson laboratory, as shown in Figure 5.1. This reactor delivers (using JASCO HPLC pumps) salt solutions and base such as (NaOH) at a defined flow rate into a stirred reaction vessel, where the pH is maintained and triggered by a feedback loop to control further addition of base as required. Subsequently, the resulting material went through hydrothermal treatment to grow the particles, washing, drying, and annealing processes to transform it into NiO, $CuBi_2O_4$ and $NiMnO_4$. The annealing step was performed in a furnace; however, the suitable temperature for the formation of these materials was initially unknown. Hence, several temperature variations were explored during the project, along with the utilisation of variable temperature X-ray diffraction (XRD) techniques and information obtained from relevant literature sources.

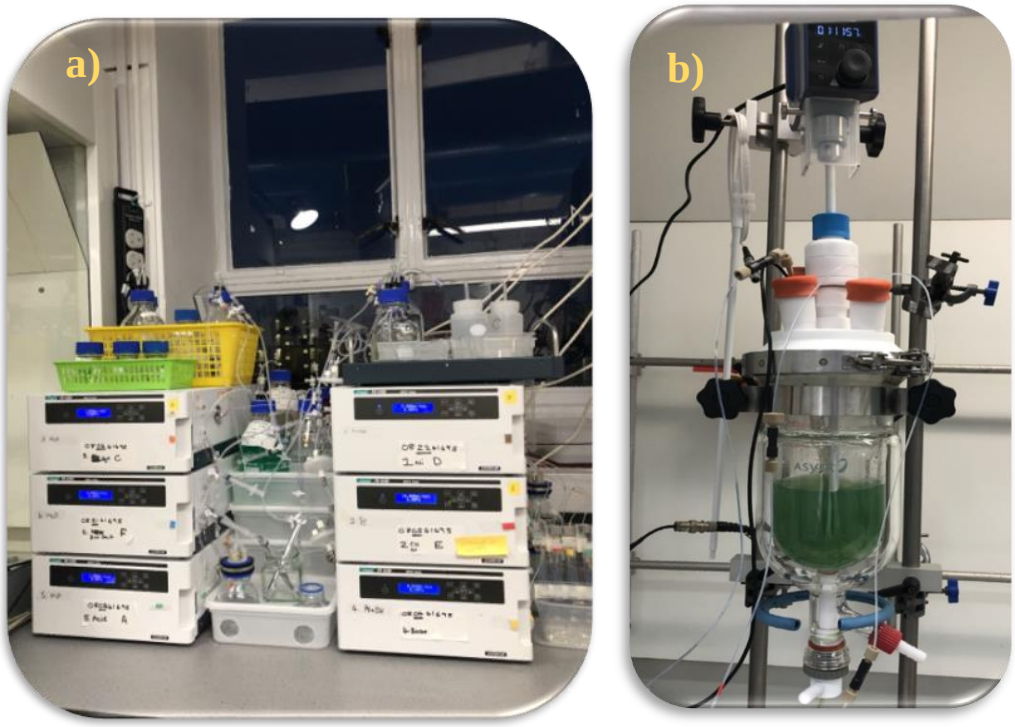

Figure 5.1. a) reactor pumps, b) stirred reaction vessel.

Both bismuth nitrate and bismuth acetate were observed to have low solubility in water. To enhance their solubility, a strong acid was utilised to facilitate dissolution, and subsequently, the resulting solution was diluted. Several acids, acetic acid, hydrochloric acid, and nitric acid were briefly tested for their ability to enhance solubility. Nitric acid exhibited the highest effectiveness in dissolving the salts, approximately twice as effective as acetic acid and about three times more effective than hydrochloric acid. It should be noted that the solution acidified with hydrochloric acid developed an undesired yellow colouration overnight.

The reactor functions by introducing the metal salts and sodium hydroxide concurrently into the reactor vessel in a 1:1 molar ratio. The pH level within the reactor is carefully maintained at a specific value deemed suitable for the formation of the desired metal hydroxides. Table 5.1 and Table 5.2 present the labeling pattern of the samples and their synthesis conditions.

Table 5.1. A summary of NiO and $NiMnO_4$ samples used in this chapter.

Sample Code	Salt type	Hydrothermal treatment (HT)	Sintering	Ball mill	Ultrasonic Horn
Ni O H (Powder)	Nickel acetate tetrahydrate	18 hours at 110°C	-	-	-
NiO (Paste)			30min@450°C	dry powder:2h	15 min
Ni Mn O H-1 (Powder)	Nickel (II) acetate tetrahydrate and manganese (II) acetate tetrahydrate	18 hours at 110°C-directly after reactor	-	-	-
Ni Mn O H-2 (Powder)		18 hours at 110°C-after one day after reactor	-	-	-
Ni Mn O H-3 (Powder)		18 hours at 110°C-after one day after reactor-dried under vacuum oven at 50 °C	-	-	-
$NiMnO_4$-1a (Paste)		18 hours at 110°C-directly after reactor	60min@700°C	dry powder:4 h paste:12 h	4 h

Table 5.2. A summary of $CuBi_2O_4$ samples used in this chapter.

Sample Code	Salt type	Hydrothermal treatment (HT)	Sintering	Ball mill	Ultrasonic Horn
Cu Bi O H-1 (Powder)	Copper acetate and bismuth acetate (A-A)	18 hours at 110°C	-	-	-
$CuBi_2O_4$-1a (Powder)			30min@450°C	-	-
$CuBi_2O_4$-1b (Powder)			30min@700°C	-	-
$CuBi_2O_4$-1c (Paste)			30min@450°C	dry powder:2h	15 min
Cu Bi O H -2 (Powder)	Copper nitrate and bismuth acetate (N-A)	18 hours at 110°C	-	-	-
$CuBi_2O_4$-2a (Powder)			30min@450°C	-	-
$CuBi_2O_4$-2b (Powder)			30min@700°C	-	-
$CuBi_2O_4$-2c (Paste)			30min@450°C	dry powder:2h	15 min
Cu Bi O H -3 (Powder)		18 hours at 110°C	-	-	-

$CuBi_2O_4$-3a (Powder)	Copper nitrate and bismuth nitrate (N-N)		30min@450°C	-	-
$CuBi_2O_4$-3b (Powder)			30min@700°C	-	-
$CuBi_2O_4$-3c (Paste)			30min@450°C	dry powder:2h	15 min
Cu Bi O H -4 (Powder)	Copper nitrate and bismuth nitrate (N-N)	18 hours at 110°C	-	-	-
$CuBi_2O_4$-4a (Powder)			30min@450°C	-	-
$CuBi_2O_4$-4b (Powder)			30min@700°C	-	-
$CuBi_2O_4$-4c (Paste)			30min@450°C	dry powder:2-4h paste:4-12 h	2-4 h
Cu Bi O H -5 (Powder)	Copper nitrate and bismuth nitrate (N-N)	8 hours at 110°C	-	-	-
$CuBi_2O_4$-5a (Powder)			30min@450°C	-	-
$CuBi_2O_4$-5b (Powder)			30min@700°C	-	-

$CuBi_2O_4$-5c (Paste)			30min@450°C	dry powder:4 h paste:12 h	4 h

5.3 Results and Discussion

5.3.1 Powder X-ray Diffraction (PXRD)

The phase identification and characterization of NiO, $CuBi_2O_4$, and $NiMnO_4$ materials were performed using Powder X-ray diffraction (PXRD) measurements on both powder and thin film samples. Figure 5.2 presents the X-ray diffraction (XRD) pattern obtained from NiO nanoparticles, scanned in the 2θ range of 20 to 100 degrees for variable temperatures. The pattern confirmed the crystallinity of the NiO nanostructures. The observed peaks at 2θ values of 37.24°, 43.26°, 62.84°, 75.34°, and 79.30° can be attributed to the (111), (200), (220), (311), and (222) crystallographic planes, respectively. These peak positions align well with the previous study (JSPDS Card no. 65–2901)[16, 17]. Furthermore, no additional peaks were observed in the XRD patterns between 250°C and 850°C, indicating the complete decomposition of precursors and impurities. This absence of impurity peaks indicates the high purity of the synthesized NiO nanoparticles.

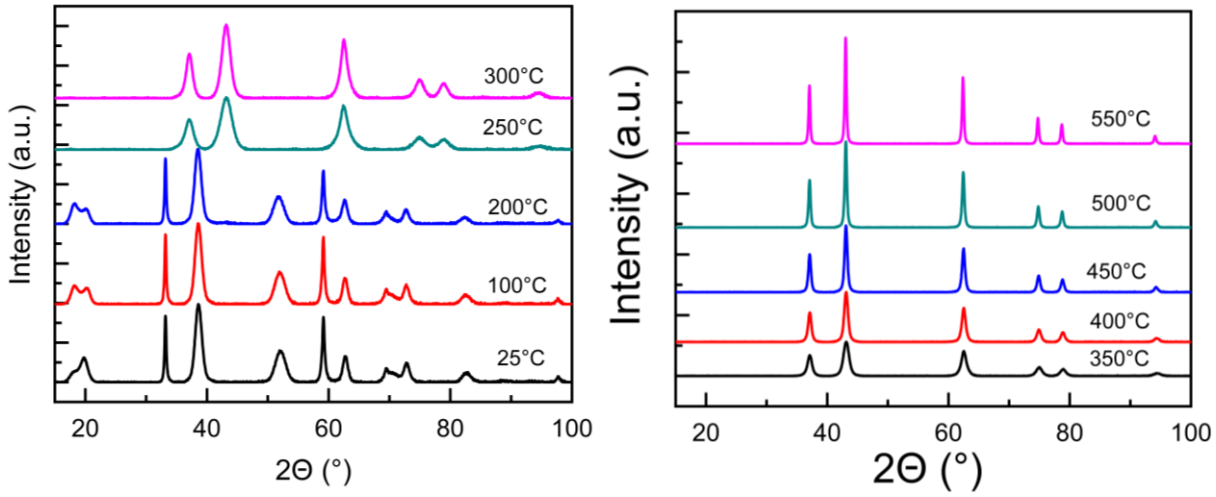

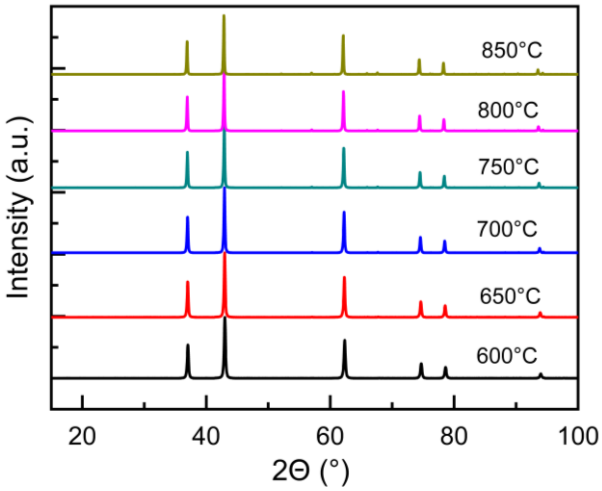

Figure 5.2. Powder X-ray diffraction pattern of (Ni O H) synthesised by reactor, and then annealed of variable temperature using a Panalytical instrument.

Table 5.3 provides a summary of the XRD analysis results for (Ni O H) at variable temperatures, with an average particle size of 20 nm. Among the samples, the smallest particle size, 14 nm, was obtained at a sintering temperature of 300°C, while the medium-sized particles, with sizes of 20 nm and 25 nm, were obtained at sintering temperatures of 450°C and 500°C, respectively. Generally, as the sintering temperature increased, the mean crystallite size increased. This correlation suggests that higher sintering temperatures promote the growth of crystalline domains within the material.

Table 5.3. Extracted crystallite size from the variable temperature pXRD analysis of (Ni O H) fitted to the Scherrer equation.

Materials	**Temperature °C**	**Peak position (°2θ)**	**FWHM (B obs.)**	**$B_{standard}$**	**$B_{structural}$**	**Size (Å)**	**Size (nm)**	**Average Size (nm)**
Ni O H	25°C	33.1883°	0.277	0	0.277	299	29.9	25.3

		59.147°	0.356	0	0.356	256	25.6	
		69.414°	0.475	0	0.475	203	20.3	
	100°C	33.180°	0.317	0	0.317	262	26.2	
		59.114°	0.356	0	0.356	256	25.6	23.1
		69.456°	0.554	0	0.554	174	17.4	
	200°C	33.178°	0.317	0	0.317	261	26.1	
		59.134°	0.436	0	0.436	209	20.9	20.3
		72. 624°	0.713	0	0.713	138	13.8	
	250°C	62.354°	0.950	0	0.950	98	9.8	
		78.970°	0.634	0	0.634	162	16.2	13
	300°C	43.264°	1.188	0	1.188	72	7.2	
		79.066°	0.475	0	0.475	217	21.7	14.5
	350°C	43.272°	0.950	0	0.950	90	9	
		62.483°	0.475	0	0.475	196	19.6	15.4
		37.971°	0.475	0	0.475	177	17.7	
	400°C	43.176°	0.594	0	0.594	144	14.4	
		62.482°	0.634	0	0.634	147	14.7	20.2
		74.856°	0.317	0	0.317	316	31.6	
	450°C	62.482°	0.594	0	0.594	156	15.6	
		78.830°	0.436	0	0.436	236	23.6	20
	500°C	43.057°	0.396	0	0.396	216	21.6	
		62.438°	0.436	0	0.436	213	21.3	22

		74.807°	0.436	0	0.436	230	23.0	
	550°C	43.034°	0.317	0	0.317	270	27	
		74.766°	0.317	0	0.317	316	31.6	29
		78.703°	0.356	0	0.356	288	28.8	
	600°C	37.038°	0.277	0	0.277	302	30.2	
		62.343°	0.277	0	0.277	335	33.5	31.5
		43.005°	0.277	0	0.277	308	30.8	
	650°C	37.013°	0.238	0	0.238	353	35.3	37.2
		62.291°	0.238	0	0.238	391	39.1	
	700°C	42.939°	0.238	0	0.238	359	35.9	
		62.241°	0.238	0	0.238	391	39.1	39
		74.561°	0.238	0	0.238	420	42	
	750°C	74.496°	0.198	0	0.198	504	50.4	46.8
		78.407°	0.238	0	0.238	431	43.1	
	800°C	36.937°	0.198	0	0.198	423	42.3	44.6
		62.142°	0.198	0	0.198	468	46.8	
	850°C	36.914°	0.198	0	0.198	423	42.3	42.7
		42.848°	0.198	0	0.198	431	43.1	

The XRD analysis was performed on Cu Bi OH and Ni Mn OH samples at variable temperatures, and the resulting XRD patterns are presented in Figure 5.3 and Figure 5.4, respectively. The patterns were recorded with a step size of 0.03° over the range of 20° to 100°. The observed diffraction pattern for $CuBi_2O_4$ confirms the formation of a spinel structure, which is consistent with the reference pattern (JCPDS no. 80-1478)[18, 19]. Similarly, the XRD pattern for $NiMnO_4$

also corresponds to the spinel structure, in agreement with the reference pattern (JCPDS no. 71-0852).

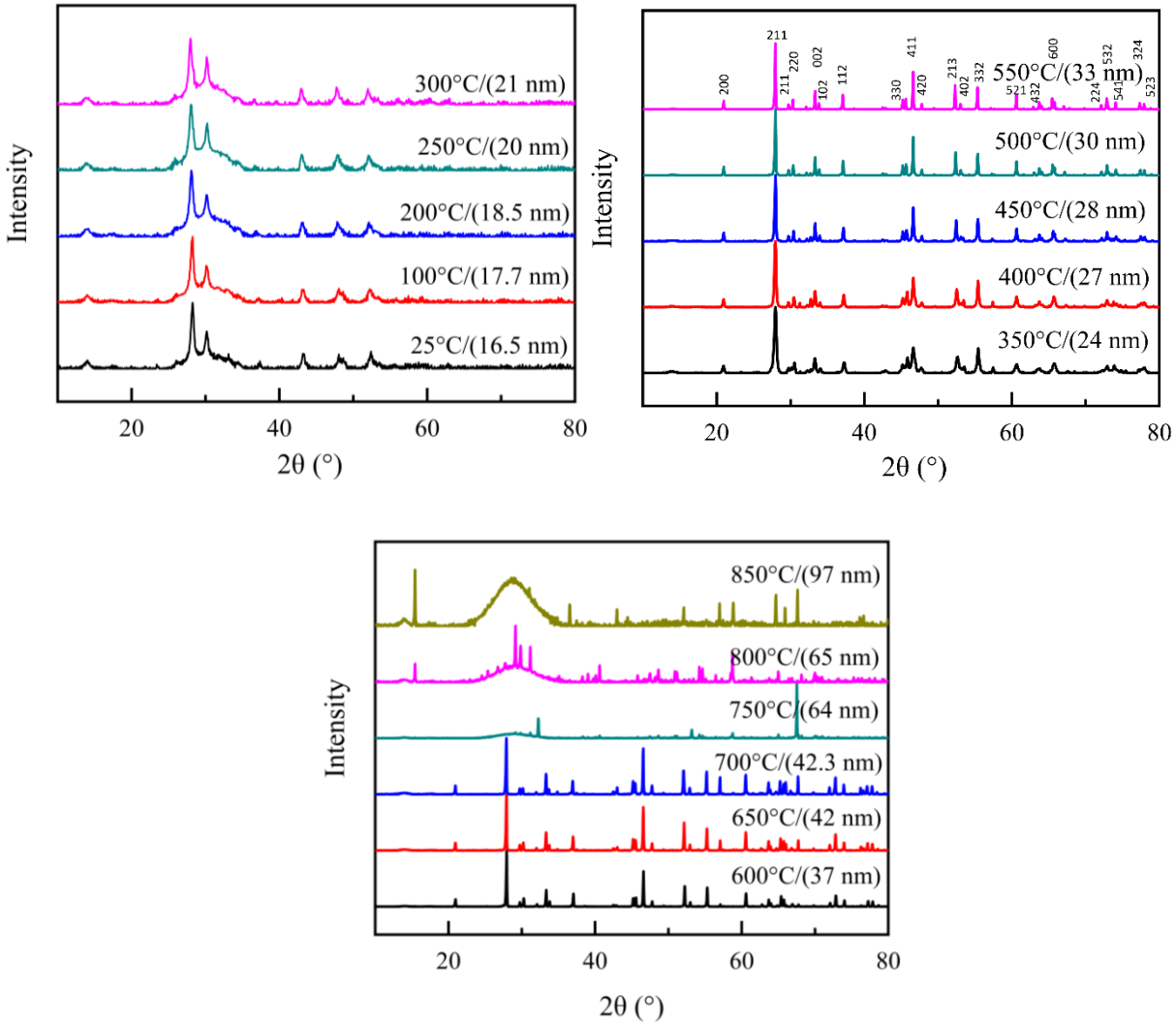

Figure 5.3. Powder X-ray diffraction pattern of (Cu Bi_2 O H) synthesised using the co-precipitation reactor, annealed of variable temperature using Panalytical instrument.

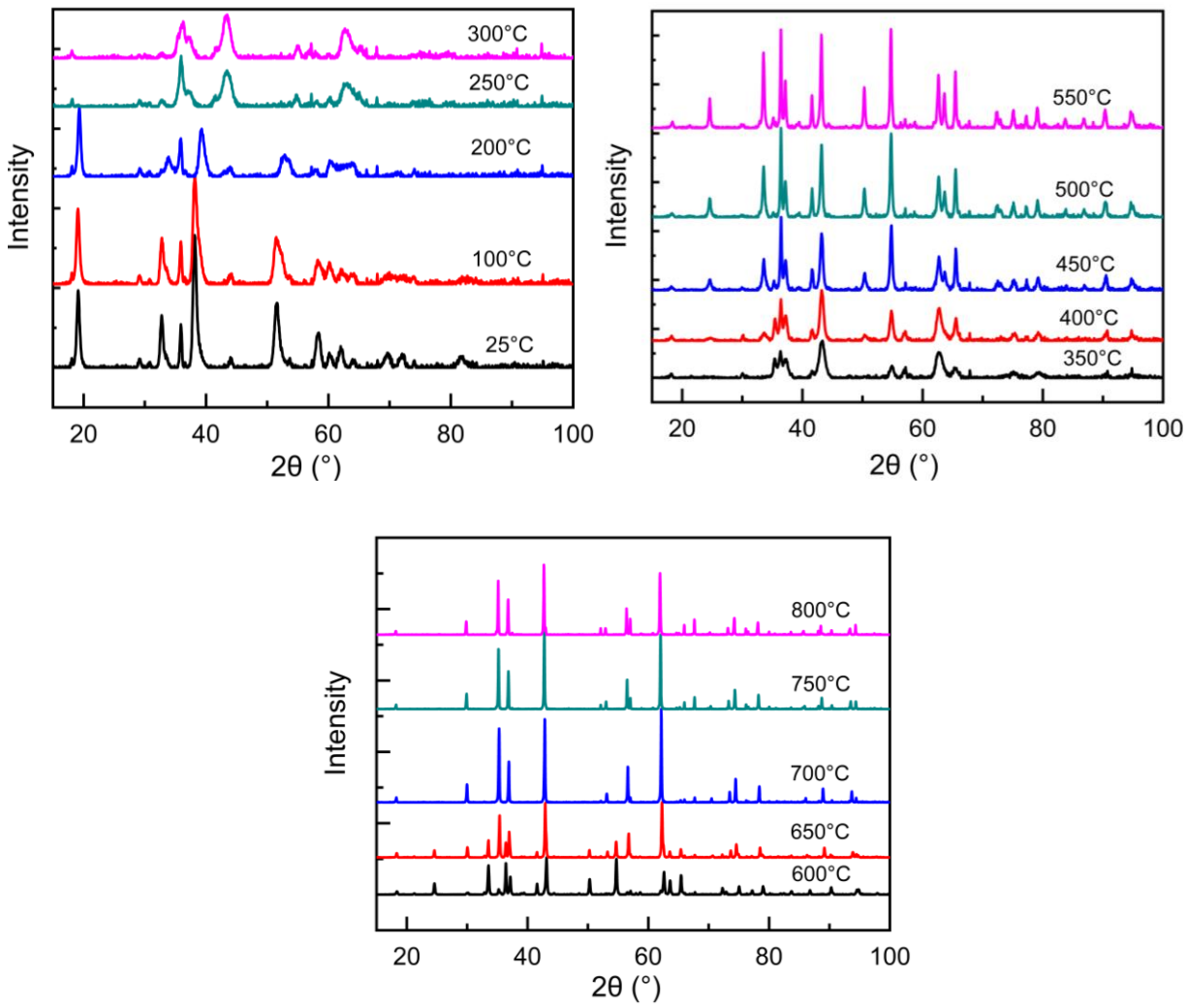

Figure 5.4. Powder X-ray diffraction pattern of (Ni Mn O H) synthesised using the co-precipitation reactor, annealed of variable temperature using Panalytical instrument.

Table 5.4 summarises the XRD analysis results for Cu Bi OH, while Table 5.5 provides the corresponding summary for Ni Mn OH, both at variable temperatures. These tables offer key information regarding the crystallographic properties of the samples, including particle size. By comparing the experimental data with known reference patterns, the phase composition a crystal structure of Cu Bi OH and Ni Mn OH at different temperatures can be accurately determined.

Table 5.4. Extracted crystallite size from the variable temperature pXRD analysis of (Cu Bi_2 O H) fitted to the Scherrer equation.

Materials	**Temperature °C**	**Peak position (°2θ)**	**FWHM (B obs.)**	**$B_{standard}$**	**$B_{structural}$**	**Size (Å)**	**Size (nm)**	**Average Size (nm)**
Cu Bi O H	25°C	37.36	0.5196	0	0.5196	161	16	16.5
		52.42	0.5196	0	0.5196	170	17	
	100°C	43.16	0.39	0	0.39	219	21.9	17.7
		48.02	0.65	0	0.52	134	13.4	
	200°C	28.14	0.39	0	0.39	210	21	18.5
		47.93	0.52	0	0.52	167	16.7	
	250°C	47.9	0.52	0	0.52	167	16.7	20
		43.13	0.36	0	0.36	239	23.9	
	300°C	47.8	0.39	0	0.39	223	22.3	21
		52.02	0.45	0	0.45	194	19.4	
	350°C	32.35	0.32	0	0.32	258	25.8	24
		65.8	0.42	0	0.42	224	22.4	
	400°C	60.63	0.32	0	0.32	288	28.8	27
		65.7	0.36	0	0.36	265	26.5	
	450°C	27.99	0.23	0	0.23	360	36	28

		69.92	0.39	0	0.39	249	24.9	
		57.42	0.39	0	0.39	232	23.2	
	500°C	49.5	0.26	0	0.26	337	33.7	30
		69.9	0.39	0	0.39	249	24.9	
	550°C	29.46	0.195	0	0.195	422	42.2	
		57.18	0.26	0	0.26	348	34.8	33
		38.59	0.39	0	0.39	216	21.6	
	600°C	49.43	0.39	0	0.39	224	22.4	
		69.9	0.39	0	0.39	307	30.7	37
		63.9	0.16	0	0.16	576	57.6	
	650°C	63.66	0.12	0	0.12	787	78.7	
		66.85	0.4	0	0.4	240	24	42
		62.64	0.39	0	0.39	238	23.8	
	700°C	52.1	0.16	0	0.16	544	54.4	42.3
		69.8	0.32	0	0.32	303	30.3	
	750°C	32.27	0.23	0	0.23	637	63.7	64
	800°C	40.6	0.13	0	0.13	652	65.2	65
	850°C	64.65	0.097	0	0.097	965	96.5	97
		67.6	0.097	0	0.097	982	98.2	

Table 5.5. Extracted crystallite size from the variable temperature pXRD analysis of (Ni Mn O H) fitted to the Scherrer equation.

Materials	**Temperature °C**	**Peak position (°2θ)**	**FWHM (B obs.)**	**$B_{standard}$**	**$B_{structural}$**	**Size (Å)**	**Size (nm)**	**Average Size (nm)**
Ni Mn O H	25°C	38.169	0.520	0	0.520	162	16.2	15.7
		51.617	0.585	0	0.585	151	15.1	
	100°C	38.175	0.455	0	0.455	185	18.5	25.3
		35.908	0.260	0	0.260	321	32.1	
	200°C	19.327	0.390	0	0.390	207	20.7	15.25
		52.790	0.909	0	0.909	98	9.8	
	250°C	35.912	0.4546	0	0.455	184	18.4	18.4
	300°C	36.267	0.649	0	0.649	129	12.9	12.9
	350°C	54.813	0.554	0	0.554	161	16.1	38.25
		67.853	0.158	0	0.158	604	60.4	
	400°C	43.197	0.436	0	0.436	196	19.6	40
		67.827	0.158	0	0.158	604	60.4	
	450°C	54.814	0.325	0	0.325	276	27.6	24
		43.318	0.422	0	0.422	203	20.3	
	500°C	54.784	0.292	0	0.292	306	30.6	30.3

		50.340	0.292	0	0.292	300	30	
	550°C	65.458	0.325	0	0.325	291	29.1	30
		54.739	0.292	0	0.292	306	30.6	
	600°C	43.157	0.227	0	0.227	376	37.6	47.9
		65.419	0.162	0	0.162	581	58.1	
	650°C	35.381	0.195	0	0.195	428	42.8	40.2
		42.924	0.227	0	0.227	376	37.6	
	700°C	36.914	0.162	0	0.162	516	51.6	47.7
		42.855	0.195	0	0.195	438	43.8	
	750°C	42.775	0.195	0	0.195	438	43.8	47.2
		29.916	0.162	0	0.162	506	50.6	
	800°C	36.795	0.162	0	0.162	516	51.6	47.7
		42.719	0.195	0	0.195	438	43.8	

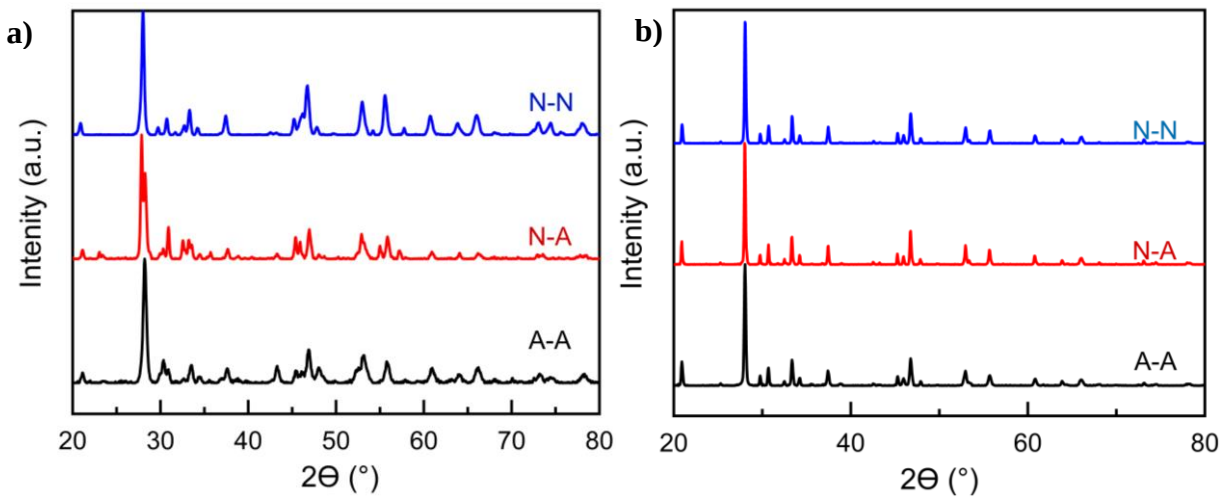

Figure 5.5. Powder X-ray diffraction pattern of (Cu Bi OH) synthesised from different salts, (A-A) copper acetate and bismuth acetate, (N-A) copper nitrate and bismuth acetate, (N-N) copper nitrate and bismuth nitrate, and then annealed the powder at a) 450°C, b) 700°C depending on transition temperature in TGA measurements.

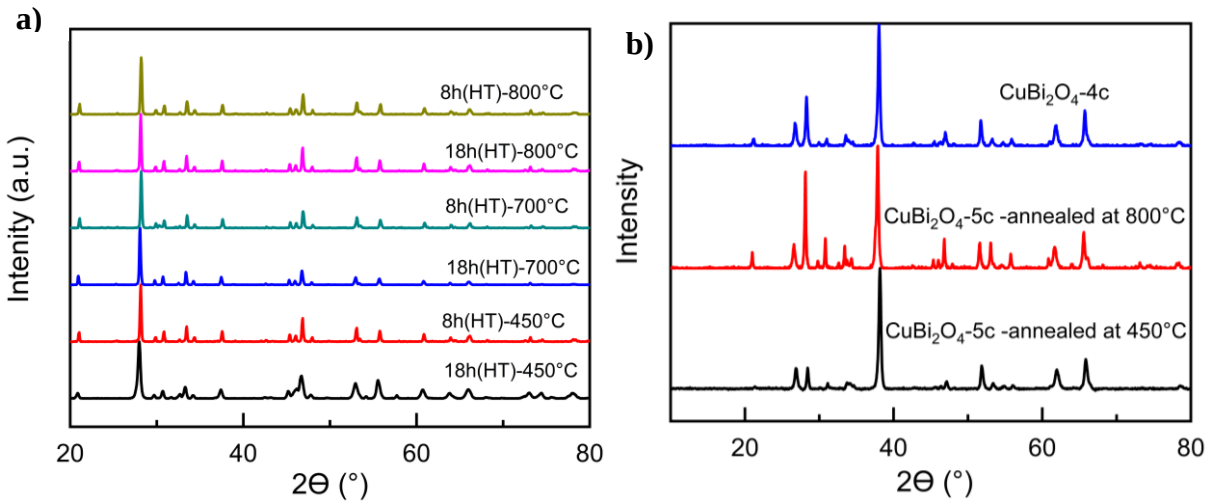

Figure 5.6. Powder X-ray diffraction pattern of (Cu Bi O H) synthesised from copper nitrate and bismuth nitrate(N-N), hydrothermal treatment (HT) at 110°C for 18h and 8h, then annealed the powder at 450°C and 700°C to determine for the products formed at the transition temperatures derived from the TGA measurements. a) as powder, b) as film on FTO.

5.3.2 Thermal Properties

The thermal properties of Cu Bi O H, Ni Mn O H, and Ni O H powders and pastes were investigated to evaluate their suitability for photovoltaic applications, considering the importance of thermal and chemical stability in high-temperature environments. To assess the thermal behaviour, thermogravimetric analysis (TGA) was performed by monitoring weight changes as a function of temperature. The TGA curves, depicted in Figure 5.7 and summarised in Table 5.6 were obtained by heating the samples from 25°C to 700°C under a nitrogen atmosphere at a heating rate of 5°C/min.

The TGA curves exhibited three distinct weight loss steps. The initial significant weight loss observed in the TGA curves of Cu Bi OH (Figure 5.7 (a) and (b)), and Ni Mn O H (Figure 5.7 (c)) can be attributed to the evaporation of water molecules of crystallization [20]. This weight loss indicates the removal of water from the crystalline structures of these materials. The subsequent weight loss observed in the second step can be associated with the thermal decomposition of hydroxide into oxide nanoparticles. As the samples were heated up to 700°C, the TGA curves exhibited a consistent slope without any noticeable weight loss, suggesting the absence of organic substances and the formation of a pure crystalline phase. This finding is consistent with previously reported results by Barzinjy, *et al.* [20], further validating the thermal stability and absence of impurities in the studied materials. These results highlight the excellent thermal properties and stability of $CuBi_2O_4$, $NiMnO_4$, and NiO, making them promising candidates for photovoltaic applications where operating temperatures can exceed 80°C. The observed weight stability up to 700°C confirms their resistance to thermal degradation and indicates their potential suitability for high-temperature device environments.

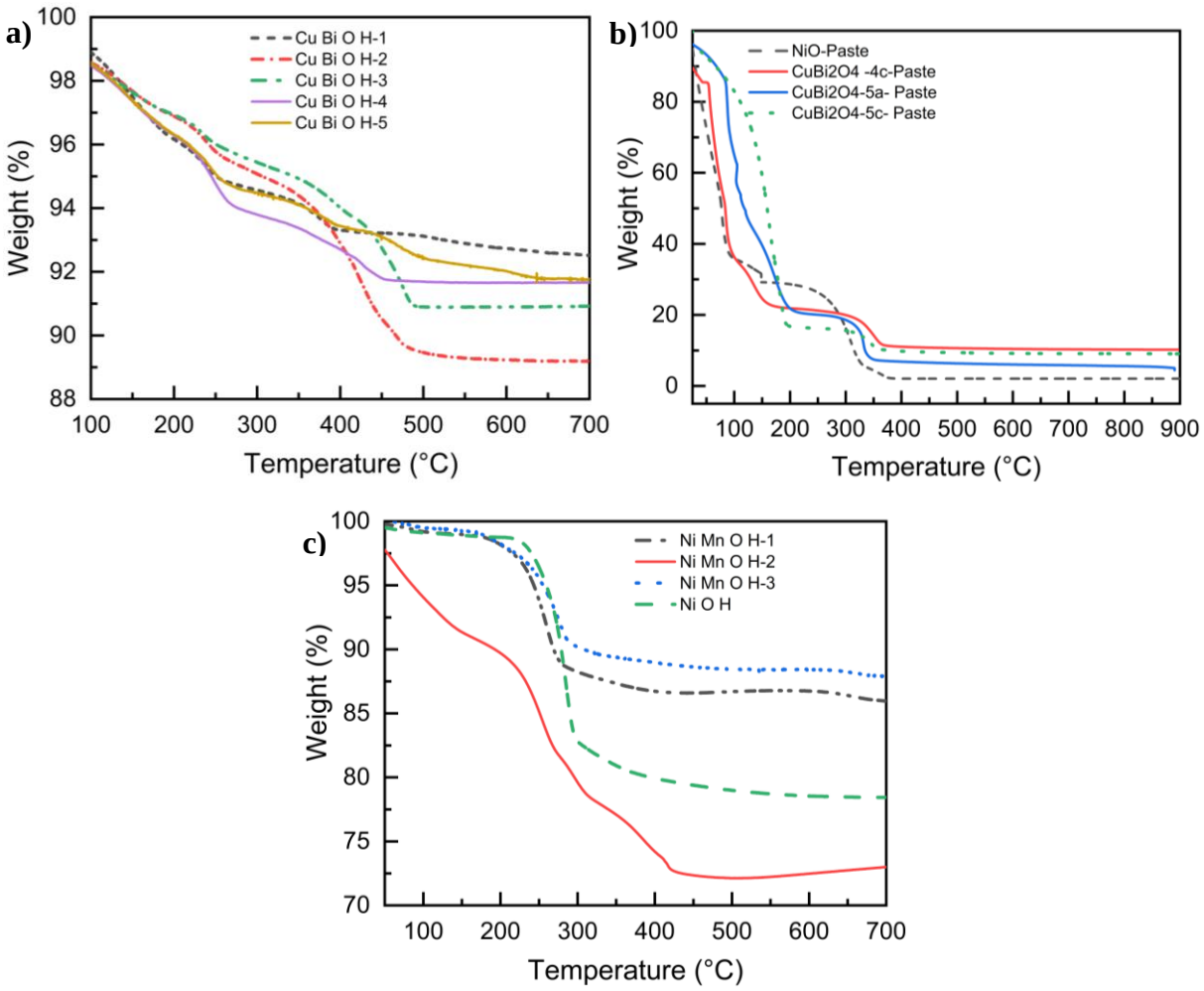

Figure 5.7. Thermogravimetric analysis of a) Cu Bi O H powder for different variables, b) $CuBi_2O_4$ paste (different conditions) and NiO paste and c) Ni Mn O H powder for different variables and Ni O H powder, all at a heating rate of 5°C min^{-1} under N_2 atmosphere samples codes details given in Table 5.1 and Table 5.2 above.

Table 5.6. Summary of samples used to study thermal properties of p-type materials.

Ni O and Ni Mn O H based		Cu Bi O H based	
Sample	T_d(°C)[a]	Sample	T_d(°C)[a]
Ni O H (Powder)	230	Cu Bi OH-1 (Powder)	250 and 358
NiO (Paste)	150 and 257	Cu Bi OH -2 (Powder)	217 and 355
Ni Mn O H-1 (Powder)	207	Cu Bi OH -3 (Powder)	225 and 423
Ni Mn O H-2 (Powder)	219 and 312	Cu Bi OH -4 (Powder)	200, 267 and 400
Ni Mn O H-3 (Powder)	200	$CuBi_2O_4$-4c (Paste)	166 and 322
Ni Mn O H-1 (Powder)	207	Cu Bi OH -5 (Powder)	254, 406 and 512
Ni Mn O H-2 (Powder)	219 and 312	$CuBi_2O_4$-5a (Paste)	209 and 315

		$CuBi_2O_4$-5c (Paste)	199 and 311
		Cu Bi OH-1 (Powder)	250 and 358

5.3.3 Film Morphology

All the NiO, $CuBi_2O_4$ and $NiMnO_4$ samples were based on nanoparticles prepared and applied as a paste (films) on FTO. Full details for each sample are given in the synthesis section and Table 5.1 and Table 5.2 In general, the particle shape and film morphology were different for each sample. Figure 5.8 illustrates the scanning electron microscope (SEM) images of the $CuBi_2O_4$ film prepared using the reactor and deposited on the fluorine-doped tin oxide (FTO) substrate. The quality of film formation plays a crucial role in enhancing charge transfer efficiency and increasing material conductivity. Figure 5.8(a) depicts a film prepared from copper nitrate and bismuth acetate, that underwent hydrothermal treatment for 18 hours at 110 °C. Subsequently, the material was sintered in an oven at 450 °C for half an hour. Upon examination, it was observed that the particle size was large and that certain regions of the FTO were exposed. Moreover, the conductivity of the film was relatively low, measuring approximately 6.5×10^{-7} (S/cm). In an attempt to address these issues, the material was prepared in a similar manner, but this time copper nitrate and bismuth nitrate were used. Figure 5.8(b) showcases the resulting film, where the particle size remained large, and some areas of the FTO were still exposed. In Figure 5.8(c) and (d), the paste obtained from image Figure 5.8(b) was subjected to grinding using a ball mill for durations ranging from 4 to 12 hours. A noticeable change in particle size was observed, although some particles remained unground. To overcome this challenge, the material was used dry grind for two hours after sintering, followed by a four-hour treatment using an ultrasonic horn. Additionally, the paste was ground for 12 hours, as depicted in Figure 5.8 (e), resulting in improved coverage of the FTO regions. Furthermore, to minimise particle growth, the heat treatment time was reduced from

18 hours to 8 hours. The same procedure as before was followed, with the powder being sintered at 450 °C (Figure 5.8 f) and then at 800 °C for half an hour (Figure 5.8 g) to achieve the desired film characteristics. Figure 5.9, depicts the SEM for a low-resolution image of NiO (Figure 5.9 (a)), providing an overall view of the material's morphology and structure. In Figure 5.9 (b), a high-resolution SEM image of NiO is displayed, allowing for a closer examination of its surface features and finer details. Moving on to Figure 5.9 (c) depicts $NiMnO_4$ that was annealed at 700°C, and ball milled the paste for 12 hours with a weight percentage of 50. The SEM image reveals the morphology and structure of this sample, indicating the effects of ball milling and annealing on its characteristics. Lastly, Figure 5.9(d) portrays $NiMnO_4$ that underwent the same annealed temperature and ball milling process for 12 hours but with a lower weight percentage of 20. The SEM image provides insight into the morphology and structure of this sample, highlighting any variations in comparison to the previous sample. Overall, the SEM images provide valuable visual information regarding the surface characteristics and structural properties of the different samples deposited on FTO glass.

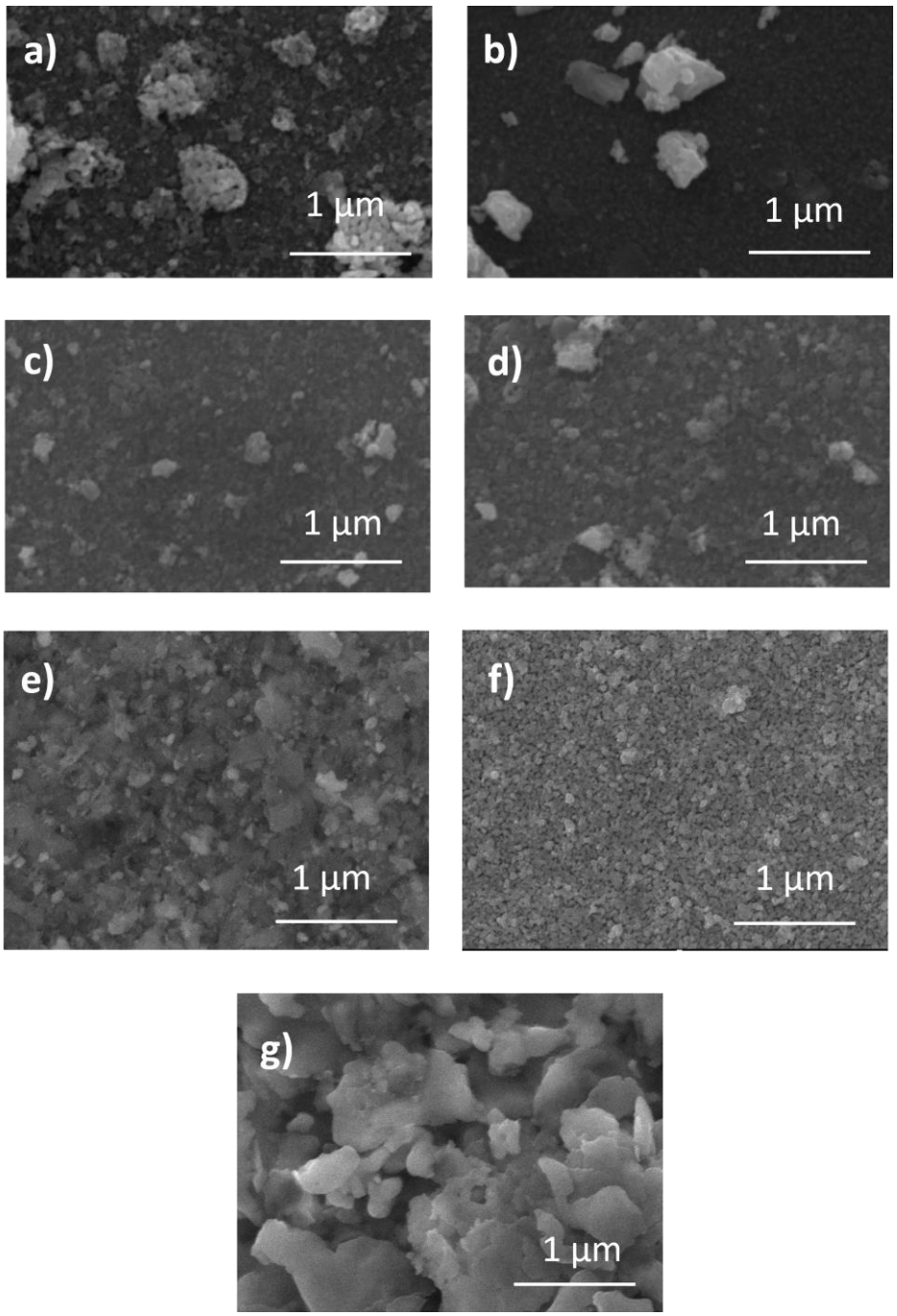

Figure 5.8. SEM images for the film deposited on FTO glass *of a)* $CuBi_2O_4$ -2*c,b)* $CuBi_2O_4$ -*3c,c)* $CuBi_2O_4$ -*4c (4 h* ball milling for paste*), d)*$CuBi_2O_4$ -*4c (12 h* ball milling for paste*), e)*$CuBi_2O_4$ -*4c (4 h* ball milling for dry powder and 12 h ball milling for the paste*),f)* $CuBi_2O_4$ -*5c (4 h* ball milling for dry powder which annealed at 450°C and 12 h ball milling for the paste),and g)$CuBi_2O_4$ -*5c (4 h* ball milling for dry powder which annealed at 800°C and 12 h ball milling for the paste). all sample (14000×magnification),20kV. samples codes details in Table 5.2 above.

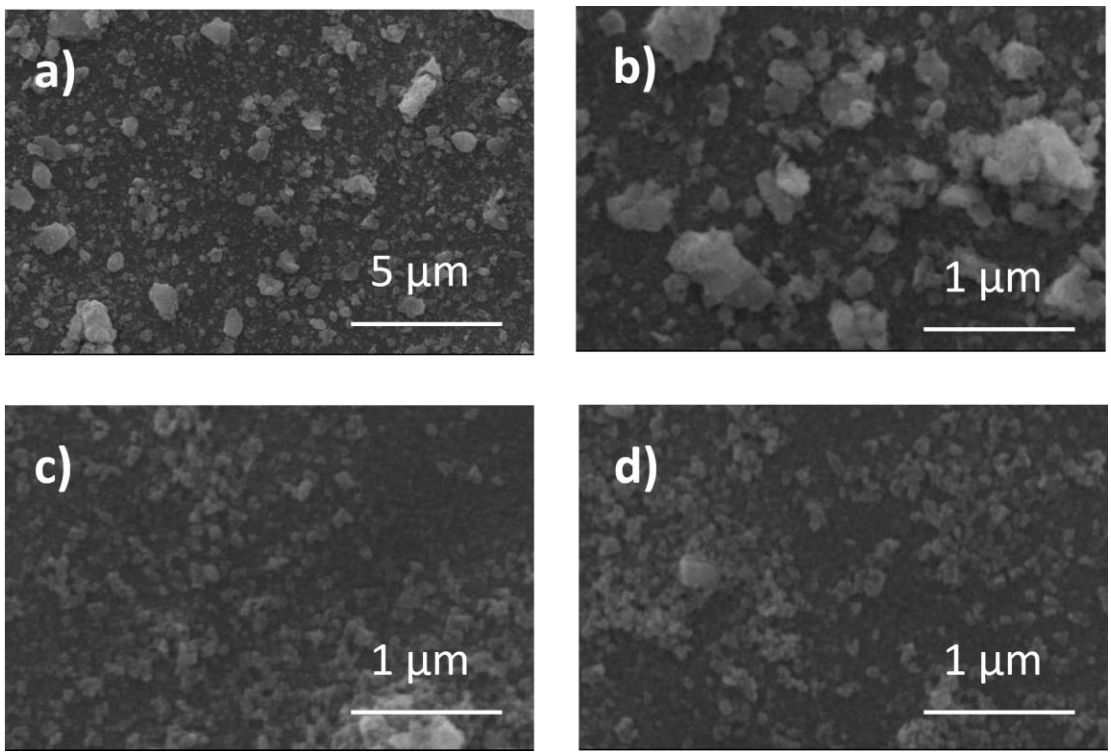

Figure 5.9. SEM images of a) low-resolution of NiO, b) high-resolution of NiO, c) $NiMnO_4$ ball milled for 12h (50wt%) annealed at 700°C, and d) $NiMnO_4$ ball milled for 12h (20wt%) annealed at 700°C, deposited on FTO glass, respectively. samples codes details given in Table 5.1above.

5.3.4 Optical and Electrochemical Characterisation

To optimize the light-harvesting efficiency of the perovskite layer in solar cells, the reduction of parasitic absorption losses and enhancement of generated current is crucial. A significant aspect of achieving this optimization involves minimizing light absorption by HTM within the visible light range of 400–800 nm. To investigate the optical properties of the $CuBi_2O_4$, $NiMnO_4$, and NiO films, UV-visible absorption spectroscopy was utilised. Analysis of the spectra and measurements revealed noticeable variations among the films in terms of their broad absorption features, which can be attributed to differences in film formation, as observed in the SEM images. These findings emphasize the importance of comprehending the optical properties of HTM materials to optimize their performance and minimize light absorption losses, ultimately enhancing solar cell efficiency.

Figure 5.10 demonstrates the optical properties of the $CuBi_2O_4$ samples labelled $CuBi_2O_4$-2C , $CuBi_2O_4$-3C. These samples exhibited lower light absorption in both the ultraviolet and visible light regions. Correspondingly, the SEM images of these samples revealed exposed substrate

regions and the presence of large-sized particles. The scattering of light caused by these particles led to a decrease in absorption. On the other hand, the samples ($CuBi_2O_4$-4C) subjected to grinding using ball milling for different durations exhibited ultraviolet light absorption at a wavelength of 350 nm, gradually decreasing in the visible light region. This decrease can be attributed to the reduction in particle size, resulting in less scattering.

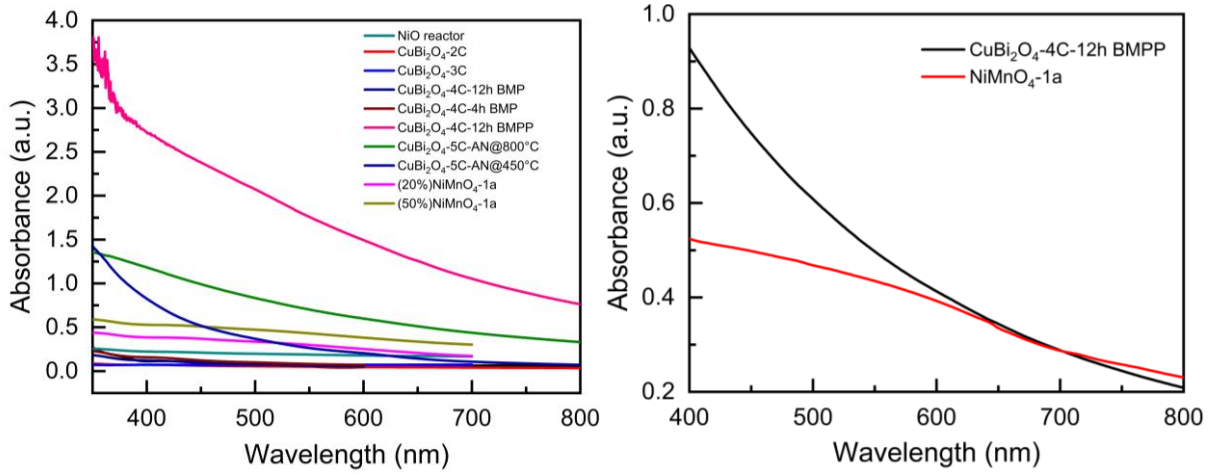

Figure 5.10. UV-Vis measurements for $CuBi_2O_4$, $NiMnO_4$, and NiO films prepared in different variables as shown in Table 5.1and Table 5.2 a) doctor blade films on FTO, b) spin coated films on glass. BMP: Bill mailing paste, BMPP: Bill milling powder and paste, AN: annealed.

Regarding the optical properties of NiO and $NiMnO_4$, the light absorption characteristics were indicative of film formation. The NiO film displayed large particles, while the $NiMnO_4$ films produced through ball milling exhibited less dispersion due to the smaller particle size. These optical property observations further underscore the influence of film morphology on light absorption behaviour. The experiment utilized a three-electrode system consisting of a working electrode made of either $CuBi_2O_4$ or $NiMnO_4$ films on FTO glass, a Ag/Ag^+ reference electrode made of (AgCl in 3 M KCl aqueous solution), and a Pt wire counter electrode. These electrodes were placed in a 50 mM phosphate buffer electrolyte solution at pH 7. cyclic voltammetry (CV) was carried out with a scan rate of 10 - 100 mV s^{-1}.

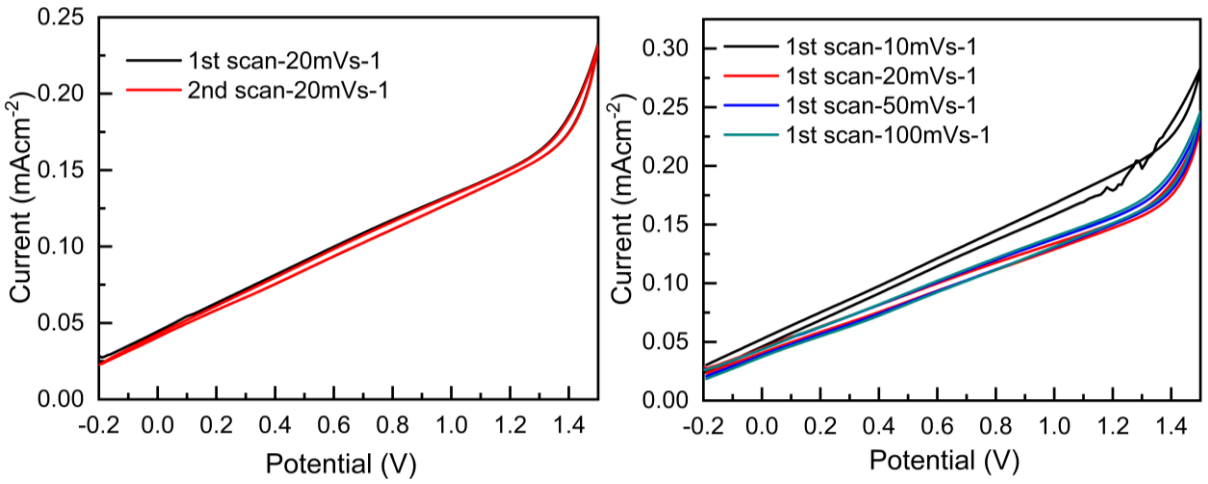

Figure 5.11. Cyclic voltammograms of fluorine-doped tin oxide (FTO), recorded in phosphate buffer (0.05M pH 7) at different scan rates 10, 20, 50, and 100 mV s^{-1}.

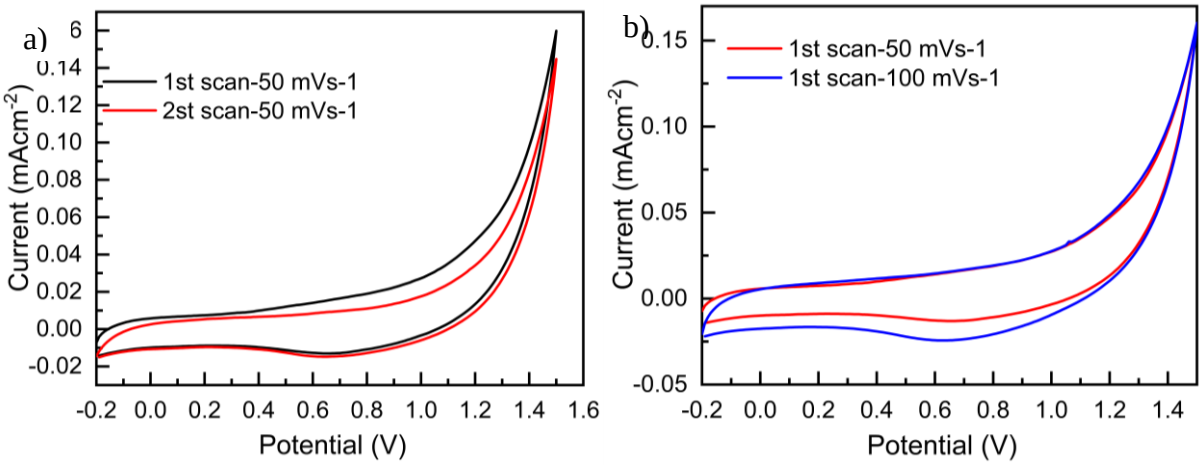

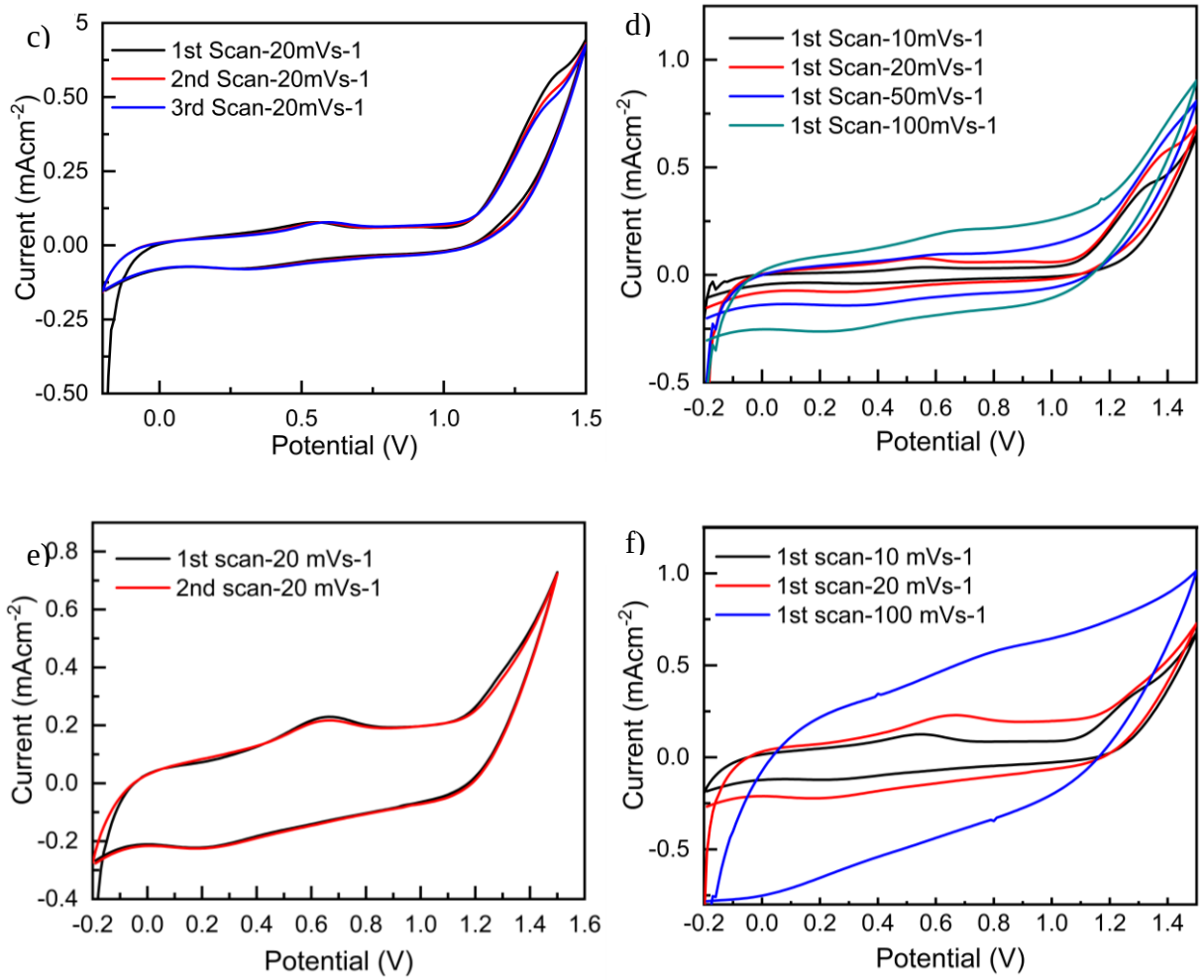

Figure 5.12. Cyclic voltammograms of a), b) $CuBi_2O_4$-4C, c), d) $NiMnO_4$-1a (screen printer film) and e), f) $NiMnO_4$-1a (doctor blade film), recorded in phosphate buffer (0.05 M pH 7) at different scan rates, 10, 20, 50, and 100 mV s^{-1}.

5.3.5 Photoluminescence Measurements

One crucial aspect of an effective p-type hole transporting layer is its ability to selectively extract holes from the perovskite absorber layer while "reflecting" electrons. This process plays a critical role in preventing electron-hole pair recombination and increasing the power conversion efficiency (PCE) of solar cells. Photoluminescence (PL) can be used as a means to assess the effectiveness of hole extraction, as the rate of PL quenching provides valuable insights into charge extraction. Figure 5.13 a) and b) (Table 5.7) depict the time-resolved and steady-state PL data of perovskite films coated with NiO or $CuBi_2O_4$, in comparison to the bare perovskite film. The PL quenching

is observed to occur for the films coated with NiO, and $CuBi_2O_4$, not for NiMnO4 (Figure 5.13 c and Table 5.8), indicating equally effective hole extraction. However, hole extraction is only one part of the process. To achieve high performance, the extracted holes must be effectively transported to the electrode. This transportation is crucial for facilitating efficient charge transfer and reducing losses due to recombination. The optimization of both hole extraction and hole transportation processes is essential for enhancing the overall performance of solar cells. Further investigations and characterization techniques are necessary to evaluate the hole transportation properties of the studied materials and to determine their suitability for use in efficient photovoltaic For $CuBi_2O_4$ and $NiMnO_4$ to work well as hole-selective contact in photovoltaic devices, they must be able to efficiently extract holes from the perovskite absorber layer. Photoluminescence (PL) spectroscopy is a useful method for monitoring the efficiency of charge extraction at the electron and hole selective contacts. By measuring the rate and degree of PL quenching, it is possible to determine how effectively charges are being extracted from the device.

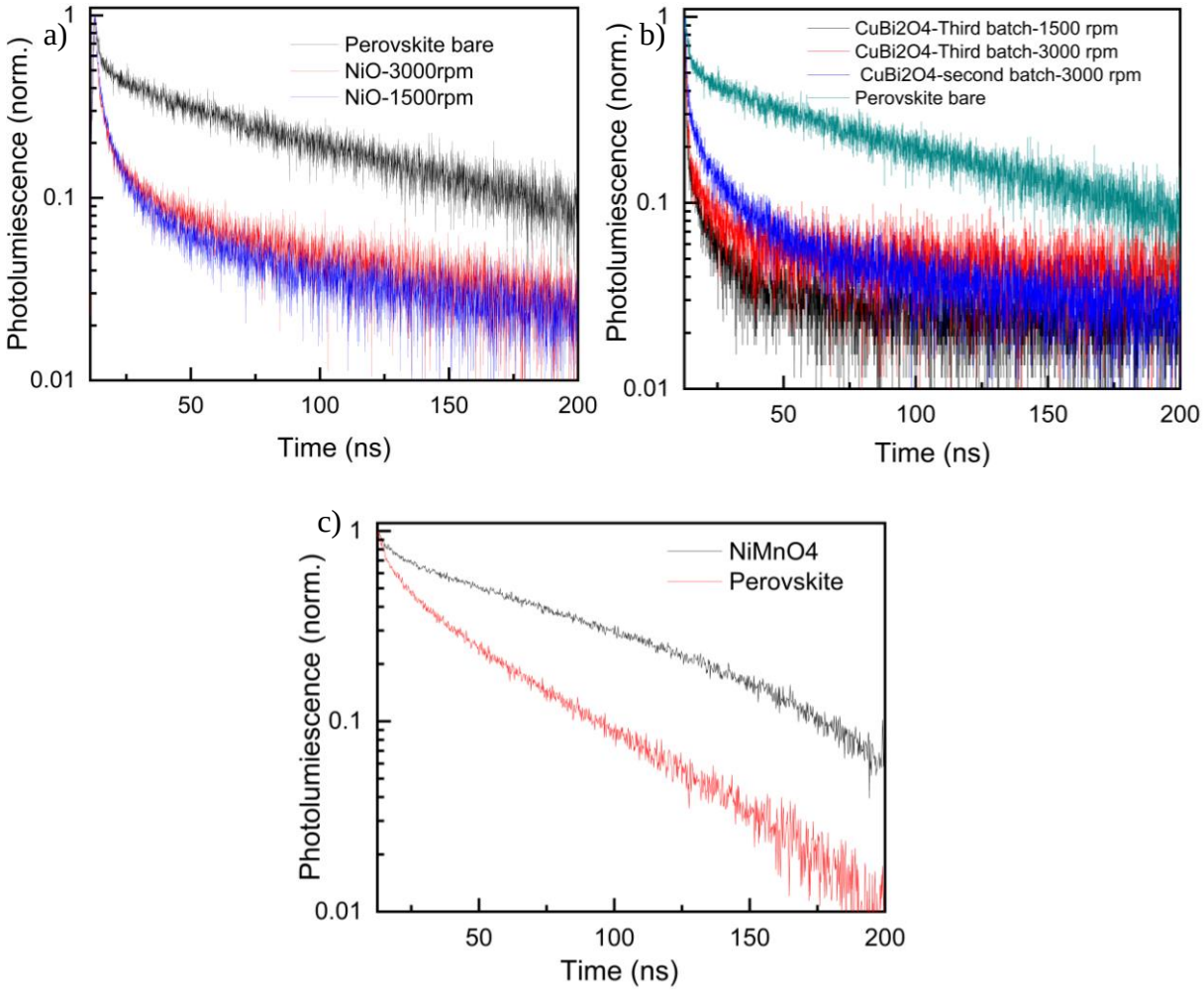

Figure 5.13. Time-resolved PL decay exited at 780 nm of a) perovskite bare film(black),and perovskite films coated with NiO 3000 rpm (red), and NiO 1500 rpm (blue), b) perovskite bare film(green),and perovskite films coated with $CuBi_2O_4$ -2 3000 rpm(purple),$CuBi_2O_4$ third batch 3000 rpm (red), and $CuBi_2O_4$-2 third batch 1500 rpm (black) and c) perovskite bare film (red),and perovskite films coated with $NiMnO_4$ (black).

Table 5.7. The time life fitting for perovskite, NiO and $CuBi_2O_4$ at different speed.

Materials	**Decay/ns**	**Standard deviation/ns**
Perovskite	2.1	0.1
	81.1	1.6
NiO -1500 rmp	2.1	0.03
	37.9	0.64
NiO -3000 rmp	2.6	0.03
	32.4	0.5
$CuBi_2O_4$-3C-1500 rpm	0.50	0.01
	11.5	0.3
$CuBi_2O_4$-3C-3000 rpm	0.9	0.02
	18.3	0.7
$CuBi_2O_4$-2C-3000 rpm	1.25	0.03
	24.02	0.34

Table 5.8. The time life fitting for perovskite and $NiMnO_4$.

Materials	Decay/ns	Standard deviation/ns
Perovskite	7.5	0.22789
	50.7	0.55
$NiMnO_4$	6.6	0.3
	129.2	2.05

5.4 Device Characterisation

The performance of $CuBi_2O_4$ and $NiMnO_4$ materials in perovskite solar cells was thoroughly evaluated through the fabrication of solar cells using a configuration similar to the one reported by Chen, *et al.* [21]. The p-type deposition parameters were optimised using $MAPbI_3$, and a state-of-the-art perovskite composition consisting of a mixture of halides and cations was utilised. This composition has demonstrated superior performance compared to $MAPbI_3$ in solar cell applications [21]. The inverted configuration device, as depicted in Figure 5.14 a), b) and c), was adopted for the fabrication process. The solar cell devices were characterised by measuring the current density-voltage (J-V) curve under the standard AM1.5 spectrum and one sun illumination (100 mW cm^{-2}). These characterization measurements provided valuable insights into the performance of $CuBi_2O_4$ and $NiMnO_4$ materials in the context of perovskite solar cells.

Theoretically, wide-band gap materials, such as NiO, possess lower conductivity compared to $CuBi_2O_4$. This characteristic holds the potential to decrease recombination rates at the HTM side, thereby enhancing charge collection efficiency and increasing the open-circuit voltage. To investigate this, different p-type NiO materials were used in the fabrication process, including commercial NiO, NiO-sol gel, and NiO from a reactor. It is worth noting that the conductivity of NiO arises from intrinsic Ni vacancies. However, the intrinsic resistivity of NiO remains large, resulting in increased series resistance and restrictions on NiO thickness [22]. Moreover, the larger-scale defects formed by NiO may impact device performance[22].

Figure 5.14 presents the recorded J-V characteristics of the fabricated solar cells under simulated AM1.5G sunlight (100 mW cm^{-2}). A comparison of the J-V curves of the best-performing devices reveals the relative photovoltaic performance of solar cells employing $CuBi_2O_4$ and NiO as hole-transporting materials. Specifically, comparing the forward bias to the short-circuit J-V curves, we observe a small increase in the short-circuit current (J_{sc}) for the $CuBi_2O_4$ devices compared to the NiO devices. However, the fill factor (FF) and open-circuit voltage (V_{oc}) demonstrate even more significant improvements in the NiO devices, resulting in enhanced power conversion efficiency (PCE) for the NiO-based devices (6.40%) compared to those utilising $CuBi_2O_4$ as the HTM (2.13%). This difference in performance could be attributed to the distinct valence positions of the two materials[19]. The detailed parameters of the best-performing cells for each configuration are provided in Table 5.9.

Table 5.9. Photoelectrochemical characteristics of p-type metal oxides in inverted perovskite solar cells under AM1.5G simulated sun light.

HTM	J_{sc} (mA/cm^2)	V_{oc} (V)	FF (%)	PCE (%)
NiO	10.92	1.0	60	6.40
$CuBi_2O_4$	11.05	0.60	32	2.13
NiO-Reactor	10.8	0.76	35	3
NiO- sol gel	8.25	0.93	60	5.05
PEDOT:PSS	15.06	0.87	42	5.52

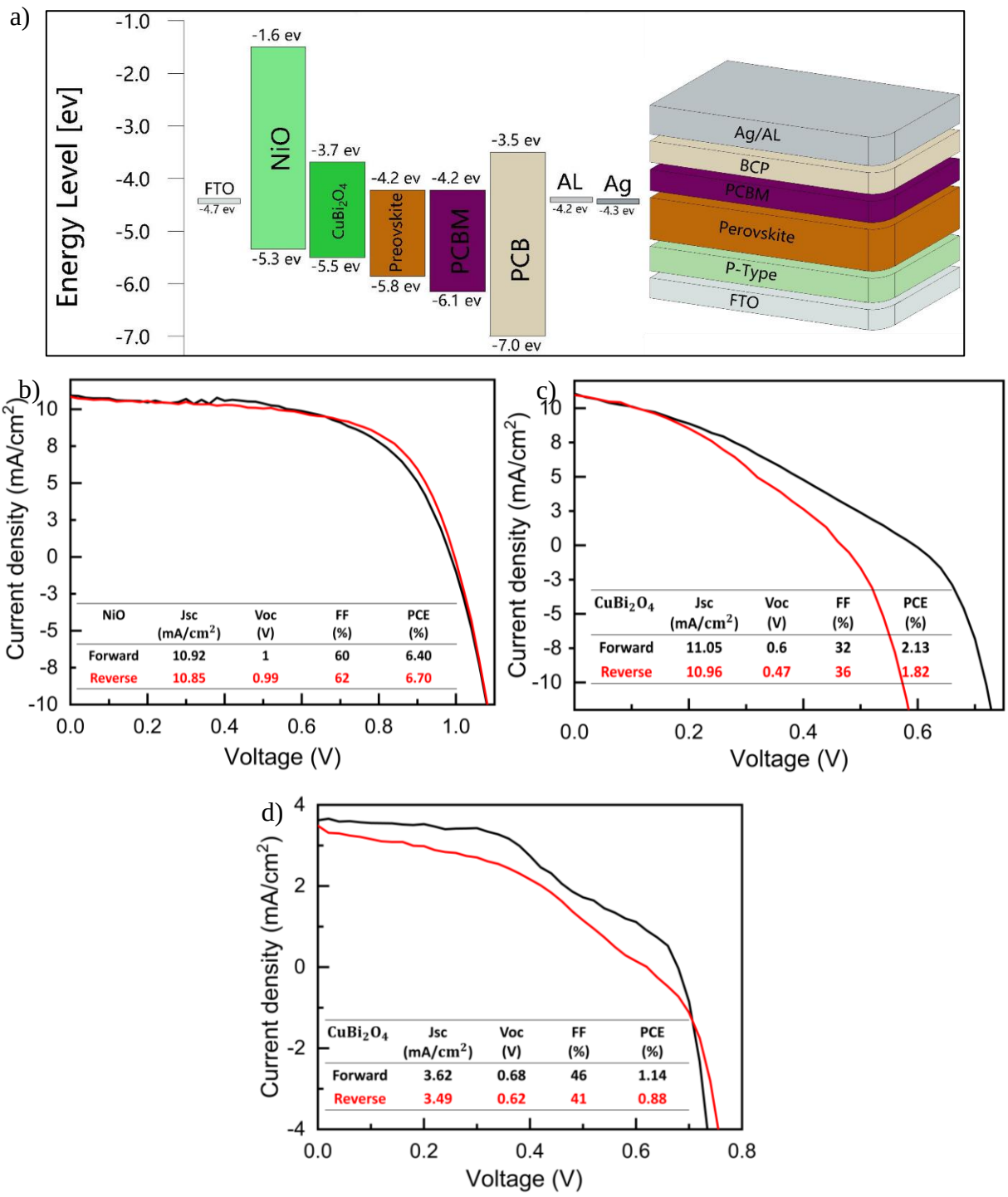

Figure 5.14. JV curves collected under AM1.5, 100 mW/cm^2 simulated sunlight of the champion device comprising : a) energy level diagram of NiO and $CuBi_2O_4$ with Perovskite and ETL, b) NiO in combination with FAMACs perovskite, c) $CuBi_2O_4$ in combination with FAMACs perovskite and d) $CuBi_2O_4$ in combination with MAPI perovskite.

5.5 Conclusions

In summary, this research aims to synthesise mixed metal oxides using a reactor on demand and vary the stoichiometry on a controlled way (including adding dopants). This is under development and successfully syntheses $CuBi_2O_4$, $NiMnO_4$ and NiO is a test case. Moreover, $CuBi_2O_4$ has low toxic property, an eco-friendly high reusability performance. A comparative analysis was undertaken to assess the performance of perovskite solar cells incorporating $CuBi_2O_4$ as (HTM) in comparison to devices utilising the inorganic HTM, NiO. The deposition of a relatively smooth $CuBi_2O_4$ film was accomplished via spin coating, resulting in a power conversion efficiency (PCE) of 2.13% for the solar cell operating in an inverted p-i-n structure. To optimise the performance of $CuBi_2O_4$ and ensure the formation of a continuous and uniform film, a series of treatments were implemented. These treatments encompassed ball milling with diverse ball sizes under both wet and dry conditions, ultrasonic treatment, and powder annealing at an appropriate temperature. The efficacy of these treatments was evaluated through the examination of XRD patterns, SEM images, and UV-vis spectroscopy. As a consequence of these optimisation endeavours, a discernible enhancement in film quality was achieved, characterized by particle sizes ranging from 20 to 25 nm, thereby facilitating improved charge transfer within the solar cell architecture. The utilisation of $CuBi_2O_4$ as an alternative HTM in perovskite solar cells exemplifies its prospective applicability in photovoltaic devices. It is important to note that the attained PCE of 2.13%, while comparatively modest when compared to conventional photovoltaic technologies, accentuates the significance of exploring novel HTMs to augment the overall performance of perovskite solar cells. Continued investigation and optimisation endeavours are imperative to heighten the efficiency of $CuBi_2O_4$-based solar cells, propelling their viability in the field of photovoltaics.

5.6 Experimental Section

5.6.1 Synthesis

All reagents were analytical. Bismuth acetate tetrahydrate ($Bi(CH_3COO)_2.0H_2O$,+99%), Bismuth(III) nitrate hydrate ($Bi(NO_3)_3.5H_2O$,+99%), Copper(II) acetate tetrahydrate ($Cu(CO_2CH_3)_2$, +99 %), Copper(II) nitrate trihydrate ($Cu(NO_3)_2.3H_2O$, +99.5%), Manganese (II) acetate tetrahydrate (Mn $(CH_3COO)_2$ $4H_2O$, +99 %), Nickel (II) acetate tetrahydrate (Ni-(CH_3COO) $2.4H_2O$, 99%), sodium hydroxide (NaOH, ≥99%) purchased from Sigma-Aldrich. Absolute ethanol (dehydrated) (C_2H_5OH).

$NiMn(OH)_4$ solution was prepared by dissolving 0.2 M of nickel (II) acetate tetrahydrate (Ni-(CH3COO)2·4H2O, 98%) in 500 mL of deionized water, 0.2 M of manganese (II) acetate tetrahydrate (Mn(CH3COO)2·4H2O, +99%) in 500 mL of DI water, and 0.4 M of sodium hydroxide (NaOH) in 500 mL of DI-water. The pH of the resulting mixture was 11 here. Subsequently, the resulting solution was transferred into a Teflon-lined stainless-steel autoclave with a volume of 100 mL. The autoclave was then placed in an oven and heated at 110°C for 18 hours. After the heating process, the product obtained was collected, washed multiple times with deionized water, and then dried under vacuum conditions over the weekend.

$CuBi_2(OH)_4$ solution was synthesized by combining copper salt, bismuth salt, and sodium hydroxide (NaOH) base, as detailed Table 5.10Table 5.10, which specifies the concentrations and types of salts used. To dissolve bismuth, it was added to 50 mL of a 0.5 M nitric acid solution, as it is insoluble in water. The mixture was then stirred for one hour. The resulting solution, characterized by a pH of approximately 10 for all batches (as depicted in Figure 5.15), was subsequently transferred to a Teflon-lined stainless-steel autoclave with a volume of 100 mL. The autoclave was placed in an oven and subjected to heating at 110°C for 18 hours. Following the heating process, the resulting product was collected, subjected to several washes with deionized water (DI-water), and subsequently dried under vacuum conditions over the weekend.

$Ni(OH)_2$ solution was prepared by dissolving 12.6 mmol of nickel (II) acetate tetrahydrate (Ni-(CH3COO)2·4H2O, 99%) in 75 mL of DI-water, and 27 mmol of sodium hydroxide (NaOH) in 100 mL of DI-water. The pH of the resulting mixture was 10 here. Subsequently, the resulting solution was transferred into a Teflon-lined stainless-steel autoclave with a volume of 100 mL. The autoclave was then placed in an oven and heated at 110°C for 18 hours. After the heating process, the product obtained was collected, washed multiple times with deionized water, and then dried under vacuum conditions over the weekend.

NiO sol-gel solution was prepared by dissolving 1 g of $NiCl_2$ and 1 g of (F108) in 6 mL of ethanol and 5 mL of pure deionized water. The resulting mixture was stirred continuously overnight. Subsequently, the solution was left to undergo an ageing process for a duration of one to two weeks before utilisation.

Table 5.10. Flow rate and concentration for bismuth and copper salt for each batch.

Batch	Bismuth Salt			Copper Salt			NaOH	
	Type of salt	Flow rate ($ml\ min^{-1}$)	Concentration (M)	Type of salt	Flow rate ($ml\ min^{-1}$)	Concentration (M)	Flow rate ($ml\ min^{-1}$)	Concentration (M)
B1-1	$Bi(CH_3COO)_2.0H_2O$	1.250	0.05	$Cu(CO_2CH_3)_2$	1.250	0.025	2.5	0.264
B1-2		1.250	0.05		0.250	0.025	2.5	0.264
B2-1		1.333	0.2	$Cu(NO_3)_2.3H_2O$	0.667	0.1	2.5	0.314
B3-1	$Bi(NO_3)_3.5H_2O$	1.333	0.1		0.667	0.1	2	0.68
B3-2		1.667	0.1		0.833	0.1	2.5	0.68
B4-1		1.667	0.1		0.8883	0.1	2.5	0.68
B4-2		1.667	0.1		0.833	0.1	2.5	0.68
B5-1		1.667	0.1		0.8883	0.1	2.55	0.2406
B5-2		1.667	0.1		0.8883	0.1	2.55	0.2406
B5-3		1.667	0.1		0.8883	0.1	2.55	0.2406

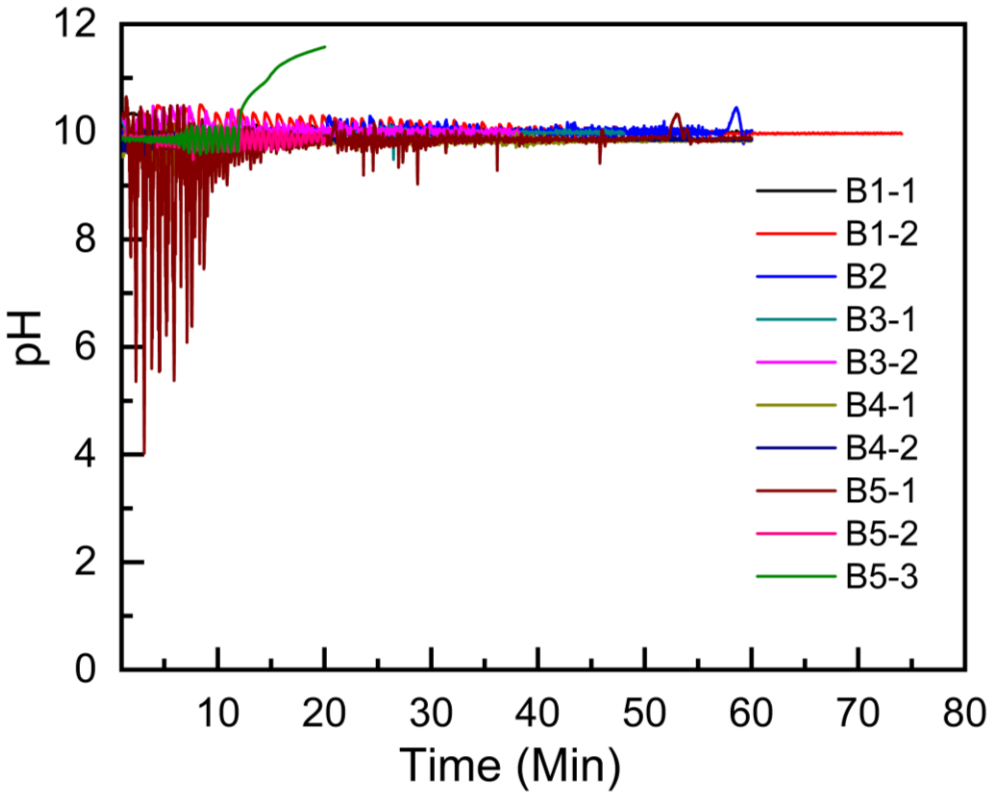

Figure 5.15. pH stability of $CuBi_2(OH)_4$ for different batch.

5.6.2 General Characterisation Techniques

The X-ray diffraction (XRD) pattern analysis was performed to investigate the structural properties and phase transitions of (Ni O H), Cu Bi OH, and (Ni Mn OH) powders using a PANanalytical Diffractometer. The diffractometer employed a Cu K-Alpha radiation source with a wavelength of 1.54 Å and was operated at 40 kV and 40 mA. To prepare the samples for analysis, a slurry of each powder in ethanol was meticulously prepared to ensure homogeneity. The resulting slurry was then carefully deposited onto a silicon zero diffraction plate, allowing for the formation of a thin and uniform layer. By utilising the variable temperature capability of the diffractometer, XRD measurements were conducted at different temperatures to capture the thermal behaviour and phase transitions of the powders. The collected data, represented by Figure 5 for (Ni O H), Figure 5 for Cu Bi OH, and Figure 5 for (Ni Mn OH), were subsequently subjected to analysis using the PANanalytical X'Pert Highscore software. This software facilitated the interpretation of the

diffraction patterns and enabled the extraction of valuable information about the crystal structures, identification of phases, determination of lattice parameters, and analysis of thermal effects on the crystalline structures. By combining the experimental measurements and data analysis, a comprehensive understanding of the structural properties and thermal behaviour of the (Ni O H), Cu Bi OH, and (Ni Mn OH) powders was obtained.

5.7 References

[1] N. Renewable, E. Laboratory, Best Research-Cell Efficiency Chart, 2023.

[2] A.S.R. Bati, Y.L. Zhong, P.L. Burn, M.K. Nazeeruddin, P.E. Shaw, M. Batmunkh, Next-generation applications for integrated perovskite solar cells, Communications Materials 4(1) (2023) 2. https://doi.org/10.1038/s43246-022-00325-4.

[3] Y. Wang, I. Ahmad, T. Leung, J. Lin, W. Chen, F. Liu, A. Man, C. Ng, Y. Zhang, A.B. Djurišš, Encapsulation and Stability Testing of Perovskite Solar Cells for Real Life Applications, (2022). https://doi.org/10.1021/acsmaterialsau.1c00045.

[4] T. Ahmed Chowdhury, M. Arafat Bin Zafar, M. Sajjad-Ul Islam, M. Shahinuzzaman, M. Aminul Islam, M. Uddin Khandaker, Stability of perovskite solar cells: issues and prospects, (2023). https://doi.org/10.1039/d2ra05903g.

[5] Q. Wang, Z. Lin, J. Su, Z. Hu, J. Chang, Y. Hao, Recent progress of inorganic hole transport materials for efficient and stable perovskite solar cells, Nano Select 2(6) (2021) 1055-1080. https://doi.org/10.1002/nano.202000238.

[6] L. Nakka, Y. Cheng, A.G. Aberle, F. Lin, Analytical Review of Spiro-OMeTAD Hole Transport Materials: Paths Toward Stable and Efficient Perovskite Solar Cells, (2022). https://doi.org/10.1002/aesr.202200045.

[7] S. Li, Y.-L. Cao, W.-H. Li, Z.-S. Bo, A brief review of hole transporting materials commonly used in perovskite solar cells, (2009). https://doi.org/10.1007/s12598-020-01691-z.

[8] E. Kasparavicius, M. Franckevič, V. Malinauskiene, K. Genevič, V. Getautis, T. Malinauskas, Oxidized Spiro-OMeTAD: Investigation of Stability in Contact with Various Perovskite Compositions, (2021). https://doi.org/10.1021/acsaem.1c02375.

[9] N. Aida, N. Ouedraogo, G.O. Odunmbaku, B. Guo, S. Chen, X. Lin, T. Shumilova, K. Sun, Oxidation of Spiro-OMeTAD in High-Efficiency Perovskite Solar Cells, Cite This: ACS Appl. Mater. Interfaces 14 (2022) 34303-34327. https://doi.org/10.1021/acsami.2c06163.

[10] W. Han, G. Ren, J. Liu, Z. Li, H. Bao, C. Liu, W. Guo, Recent Progress of Inverted Perovskite Solar Cells with a Modified PEDOT:PSS Hole Transport Layer, Cite This: ACS Appl. Mater. Interfaces 12 (2020) 49322-49322. https://doi.org/10.1021/acsami.0c13576.

[11] H. Pang, J. Deng, S. Wang, S. Li, J. Du, J. Chen, J. Zhang, Facile synthesis of porous nickel manganite materials and their morphology effect on electrochemical properties, RSC Advances 2(14) (2012) 5930-5934. https://doi.org/10.1039/C2RA20245J.

[12] W. Kang, Y. Tang, W. Li, X. Yang, H. Xue, Q. Yang, C.S. Lee, High interfacial storage capability of porous NiMn2O4/C hierarchical tremella-like nanostructures as the lithium ion battery anode, Nanoscale 7(1) (2014) 225-231. https://doi.org/10.1039/C4NR04031G.

[13] A.C. Garcia, A. Diaz Herrera, E.A. Ticianelli, M. Chatenet, C. Poinsignon, Evaluation of Several Carbon-Supported Nanostructured Ni-Doped Manganese Oxide Materials for the Electrochemical Reduction of Oxygen, Journal of The Electrochemical Society 158 (2011) 290-296. https://doi.org/10.1149/1.3528439.

[14] P.W. Menezes, A. Indra, O. Levy, K. Kailasam, V. Gutkin, J. Pfrommer, M. Driess, Using nickel manganese oxide catalysts for efficient water oxidation, Chemical Communications 51(24) (2015) 5005-5008. https://doi.org/10.1039/C4CC09671A.

[15] D. Kang, J.C. Hill, Y. Park, K.S. Choi, Photoelectrochemical Properties and Photostabilities of High Surface Area CuBi2O4 and Ag-Doped CuBi2O4 Photocathodes, Chemistry of Materials 28(12) (2016) 4331-4340. https://doi.org/10.1021/ACS.CHEMMATER.6B01294/ASSET/IMAGES/LARGE/CM-2016-01294A_0008.JPEG.

[16] M.A. Peck, M.A. Langell, Comparison of nanoscaled and bulk NiO structural and environmental characteristics by XRD, XAFS, and XPS, Chemistry of Materials 24(23) (2012) 4483-4490. https://doi.org/10.1021/CM300739Y/SUPPL_FILE/CM300739Y_SI_004.PDF.

[17] J. Moavi, F. Buazar, M.H. Sayahi, Algal magnetic nickel oxide nanocatalyst in accelerated synthesis of pyridopyrimidine derivatives, Scientific Reports 2021 11:1 11(1) (2021) 1-14. https://doi.org/10.1038/s41598-021-85832-z.

[18] J. Lee, H. Yoon, K. Soon Choi, S. Kim, S. Seo, J. Song, B.-U. Choi, J. Ryu, S. Ryu, J. Oh, C. Jeon, S. Lee, J. Lee, H. Yoon, S. Kim, S. Seo, J. Song, S. Lee, K.S. Choi, B.u. Choi, J. Oh, J. Ryu, S. Ryu, C. Jeon, Template Engineering of CuBi2O4 Single-Crystal Thin Film Photocathodes, Small 16(39) (2020) 2002429-2002429. https://doi.org/10.1002/SMLL.202002429.

[19] F.E. Oropeza, N.Y. Dzade, A. Pons-Martí, Z. Yang, K.H.L. Zhang, N.H. De Leeuw, E.J.M. Hensen, J.P. Hofmann, Electronic Structure and Interface Energetics of CuBi2O4Photoelectrodes, Journal of Physical Chemistry C 124(41) (2020) 22416-22425. https://doi.org/10.1021/ACS.JPCC.0C08455/ASSET/IMAGES/LARGE/JP0C08455_0006.JPEG.

[20] A.A. Barzinjy, S.M. Hamad, S. Aydın, M.H. Ahmed, F.H.S. Hussain, Green and eco-friendly synthesis of Nickel oxide nanoparticles and its photocatalytic activity for methyl orange degradation, Journal of Materials Science: Materials in Electronics 31(14) (2020) 11303-11316. https://doi.org/10.1007/S10854-020-03679-Y/FIGURES/15.

[21] C. Chen, S. Zhang, S. Wu, W. Zhang, H. Zhu, Z. Xiong, Y. Zhang, W. Chen, Effect of BCP buffer layer on eliminating charge accumulation for high performance of inverted perovskite solar cells, RSC Advances 7(57) (2017) 35819-35826. https://doi.org/10.1039/C7RA06365B.

[22] X. Lin, D. Cui, X. Luo, C. Zhang, Q. Han, Y. Wang, L. Han, Efficiency progress of inverted perovskite solar cells, Energy & Environmental Science 13(11) (2020) 3823-3847. https://doi.org/10.1039/D0EE02017F.

Chapter 6. Conclusions

This thesis has been dedicated to investigating innovative materials that facilitate the transportation of holes (positive charges) in perovskite solar cells (PSCs) with the objective of enhancing the efficiency of converting sunlight into electricity. The primary focus of this research encompasses a comprehensive examination of three distinct hole-transporting materials (HTMs): TPABT, $CuBi_2O_4$, and NiMnO4. While $CuBi_2O_4$ and $NiMnO_4$ have been previously employed as p-type semiconductors in device applications such as dye-sensitized solar cells (DSSCs), their complete utilisation in PSCs has not been thoroughly explored. Consequently, the thesis pursued device optimisation by modifying various parameters associated with the HTMs, depositing different types of perovskite materials, and conducting charge extraction and transport analyses.

In Chapter 4, a novel and cost-effective hole transporting material (HTM), TPABT, was designed and synthesised, surpassing the performance of the previous generation material, EDOT-Amide-TPA. TPABT exhibited desirable properties such as molecular assembly, high transparency, and excellent charge transport. The synthesis of TPABT involved a simple condensation chemistry method, resulting in an extremely low-cost material compared to the expensive and complex synthesis of Spiro-OMeTAD, which is commonly used as an HTM. Cyclic voltammetry and DFT calculations revealed a favorable alignment between the highest occupied molecular orbital (HOMO) level of TPABT and the valence band of perovskite, indicating hole-selectivity and suggesting its potential for high performance in solar cell devices. Conductivity measurements demonstrated a significant increase in conductivity, up to 4.71×10^{-4} S cm^{-1}, with the addition of LiTFSI as an oxidant, surpassing Spiro-OMeTAD under similar conditions. Hole mobility measurements of TPABT exhibited a mobility increase up to 10^{-4} cm^2 $V^{-1}s^{-1}$ with the addition of Li-TFSI. Implementing TPABT as an HTM in solar cell devices resulted in a respectable efficiency of approximately 15%, with a V_{oc} of 1.11V and a J_{sc} of 22.59 mA cm^{-2}. Ongoing investigations are exploring the performance of TPABT derivatives, as it is relatively easy to modify the core and tune the TPA units to enhance film characteristics, conductivity, and transparency. These advancements hold the potential for further improvements in solar cell efficiency.

Chapter 5 focused on the synthesis of mixed metal oxides using a reactor-on-demand system, allowing for controlled variation of stoichiometry and the addition of dopants. The successful

synthesis of $CuBi_2O_4$, $NiMnO_4$, and NiO was achieved as a test case. $CuBi_2O_4$ was particularly highlighted for its favourable characteristics, including low toxicity, eco-friendly reusability, wide bandgap, high transparency, and solution-processability at low temperatures. It is readily available from commercial sources at a low cost. A comparative analysis was conducted to evaluate the performance of perovskite solar cells incorporating $CuBi_2O_4$ as the hole transport material (HTM) in comparison to devices utilising the inorganic HTM, NiO. A relatively smooth $CuBi_2O_4$ film was successfully deposited via spin coating, resulting in a power conversion efficiency (PCE) of 2.13% for the solar cell operating in an inverted p-i-n structure.

To optimise the performance of $CuBi_2O_4$, several treatments were implemented to ensure the formation of a continuous and uniform film. These treatments included ball milling with various ball sizes under both wet and dry conditions, ultrasonic treatment, and powder annealing at an appropriate temperature. The effectiveness of these treatments was evaluated through the analysis of XRD patterns, SEM images, and UV-vis spectroscopy. As a result of these optimisation efforts, an improvement in film quality was achieved, characterised by particle sizes ranging from 20 to 25 nm, facilitating enhanced charge transfer within the solar cell architecture.

The successful utilisation of $CuBi_2O_4$ as an alternative hole transport material (HTM) in perovskite solar cells demonstrates its potential applicability in photovoltaic devices. Despite achieving a modest power conversion efficiency (PCE) of 2.13%, continued investigation and optimisation efforts are of utmost importance to further enhance the efficiency of $CuBi_2O_4$-based perovskite solar cells, ultimately advancing their viability in the field of photovoltaics. Ongoing investigations are currently exploring the performance of $CuBi_2O_4$ with the addition of dopants, such as Ag, aiming to improve film characteristics, conductivity, and transparency. These ongoing advancements hold significant potential for further improvements in solar cell efficiency and signify the importance of pursuing novel strategies to push the boundaries of perovskite-based photovoltaic technologies.

In conclusion, this thesis has provided significant investigations into a novel, cost-effective, and stable hole transporting material (HTM) aimed at achieving efficient PCEs in perovskite solar cells. The significance of further characterisations, particularly dark current characteristics, ultraviolet photoelectron spectroscopy (UPS) and Mott-Schottky measurement before and after doping, are

underscored. While the dark current characteristics is crucial benchmark for understanding HTM behaviour in the absence of light, providing pivotal insights for optimising performance in illuminated conditions, the UPS and Mott-Schottky measurements offer nuanced insights into electronic structure and doping effects. |In addition, charge transfer experiments such as conductivity and mobility measurements shall be explored. Further research endeavours can be directed towards the application of the developed techniques to novel perovskite materials exhibiting higher efficiency and enhanced thermal stability. These innovative HTMs can also be employed in future tandem device fabrication, serving as either HTMs or interlayers, thereby expanding their potential applications and contributing to advancements in photovoltaic technologies.

Appendices

Characterisation of TPABT

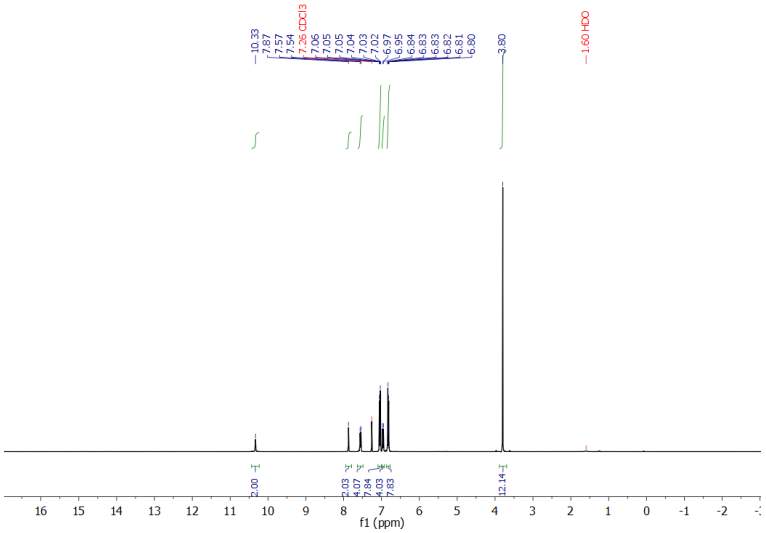

Figure A. 1. ^{1}H NMR spectrum recorded at room temperature of TPABT in CDCl3.

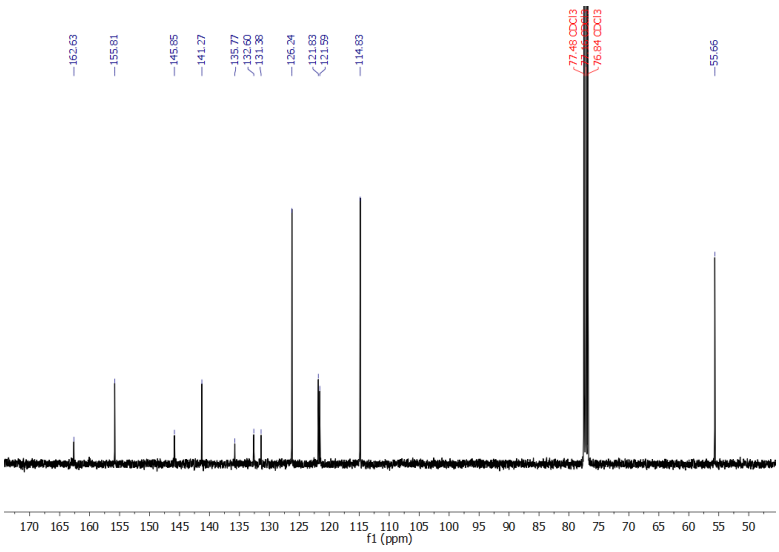

Figure A. 2. ^{13}C NMR spectrum recorded at R.T. of TPABT in CDCl3.

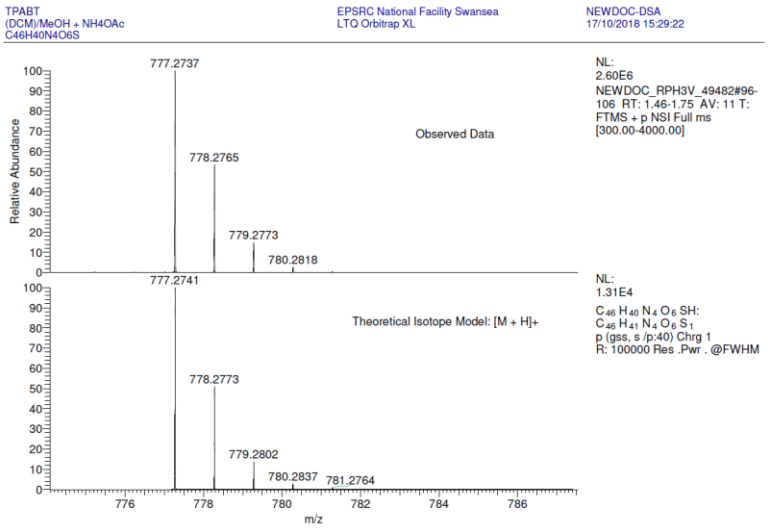

Figure A. 3. Observed and theoretical HRMS for $[M+H]^{\cdot}$ cation of TPABT.

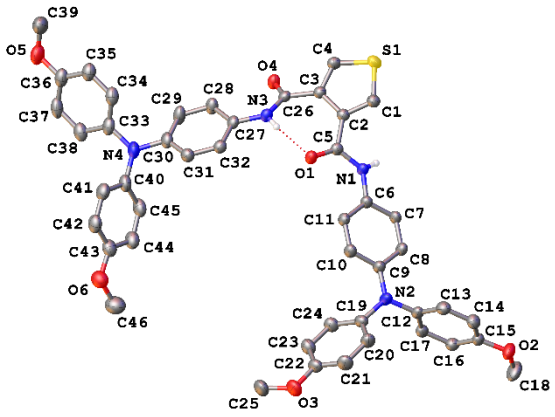

Table A. 1. Crystal data and structure refinement for the CB solvate of TPABT.

Identification code	TPABT-CB
Empirical formula	$C_{58}H_{50}Cl_2N_4O_6S$
Formula weight	1001.98
Temperature/K	150.0(2)
Crystal system	monoclinic
Space group	$P2_1/c$
a/Å	12.1297(3)
b/Å	14.8832(3)

c/Å	27.8998(7)
α/°	90
β/°	96.293(2)
γ/°	90
Volume/Å^3	5006.38(19)
Z	4
ρ_{calc}g/cm^3	1.329
μ/mm^{-1}	2.014
F(000)	2096.0
Crystal size/mm^3	0.22 × 0.05 × 0.05
Radiation	CuKα (λ = 1.54184)
2Θ range for data collection/°	7.332 to 133.852
Index ranges	-14 ≤ h ≤ 14, -17 ≤ k ≤ 11, -33 ≤ l ≤ 32
Reflections collected	36302
Independent reflections	8876 [R_{int} = 0.0653, R_{sigma} = 0.0490]
Data/restraints/parameters	8876/0/650
Goodness-of-fit on F^2	1.012
Final R indexes [I>=2σ (I)]	R_1 = 0.0527, wR_2 = 0.1327
Final R indexes [all data]	R_1 = 0.0809, wR_2 = 0.1522
Largest diff. peak/hole / e Å^{-3}	0.57/-0.57

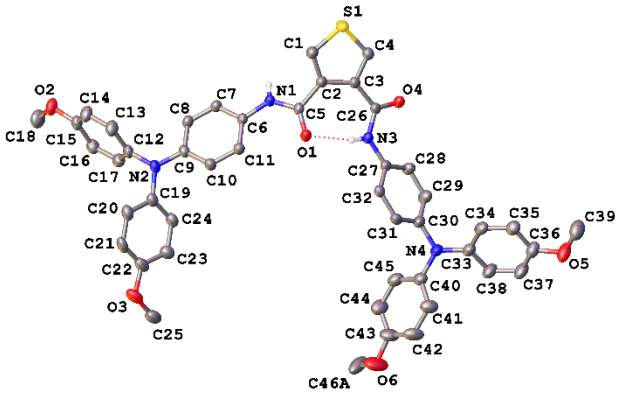

Table A. 2. Crystal data and structure refinement for the $CHCl_3$ solvate of TPABT.

Identification code	TPABT-$CHCl_3$
Empirical formula	$C_{47}H_{41}Cl_3N_4O_6S$
Formula weight	896.25
Temperature/K	150.0(2)
Crystal system	triclinic
Space group	P-1
a/Å	11.2176(3)
b/Å	15.2072(3)
c/Å	26.5071(6)
α/°	76.7998(19)
β/°	86.521(2)
γ/°	89.1071(19)
Volume/Å^3	4394.19(18)
Z	4
ρ_{calc}g/cm^3	1.355
μ/mm^{-1}	2.773

F(000)	1864.0
Crystal size/mm^3	0.3 × 0.21 × 0.08
Radiation	CuKα (λ = 1.54184)
2Θ range for data collection/°	7.534 to 133.832
Index ranges	-13 ≤ h ≤ 13, -18 ≤ k ≤ 17, -31 ≤ l ≤ 31
Reflections collected	61973
Independent reflections	15552 [R_{int} = 0.0396, R_{sigma} = 0.0298]
Data/restraints/parameters	15552/1081/1165
Goodness-of-fit on F^2	1.023
Final R indexes [I>=2σ (I)]	R_1 = 0.0504, wR_2 = 0.1350
Final R indexes [all data]	R_1 = 0.0625, wR_2 = 0.1462
Largest diff. peak/hole / e Å^{-3}	0.57/-0.63

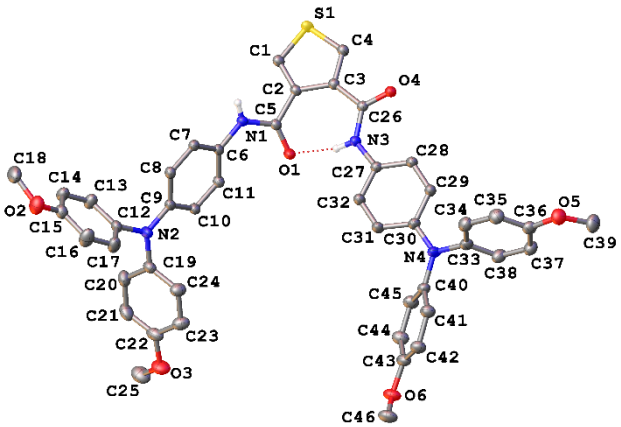

Table A. 3. Crystal data and structure refinement for the second polymorph of the $CHCl_3$ solvate of TPABT.

Identification code	TPABT2_$CHCl_3$
Empirical formula	$C_{47}H_{41}Cl_3N_4O_6S$
Formula weight	896.25
Temperature/K	100.0(2)
Crystal system	triclinic
Space group	P-1
a/Å	8.35220(10)
b/Å	14.70570(10)
c/Å	18.79250(10)
α/°	66.99
β/°	86.25
γ/°	88.95
Volume/Å^3	2119.93(3)
Z	2

ρ_{calc}g/cm^3	1.404
μ/mm^{-1}	0.301
F(000)	932.0
Crystal size/mm^3	0.236 × 0.049 × 0.023
Radiation	Synchrotron (λ = 0.6889)
2Θ range for data collection/°	2.286 to 55.48
Index ranges	-11 ≤ h ≤ 11, -19 ≤ k ≤ 19, -25 ≤ l ≤ 25
Reflections collected	32739
Independent reflections	10867 [R_{int} = 0.0675, R_{sigma} = 0.0687]
Data/restraints/parameters	10867/507/587
Goodness-of-fit on F^2	1.065
Final R indexes [I>=2σ (I)]	R_1 = 0.0557, wR_2 = 0.1708
Final R indexes [all data]	R_1 = 0.0613, wR_2 = 0.1767
Largest diff. peak/hole / e Å^{-3}	0.82/-0.80

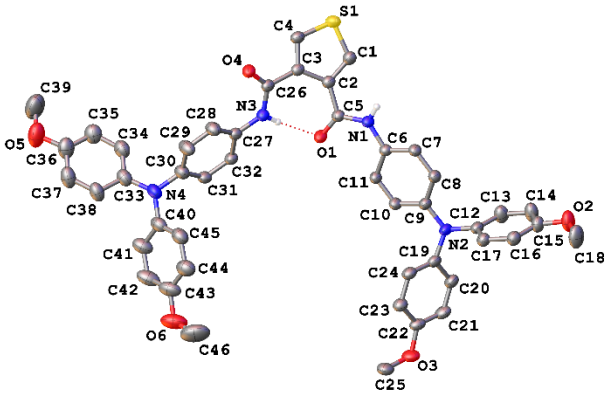

Table A. 4. Crystal data and structure refinement for the tetrahydrofuran (THF)solvate of TPABT.

Identification code	TPABT_THF
Empirical formula	$C_{108}H_{118}N_8O_{16}S_2$
Formula weight	1848.22
Temperature/K	150.0(2)
Crystal system	triclinic
Space group	P-1
a/Å	11.3945(2)
b/Å	15.1250(4)
c/Å	28.8132(7)
α/°	85.612(2)
β/°	81.4751(19)
γ/°	89.9926(18)
Volume/Å^3	4896.2(2)
Z	2
ρ_{calc}g/cm^3	1.254
μ/mm^{-1}	1.061
F(000)	1964.0
Crystal size/mm^3	0.27 × 0.21 × 0.07

Radiation	CuKα (λ = 1.54184)
2Θ range for data collection/°	7.846 to 133.802
Index ranges	$-13 \leq h \leq 13$, $-17 \leq k \leq 17$, $-34 \leq l \leq 32$
Reflections collected	68908
Independent reflections	17290 [R_{int} = 0.0488, R_{sigma} = 0.0375]
Data/restraints/parameters	17290/1527/1368
Goodness-of-fit on F^2	1.080
Final R indexes [I>=2σ (I)]	R_1 = 0.0773, wR_2 = 0.2073
Final R indexes [all data]	R_1 = 0.0929, wR_2 = 0.2176
Largest diff. peak/hole / e $Å^{-3}$	0.47/-0.41

Table A. 5. The cost and quantities of the materials used to synthesise TPABT.

Chemical name	Weight(g)	Price of chemical ($/kg)	Material cost ($/g product)
Thiophene-diCOOH(1)	0.28	3,120.00	0.8736
DMF	0.01	5.09	0.0000509
SOCL2	0.44	27.67	0.0121748
THF	20.9	9.24	0.0193116
TPA-NH2(3)	1.18	2,280.00	2.6904
Triethylamine	0.1	21.54	0.002154
THF	20.9	9.24	0.193116
EtOH	39.5	2.78	0.10981

MeOH	39.6	2.21	0.087516
Et2O	4.2	5.57	0.023394
Total			4.1853317

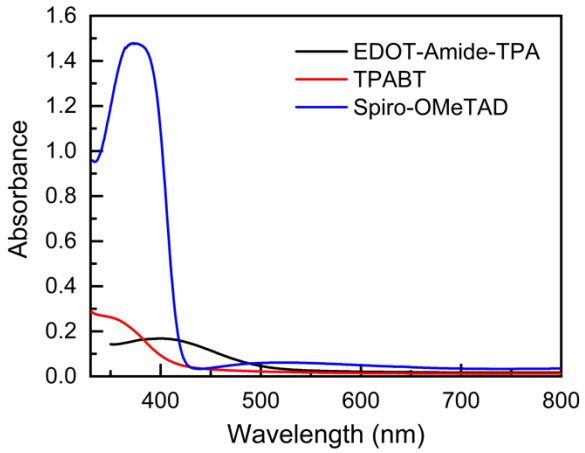

Figure A. 4. UV-vis absorption spectrum of TPABT (50 nm thickness), EDOT-Amide-TPA (45 nm), and Spiro-OMeTAD (200 nm) as thin film.

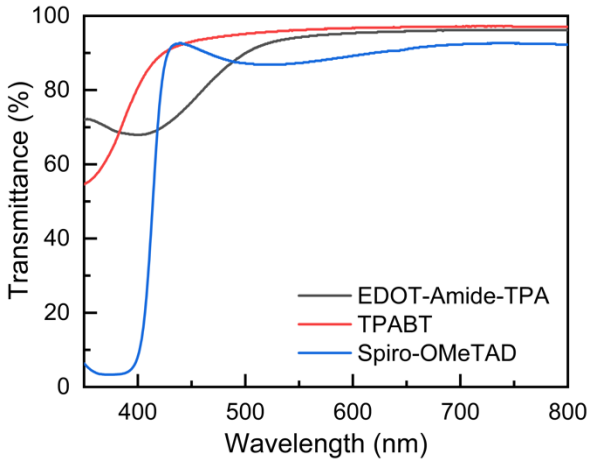

Figure A. 5. Transmittance of TPABT, EDOT-Amide-TPA, and Spiro-OMeTAD as thin film.

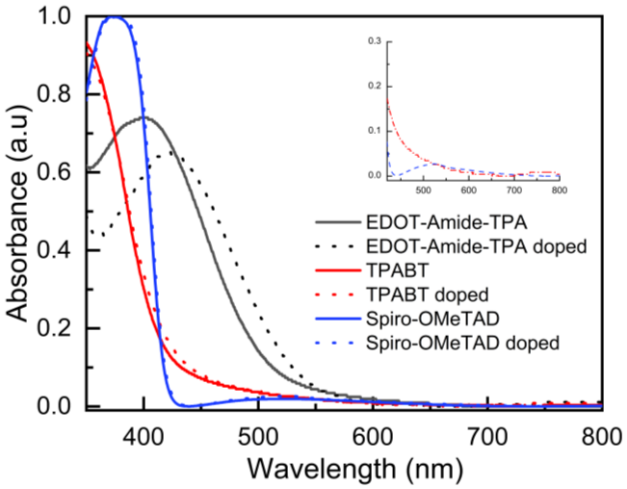

Figure A. 6. UV-vis absorption spectra of TPABT, EDOT-Amide-TPA, and Spiro-OMeTAD pristine and doped with Li-TFSI as a thin film.

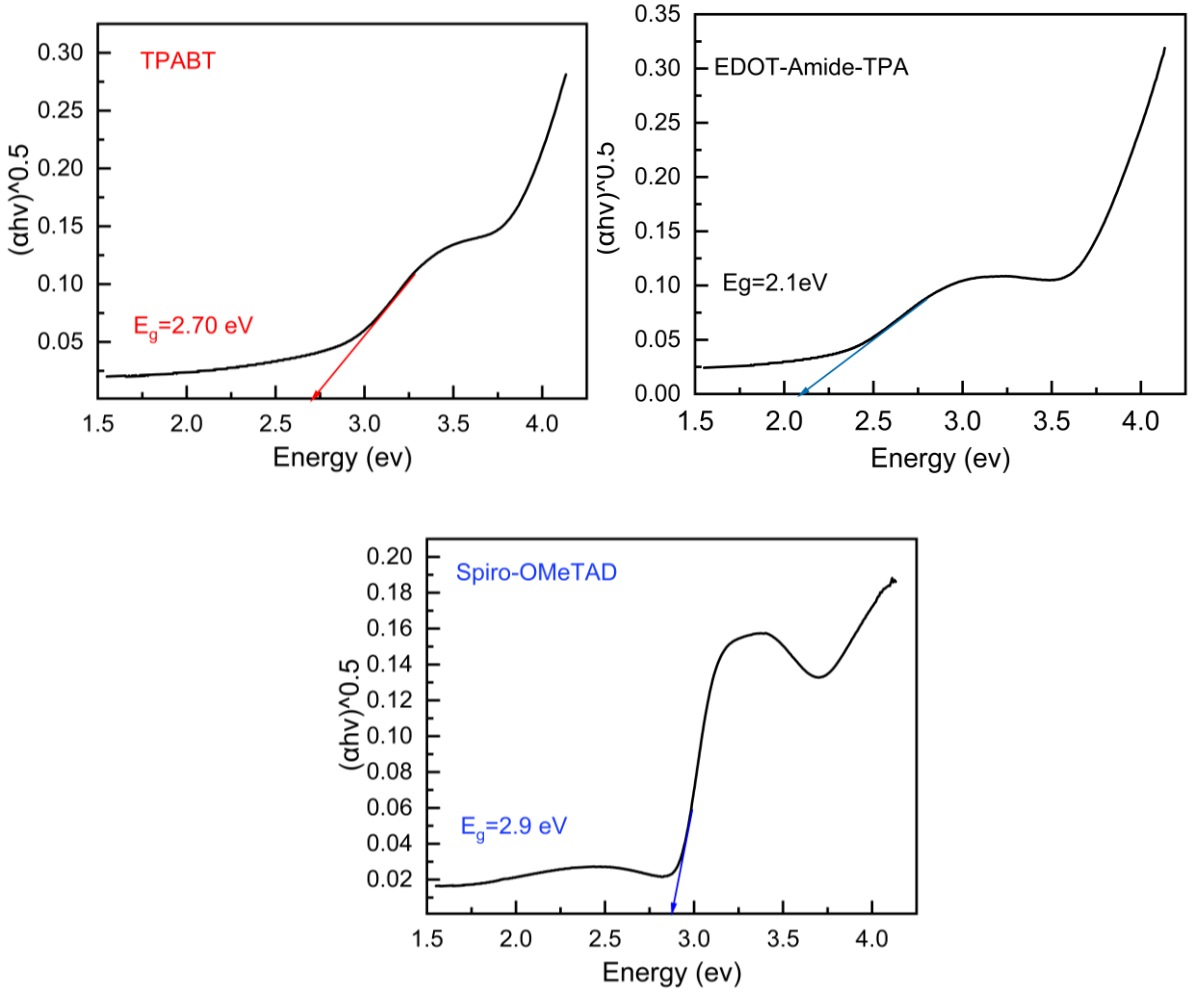

Figure A. 7. Band gap calculation of TPABT (50 nm thickness), EDOT-Amide-TPA (45 nm), and Spiro-OMeTAD (200 nm).

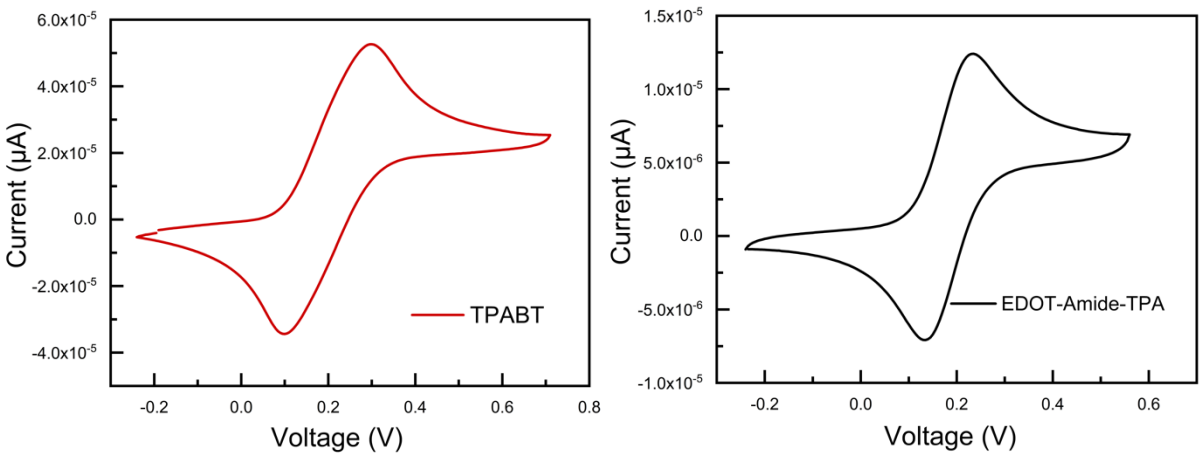

Figure A. 8. Cyclic voltammogram of TPABT and EDOT-Amide-TPA measured in anhydrous dichloromethane under N_2 with 0.1M tetrabutylammonium hexafluorophosphate $TBAPF_6$.

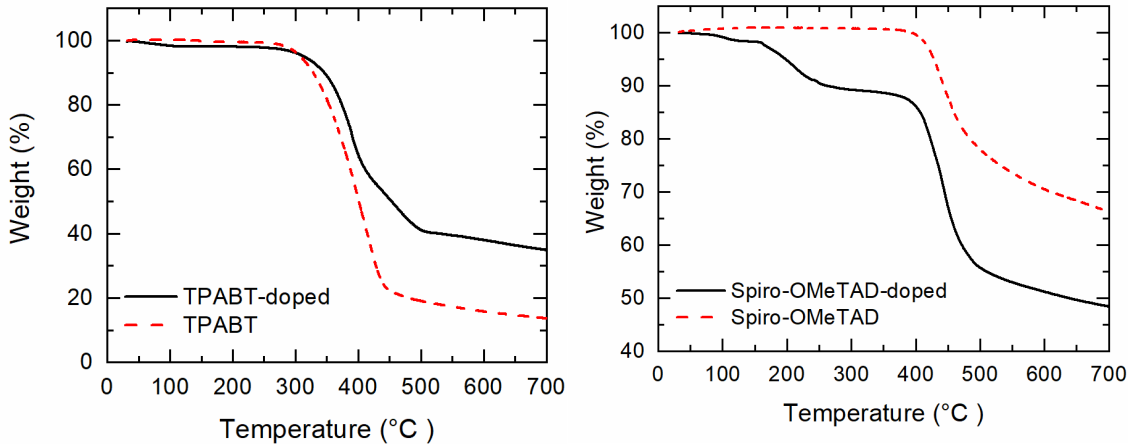

Figure A. 9. TGA thermograms of pristine and doped TPABT and Spiro-OMeTAD with a heating rate of 5 °C min^{-1} under nitrogen atmosphere.

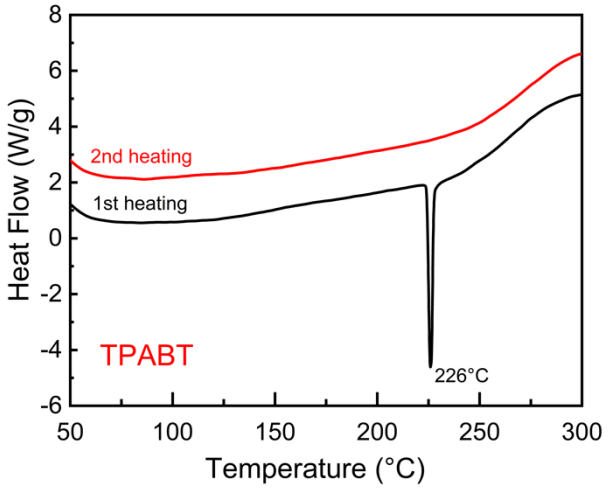

Figure A. 10. DSC first and second heating for TPABT, at the heating rate of 5° min^{-1}.

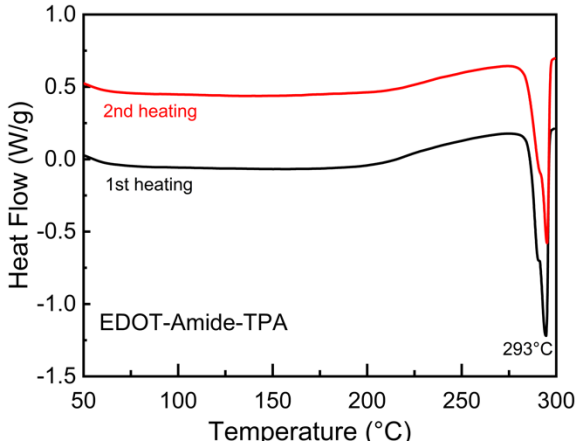

Figure A. 11. DSC first and second heating for EDOT-Amide-TPA, at the heating rate of 5° min^{-1}.

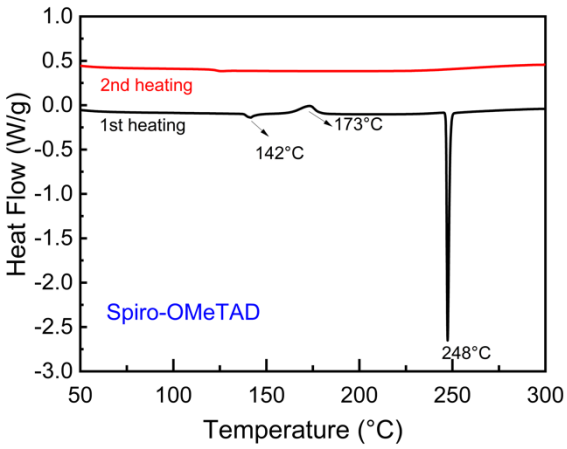

Figure A. 12. DSC first and second heating for Spiro-OMeTAD, at the heating rate of 5° min^{-1}.

Table A. 6. Comparison of the degradation, melting and glass transition temperature of EDOT-Amide, TPABT and Spiro-OMeTAD

HTL	T_m(°C)	T_d(°C)	T_g(°C)
Spiro-OMeTAD	248	408	142
EDOT-Amide-TPA	293	347	-
TPABT	226	300	-

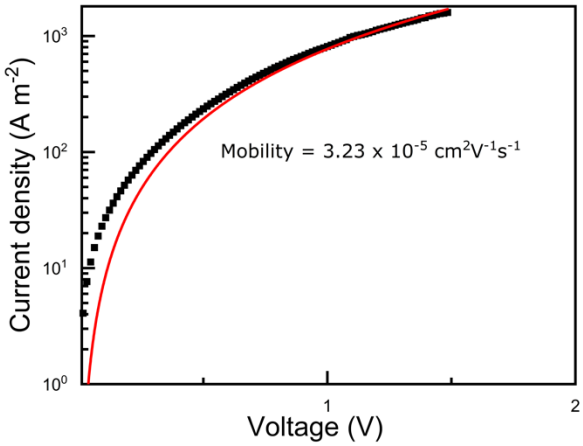

Figure A. 13. J-V measurements of hole only devices on a linear-log scale.

Table A. 7. Comparison of the mobility for Spiro-OMeTAD, EDOT-amide and TPABT, as pristine and with Li-TFSI doping

	TPABT	EDOT-Amide-TPA[3]	Spiro-OMeTAD[3]
Hole mobility ($cm^2\ V^{-1}\ s^{-1}$)	5.3×10^{-6}	3.9×10^{-5}	4×10^{-5}
Hole mobility doped ($cm^2\ V^{-1}\ s^{-1}$)	3.23×10^{-5}	2.1×10^{-4}	5.3×10^{-4}

Table A. 8. The experiment was done by using the XE-150 park system AFM to measure the thickness for TPABT, EDOT-Amide-TPA, and Spiro-OMeTAD at the same condition of solar cells.

Materials	TPABT	EDOT-Amide-TPA	Spiro-OMeTAD
Δy(nm)	50	45	200

TPABT

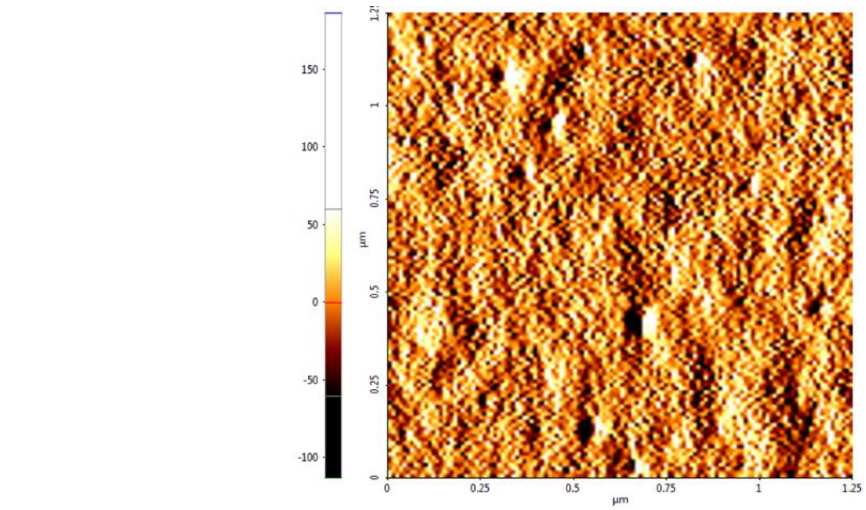

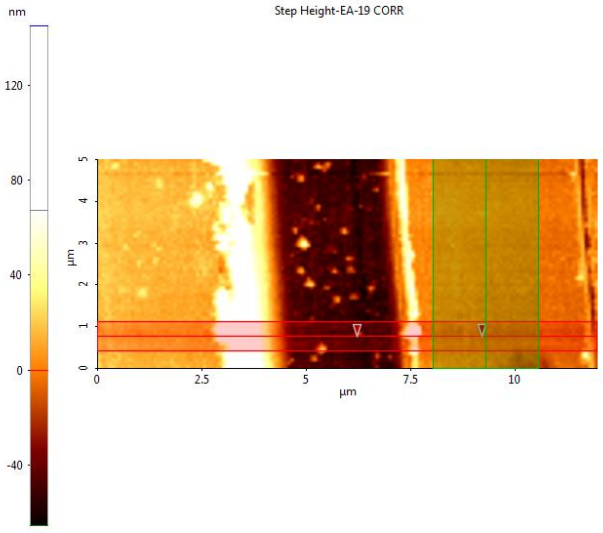

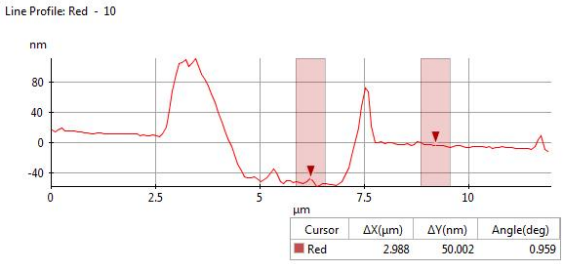

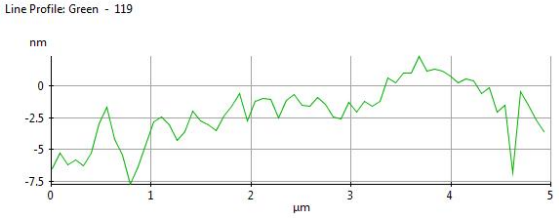

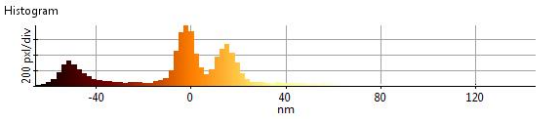

Statistics

Line	Min(nm)	Max(nm)	Mid(nm)	Mean(nm)	Rpv(nm)	Rq(nm)	Ra(nm)	Rz(nm)	Rsk	Rku
Red	-58.475	111.182	26.353	0.000	169.658	38.728	26.777	121.287	-0.871	4.077
Green	-7.729	2.305	-2.712	-2.185	10.034	2.275	1.805	7.188	0.460	2.648

Figure A. 14. NC mode AFM topography of TPABT (Rq=2.275nm) film on glass substrate, scan area $5 \times 3\ \mu m$.

EDOT-Amide-TPA

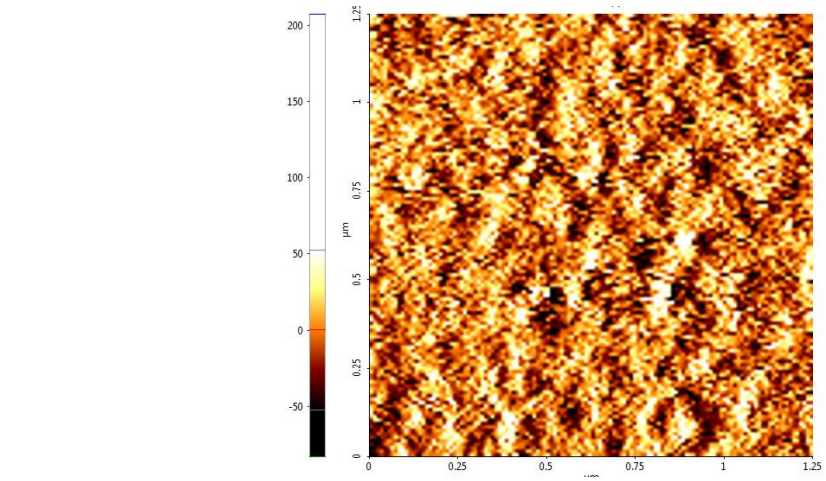

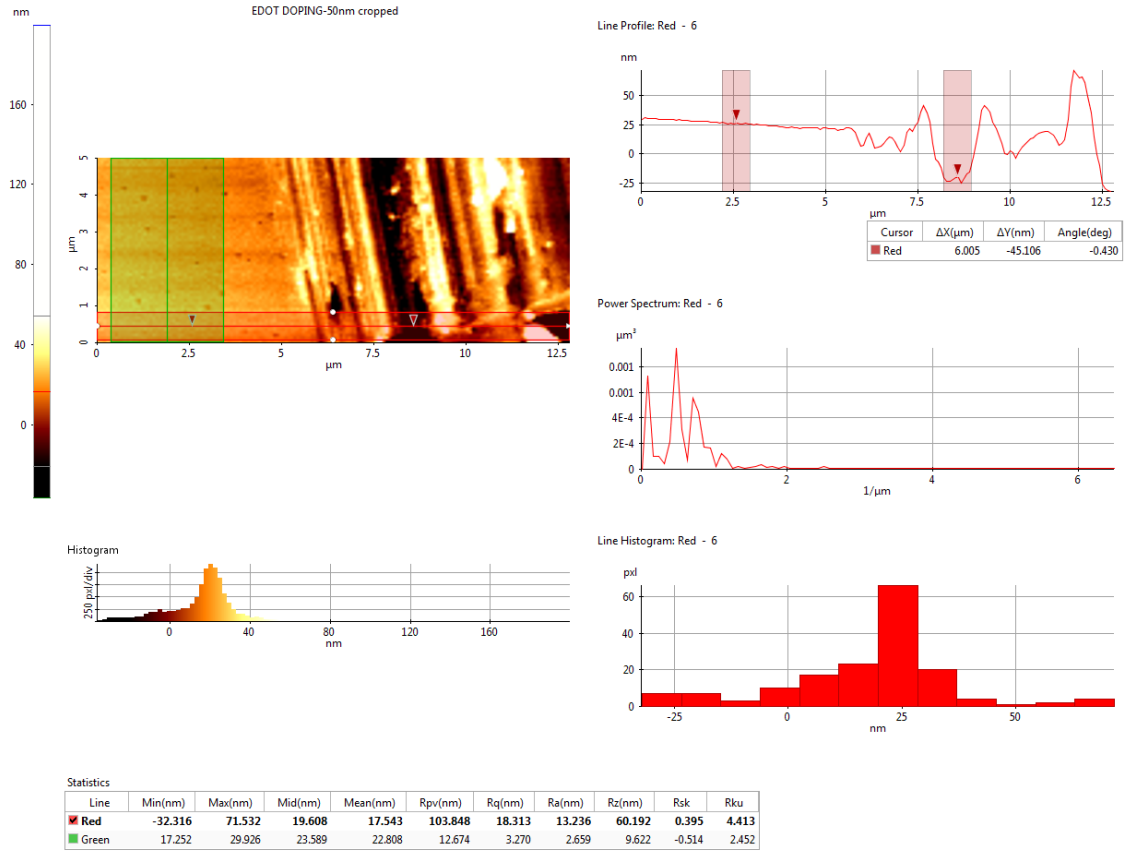

Line	Min(nm)	Max(nm)	Mid(nm)	Mean(nm)	Rpv(nm)	Rq(nm)	Ra(nm)	Rz(nm)	Rsk	Rku
Red	-32.316	71.532	19.608	17.543	103.848	18.313	13.236	60.192	0.395	4.413
Green	17.252	29.926	23.589	22.808	12.674	3.270	2.659	9.622	-0.514	2.452

Figure A. 15. NC mode AFM topography of EDOT-Amide-TPA (Rq=3.2nm) film on glass substrate, scan area $5 \times 3\ \mu m$.

Spiro-OMeTAD

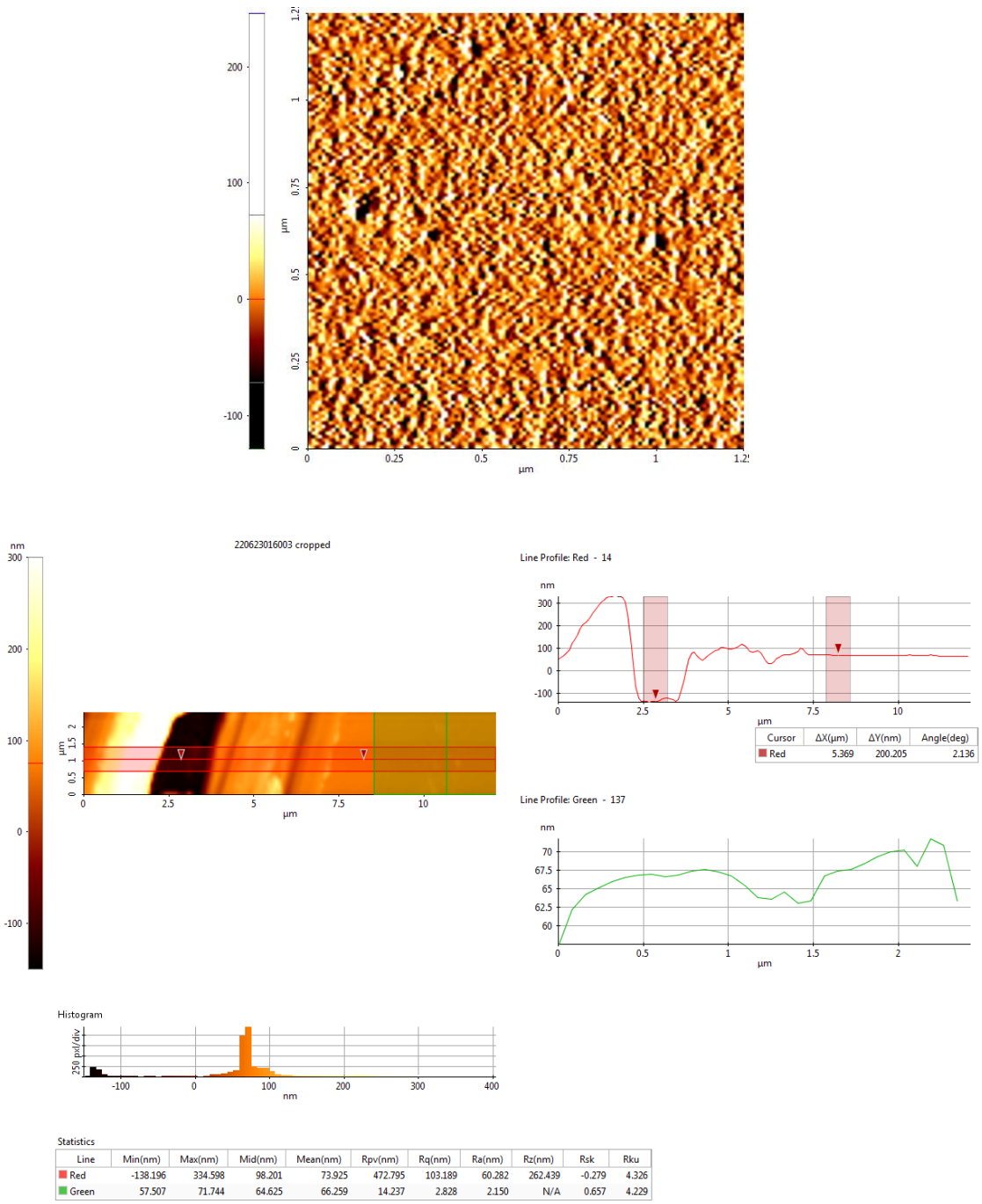

Figure A. 16. NC mode AFM topography of Spiro-OMeTAD (Rq=2.8 nm) film on glass substrate, scan area $5 \times 3\ \mu m$.

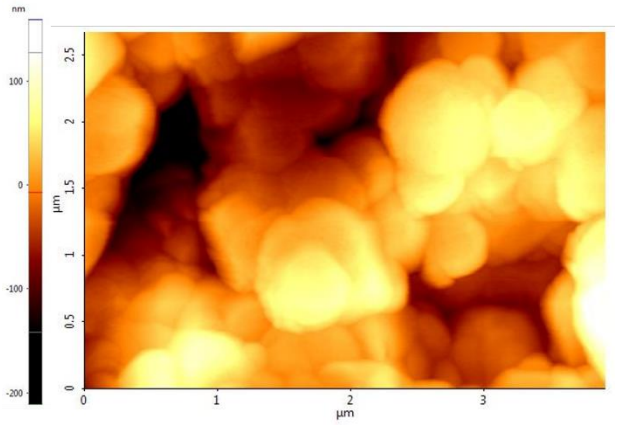

Figure A. 17. NC mode AFM topography of FAMACs perovskite (Rq=43.5 nm), scan area 5×5 µm.

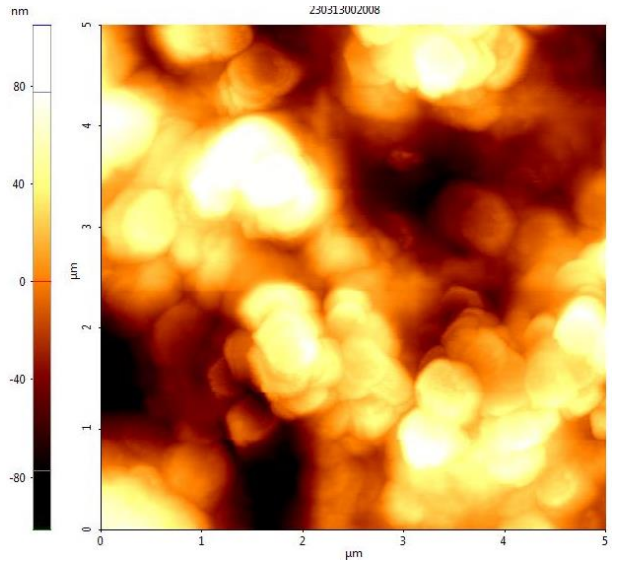

Figure A. 18. NC mode AFM topography of TPABT film upon the perovskite films within the device (Rq=23.5 nm), scan area 5×5 µm.

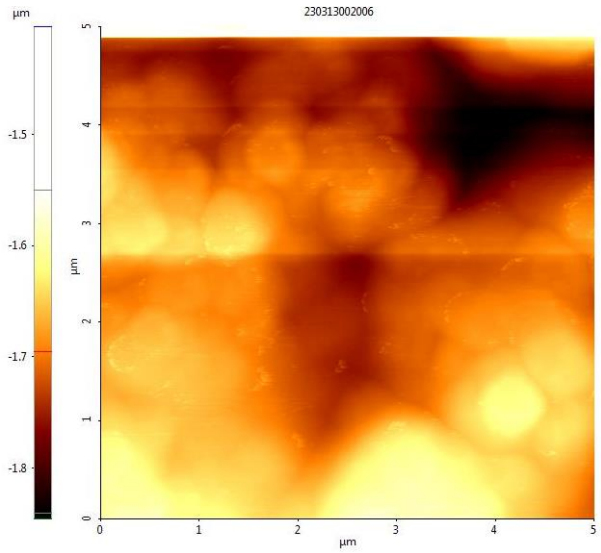

Figure A. 19. NC mode AFM topography of Spiro-OMeTAD film upon the perovskite films within the device (Rq=12.5 nm), scan area 5×5 µm.

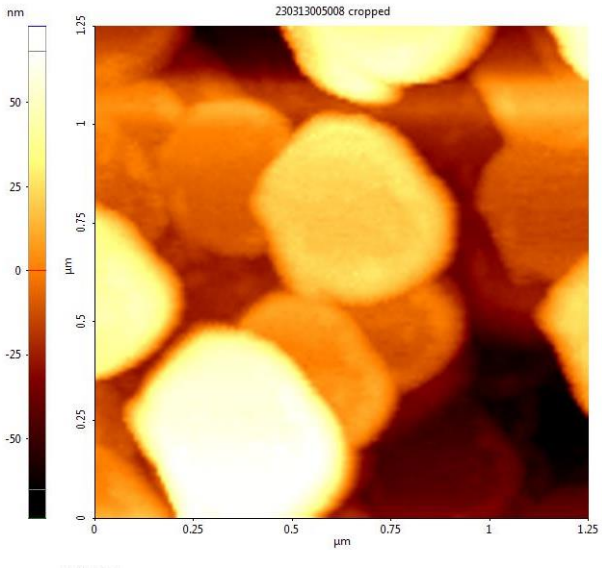

Figure A. 20. NC mode AFM topography of TPABT film (after one week for the oxidation) upon the perovskite films within the device (Rq=17 nm), scan area 1.25×1.25 µm.

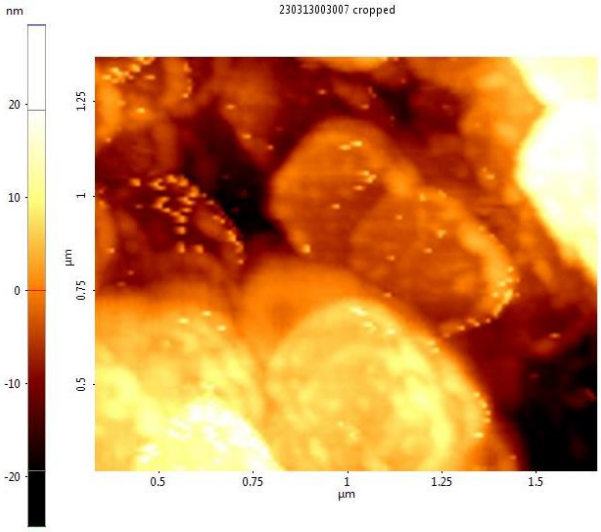

Figure A. 21. NC mode AFM topography of Spiro-OMeTAD film (after one week for the oxidation) upon the perovskite films within the device (Rq=7 nm), scan area 1.75 × 1.5 µm.

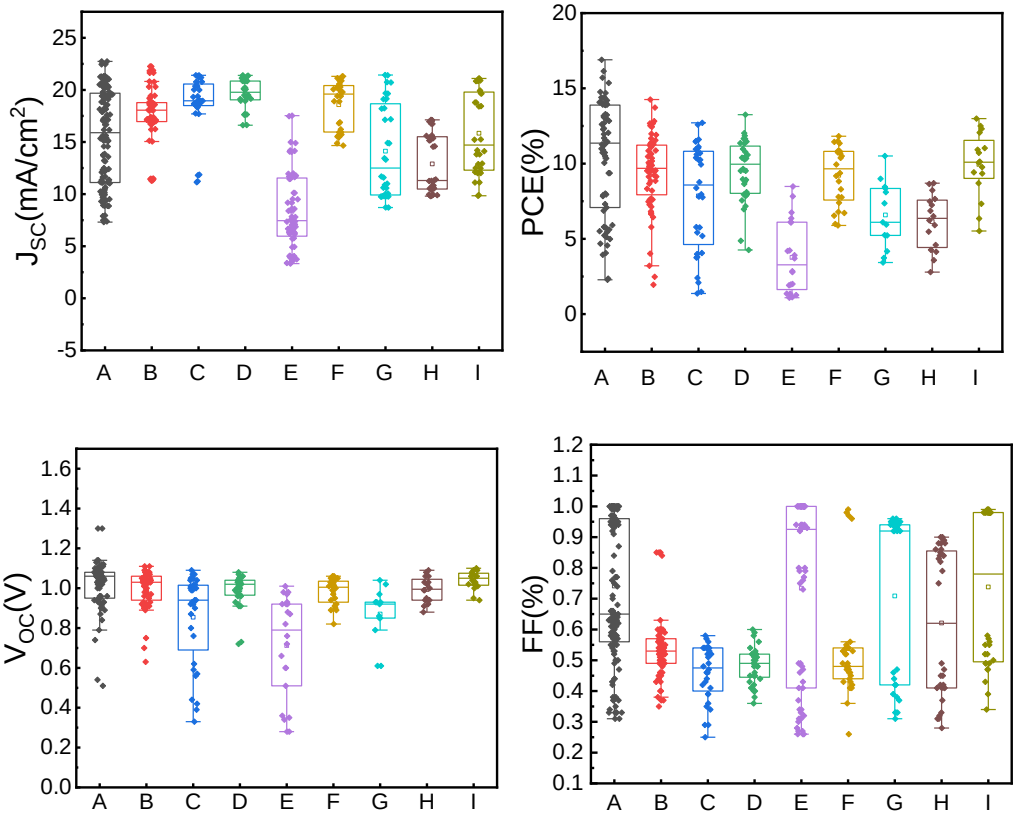

Figure A. 22. Photovoltaic performance FAMACs perovskite devices with SnO_2 as ETM. Box-plot of devices prepared in different parameters, A) Spiro-OMeTAD, B) TPABT doped with 25µL LiTFSi and 10 tBP, C) TPABT doped with 25µL LiTFSi and 12 tBP, D) TPABT doped with 25µL LiTFSi and 8 tBP, E) TPABT doped with 30µL LiTFSi and 10 tBP, F) TPABT doped with 30µL LiTFSi and 12 tBP, G) TPABT doped with 30µL LiTFSi and 8 tBP, H) TPABT doped with 35µL LiTFSi and 10 tBP, I) TPABT doped with 35µL LiTFSi

Table A. 9. The statistical analysis of the efficiency for devices

	Mean	Std. Deviation
A	10.4	3.8
B	9.4	2.6
C	7.8	3.6
D	9.5	2
E	3.8	2.3
F	9.2	1.9
G	6.6	2.21
H	6.2	1.9
I	9.9	2.2

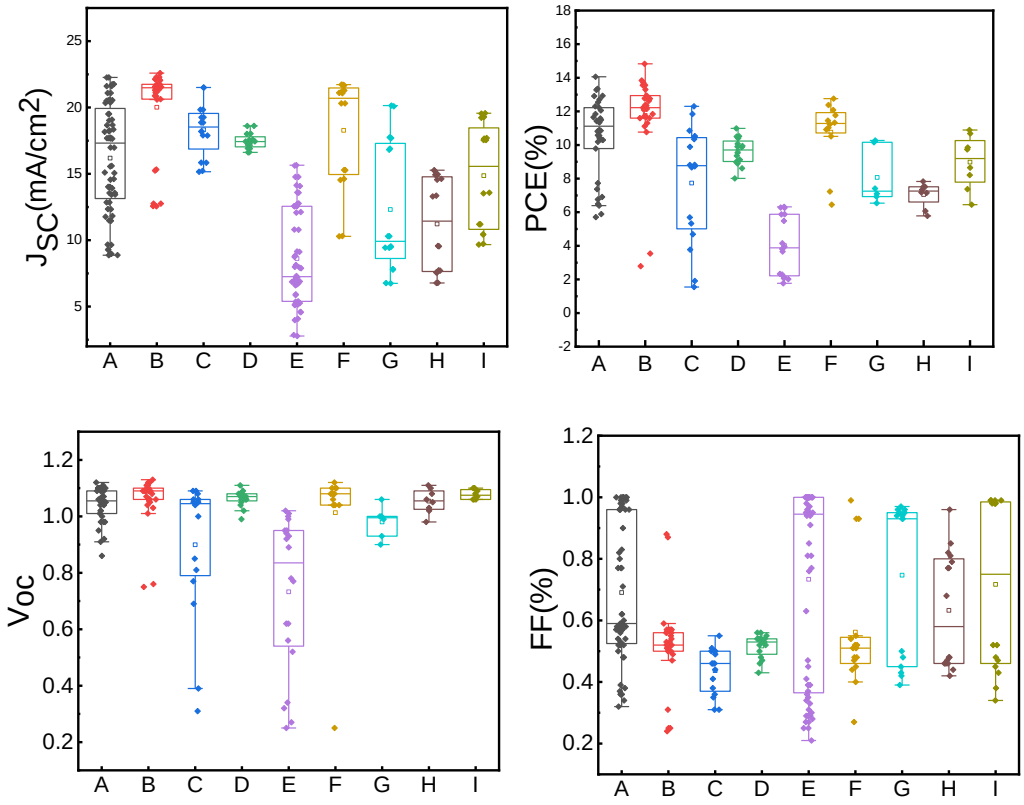

Figure A. 23. Re-measured photovoltaic devices after two days kept under N_2. Box-plot of devices prepared in different parameters, A) Spiro-OMeTAD, B) TPABT doped with 25µL LiTFSi and 10 tBP, C) TPABT doped with 25µL LiTFSi and 12 tBP, D) TPABT doped with 25µL LiTFSi and 8 tBP, E) TPABT doped with 30µL LiTFSi and 10 tBP, F) TPABT doped with 30µL LiTFSi and 12 tBP, G) TPABT doped with 30µL LiTFSi and 8 tBP, H) TPABT doped with 35µL LiTFSi and 10 tBP, I) TPABT doped with 35µL LiTFSi and 12 tBP.

Table A. 10. The statistical analysis of the efficiency for devices.

	Mean	Std. Deviation
A	10.5	2.3
B	11.8	2.6
C	7.7	3.4
D	9.6	0.8
E	4	1.8
F	10.8	1.9
G	8	1.7
H	7	0.7
I	8.98	1.6

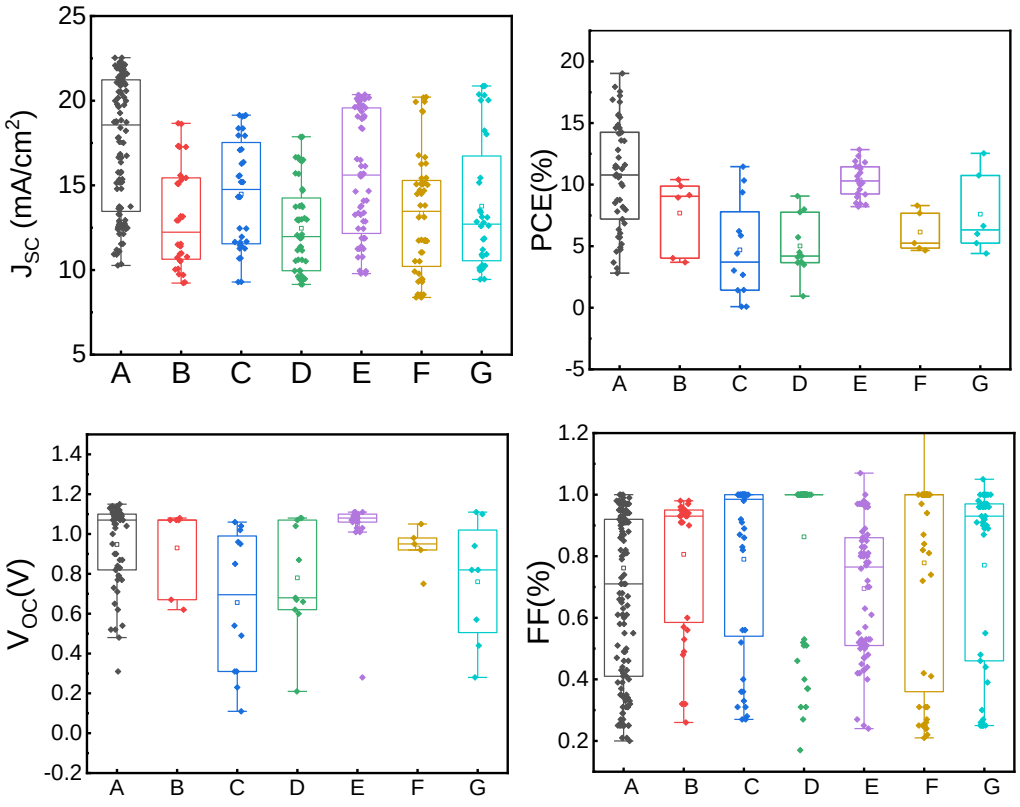

Figure A. 24. Photovoltaic performance FAMACs perovskite devices with SnO_2 as ETM. Box-plot of devices prepared in different parameters, A) Spiro-OMeTAD, B) TPABT doped with 25µL LiTFSi and 12 tBP, C) TPABT doped with 25µL LiTFSi and 12 tBP annealed at 60°C for 30 min, D) TPABT doped with 25µL LiTFSi and 12 tBP annealed at 70°C for 30 min, E) TPABT doped with 30µL LiTFSi and 12 tBP, F) TPABT doped with 30µL LiTFSi and 12 tBP annealed at 60°C for 30 min, G) TPABT doped with 30µL LiTFSi and 12 tBP annealed at70°C for 30 min.

Table A. 11. The statistical analysis of the efficiency for devices.

	Mean	Std. Deviation
A	10.7	4.36
B	7.69	3.01
C	4.7	3.98
D	5.02	2.4
E	10.37	1.34
F	6.15	1.71
G	7.6	3.27

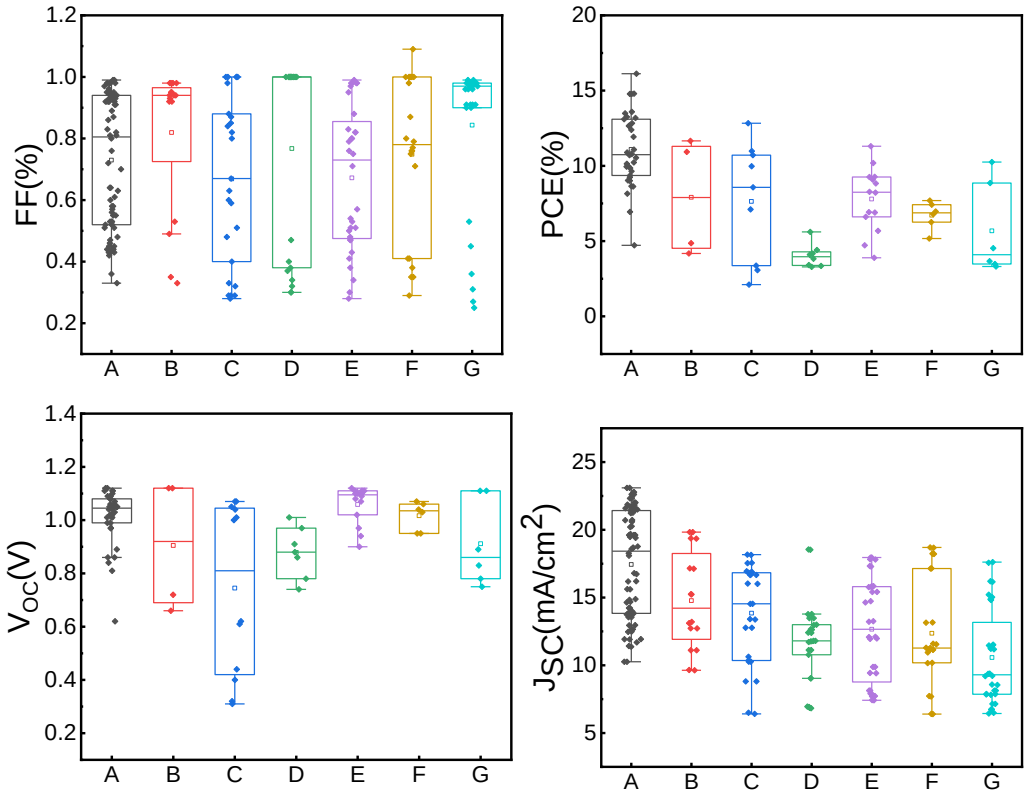

Figure A. 25. Re-measured photovoltaic devices after one day kept under N_2. Box-plot of devices prepared in different parameters, A) Spiro-OMeTAD, B) TPABT doped with 25µL LiTFSi and 12 tBP, C) TPABT doped with 25µL LiTFSi and 12 tBP annealed at 60°C for 30 min , D) TPABT doped with 25µL LiTFSi and 12 tBP annealed at 70°C for 30 min, E) TPABT doped with 30µL LiTFSi and 12 tBP, F) TPABT doped with 30µL LiTFSi and 12 tBP annealed at 60°C for 30 min, G) TPABT doped with 30µL LiTFSi and 12 tBP annealed at 70°C for 30 min.

Table A. 12. The statistical analysis of the efficiency for devices (figure S19).

	Mean	Std. Deviation
A	11.1	2.5
B	7.91	3.9
C	7.64	3.9
D	4.02	0.77
E	7.8	2.1
F	6.71	0.91
G	5.9	3.06

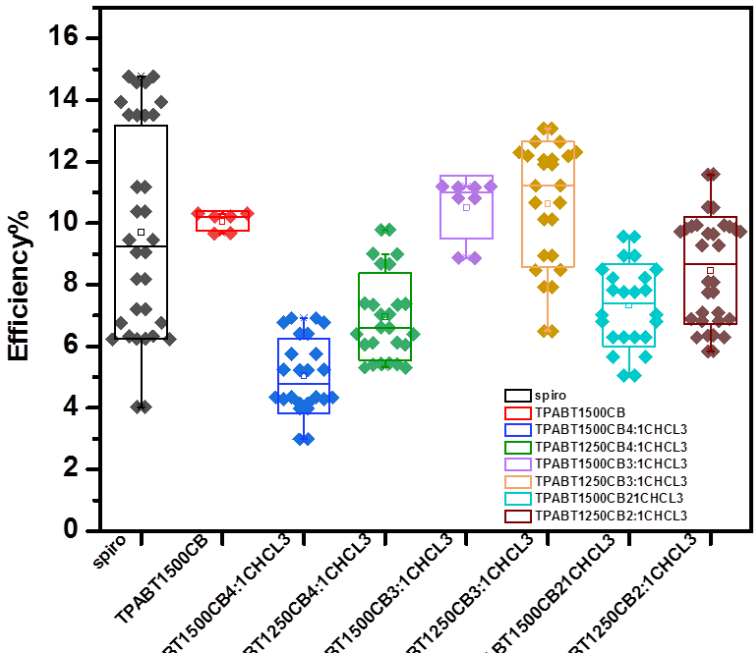

Figure A.26. The efficiency of TPABT and Spiro-OMeTAD with MAPI after 2 days of oxidation for different speeds and different ratio between Chloroform and Chlorobenzene.

Table A.13. The efficiency of TPABT and Spiro-OMeTAD with MAPI after 2 days of oxidation for different speeds and different ratio between Chloroform and Chlorobenzene.

	Jsc	Eff	Voc	FF
spiro	**22.91**	**14.77**	**0.98**	**0.66**
TPABT1500CB	**18.23**	**10.31**	**0.98**	**0.64**
TPABT1500(4CB:1CHCL3)	**11.32**	**6.69**	**0.92**	**0.64**
TPABT1250(4CB:1CHCL3)	**19.35**	**12.89**	**0.93**	**0.72**
TPABT1500(3CB:1CHCL3)	**16.72**	**11.19**	**0.95**	**0.72**
TPABT1250(3CB:1CHCL3)	**20.24**	**13.07**	**0.96**	**0.67**
TPABT1500(2CB:1CHCL3)	**16.13**	**9.56**	**0.93**	**0.63**
TPABT1250(2CB:1CHCL3)	**17.13**	**11.58**	**0.93**	**0.73**

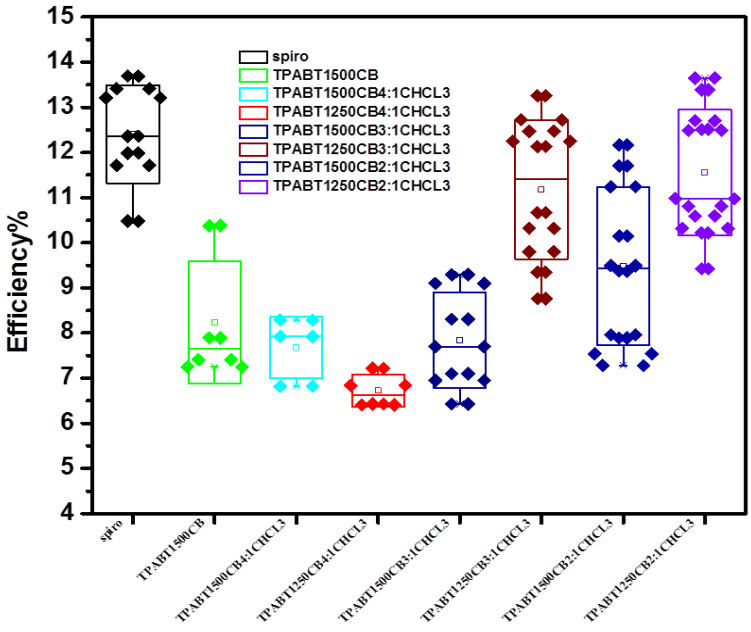

Figure A. 27. The efficiency of TPABT and Spiro-OMeTAD with MAPI after 10 days of oxidation for different speeds and different ratio between Chloroform and Chlorobenzene

Table A.14. The efficiency of TPABT and Spiro-OMeTAD with MAPI after 10 days of oxidation for different speeds and different ratio between Chloroform and Chlorobenzene

	Jsc	Eff	Voc	FF
spiro	22.59	13.69	0.96	0.63
TPABT1500CB	10.87	7.89	0.85	0.72
TPABT1500(4CB:1CHCL3)	12.29	8.29	0.94	0.72
TPABT1250(4CB:1CHCL3)	10.14	6.84	0.88	0.77
TPABT1500(3CB:1CHCL3)	16.8	9.29	0.99	0.62
TPABT1250(3CB:1CHCL3)	19.98	13.26	0.94	0.7
TPABT1500(2CB:1CHCL3)	17.33	12.17	0.93	0.76
TPABT1250(2CB:1CHCL3)	19.97	13.65	0.93	0.74

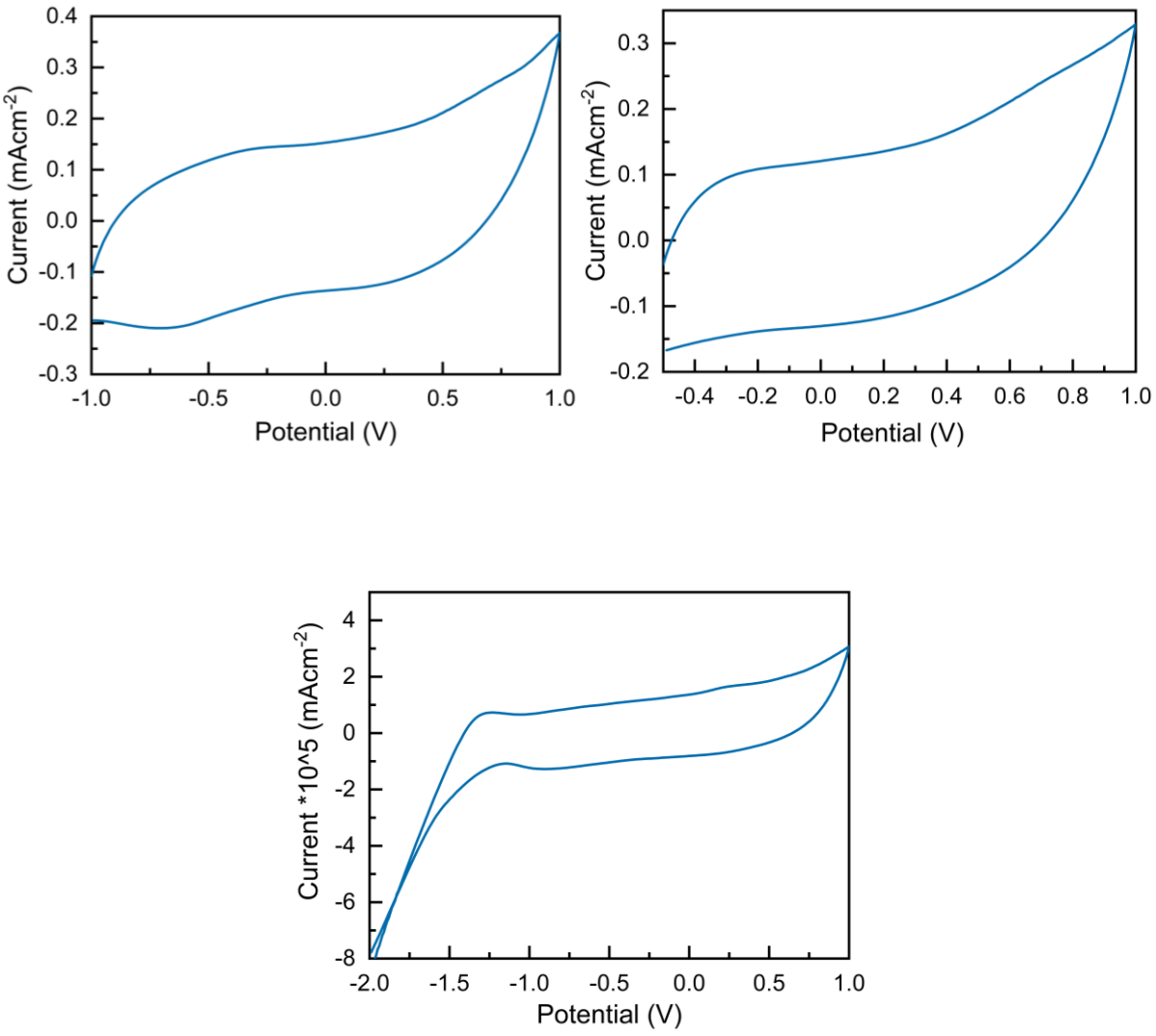

Figure A. 28. Cyclic voltammograms of NiO film), recorded in phosphate buffer (0.05 M pH 7) at scan rates 0.2 mV s^{-1}.

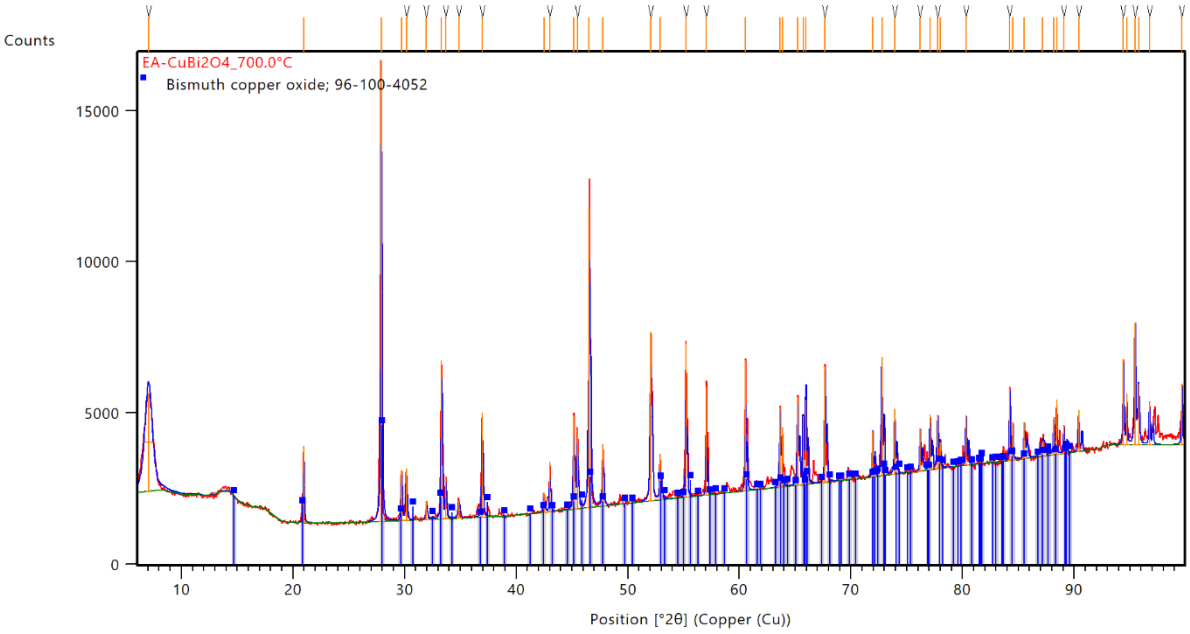

Figure A. 29. Peak match with code 100-4052 for $CuBi_2O_4$ using highscore software.